

VisionHat
**Development of a wearable collision alert system supported
by flexible optic flow sensors**

THÈSE N° 5837 (2013)

PRÉSENTÉE LE 30 AOÛT 2013

À LA FACULTÉ DES SCIENCES ET TECHNIQUES DE L'INGÉNIEUR
LABORATOIRE DE SYSTÈMES INTELLIGENTS
PROGRAMME DOCTORAL EN SYSTÈMES DE PRODUCTION ET ROBOTIQUE

ÉCOLE POLYTECHNIQUE FÉDÉRALE DE LAUSANNE

POUR L'OBTENTION DU GRADE DE DOCTEUR ÈS SCIENCES

PAR

Michał Karol DOBRZYŃSKI

acceptée sur proposition du jury:

Prof. M.-O. Hongler, président du jury
Prof. D. Floreano, directeur de thèse
Prof. D. Atienza Alonso, rapporteur
Prof. H. A. Mallot, rapporteur
Prof. S. Viollet, rapporteur



ÉCOLE POLYTECHNIQUE
FÉDÉRALE DE LAUSANNE

Suisse
2013

Acknowledgements

It is my great pleasure to express my gratitude to the people who have contributed to this thesis with their advice, encouragement and cooperation.

I am especially thankful to Professor Dario Floreano for giving me the opportunity to join the Laboratory of Intelligent Systems. Under his supervision I immersed into the fantastic world of robotics research, so different from the industrial one and so intriguing. Dario provided me with freedom in diverging from the the main path of my PhD, exploring new areas, among many, soft robotics. I owe him my interest in wearable systems. Thanks to Dario I understood the importance of presenting my work clearly and comprehensibly. He taught me how to address the audience and how to gain attention. Last, but not least, Dario introduced me to the robotics community and gave opportunities to meet extraordinary people.

I am particularly indebted to Dr. Ramon Pericet-Camara, for the stimulating scientific discussions and for his support and motivation throughout the four years of my PhD. Without Ramon this thesis would not have been possible. Under his supervision I learned how to write scientific papers and how to present my work. Also, to a grate extent, he was relieving me from many administrative and reporting tasks imposed by working in a European project.

I owe my good knowledge in statistical analysis to Dr. Steffen Wischmann. With his useful suggestions and continuous encouragement he guided me towards the doctoral degree. I owe him much as a doctoral student, friend and a climbing partner.

I wish to express deepest gratitude to my jury members, for accepting the invitation to my exam, taking the time and effort to read my thesis and for sharing their comments. Professor David Atienza Alonso the head of the EPFL's Embedded Systems Laboratory, Professor Hanspeter A. Mallot, the dean of the Faculty of Biology at the Eberhard-Karls-University, Tuebingen, Germany, and Professor Stephane Viollet, the head of the Biorobotique group at the Aix-Marseille University, Institute of Movement Sciences, Marseille, France. I am grateful to Professor Max-Olivier Hongler for accepting the invitation to be the president of the jury.

Acknowledgements

I would like to acknowledge the CURVACE project not only for the financial support provided within the Seventh Framework Programme for Research of the European Commission, under FET-Open grant number: 2009-237940, but most of all for the stimulating atmosphere during (and after) our many brainstorming meetings. These are the people involved in the project who taught me the importance of the team work. I do believe that development of the CURVACE vision sensors would not have been possible without every single one of us. Among all of them I especially thank the PhD students, Fabien Expert, Raphael Juston, Fabian Recktenwald and Andreas Brueckner, whose knowledge and results did always impress me, giving me the motivation to work harder. I am also particularly grateful to Geraud L'Eplattenier, who helped me in addressing many technical challenges. His comments and advices were priceless. Also, Dr. Claudio Bruschini for the coordination of the administrative and financial aspects of the project. He was the pulse-keeper of the project's heart.

I would like to thank all my colleagues and friends from the Laboratory of Intelligent Systems for providing the great atmosphere when sharing hours of working, but also climbing, skiing and cooking. You made me understand the complexities of swarms, genetic algorithms and artificial evolution and helped me develop technically and personally. Among many to Dr. Steffen Wischmann, Dr. Sara Mitri, Adrien Briod, Dr. Adam Klaptocz, Dr. Ramon Pericet, Jurg Germann, Dr. Pawel Lichocki, Andrea Maesani, Dr. Pavan Ramdya, Thomas Schaffter, Przemek Kornatowski, Trevis Alleyne and Dr. Bryan Schubert. In particular, I would like to thank my office mates for many long, disturbing yet stimulating discussions, Dr. Mirko Kovac, Dr. Pradeep Ruben Fernando and Geraud L'Eplattenier. Their enthusiasm and expertise had much impact on the thesis. Also, not to be forgotten, the administrative assistant Michelle Waelti who is the ones that make it all work.

Many sections of the thesis, as well as my articles, were corrected according to the comments of Dr. Ramon Pericet, Dr. Bryan Schubert, Dr. Pradeep Fernando and Trevis Alleyne. I appreciate your unconditional help and the time you spent.

Several students have contributed to this work. I wish to thank in particular Seiffeddine Mejri and Ionut Halasz for their contribution to this research. Also, I wish to acknowledge the 22 volunteers who participated in my experiments.

Additionally, I would like to express my gratitude to Professor Stephanie Lacour and Dr. Hugues Vandeparre from the Laboratory for Soft Bioelectronic Interfaces for their help in producing the hyper-flexible strain gauges. Philippe Vosseler and the atelier pour le routage et la fabrication de circuits imprimés (ACI) for their help and flexibility in producing the PCBs, sometimes stretching the limits of possible. Also, Andre Badertscher for his surgery-precise soldering and patience when correcting my

Acknowledgements

mistakes and Peter Bruehlmeier for sharing his expertise in designing and routing the PCBs.

Finally to my wife and daughter, my two loves, for giving me a life beyond the PhD.

Lausanne, May 2013

Michal Karol Dobrzynski

Abstract

Mobility defines to a great extent the quality of our life. It allows us to perform most of our everyday tasks as commuting to work places, going shopping, or maintaining our physical condition by enjoying a variety of sports. On the other hand, limited mobility autonomy reduces the life quality of some of us, paralyzed, with limb loses or sensory dysfunctions. Among others, it is strongly present for visually impaired people. In order to extend their autonomy, many assistive tools are available. Rapid technological progress over the last decades pushed engineers and scientists towards the development of modern electronic tools addressing the challenge of mobility autonomy of visually impaired people. These tools are called Electronic Travel Aid (ETA). However, the appreciation and utilization of ETA systems are still not significantly widespread and a cane or a guide dog is still the best-established method nowadays. As various studies show, there is still a psychological barrier between visually impaired people and modern assistive devices related to their noticeable visual appearance, low ergonomics and lack of intuitive understanding of the provided feedback. One of the reasons is that addressing these challenges requires holistic interdisciplinary studies difficult to accomplish within the development of one ETA system.

In this thesis, I present a novel holistic approach to the design of an ETA device and introduce the *VisionHat*, a wearable collision alert system supported by flexible optic flow sensors. The *VisionHat* perceives motion present in close proximity through estimation of the optic flow and transmits this information to the user. Although commonly utilized in robotics for collision avoidance or ego-motion estimation, such principle of operation has not been applied in a system for humans yet. The aim of the *VisionHat* is to increase the awareness of the user of surrounding collision threats. The *VisionHat* system is fully integrated with a baseball cap, which overcomes the challenge of ergonomics and wearability. In particular, textile integration is possible due to the use of newly developed mechanically flexible optic flow sensors bearing only 0.9 mm in thickness. Yet, its mechanical flexibility introduces a big challenge for vision processing. Indeed, the shape of the sensor affects considerably its performance, reducing its practical use. In this thesis I explain the source of such behavior and propose a method to maintain the performance of the sensor regardless of its shape.

Abstract

The proposed method requires information regarding the shape of the optic flow sensor as an input.

To acquire this information, two solutions are proposed for real-time shape monitoring. A novel contactless deflection sensing method allows measuring complex 2-D shapes with an angular resolution of 0.8° . The alternative method, a hyper-flexible strain gauge, extends the range of functionality of the contactless deflection sensor providing nearly three-times higher spatial resolution under a similar angular resolution of 0.8° . A novel read-out method applied in the strain gauge method allows decoupling the meaningful shape-related signal from other parasitic signals naturally present in any sensor with a consequent performance enhancement. Moreover, its integration with the flexible optic flow sensor is simple.

To make the *VisionHat* system successful, the extracted collision-threats must be subsequently transferred to the user in an intuitively understandable manner. Therefore, in this thesis I put a careful attention to the design of a feedback system capable of transferring such information quickly and efficiently. A head-attached vibrotactile display is proposed and tested through a set of experiments with 22 human subjects. The tests identified the best design and control of the feedback system pointing on the correct placement of the vibration motors, the strength of the applied vibrations and the maximum number of simultaneously presented stimuli.

Finally, a fully-integrated prototype of the *VisionHat* system is developed and tested. The performance of the *VisionHat* is assessed when worn in an indoor, office-like room, and during outdoor walking, mimicking everyday-life situations. The conducted experiments show optic flow extraction and its subsequent normalization with shape-related information and vibration motors activation for feedback transfer. Despite certain limitations, it is demonstrated that the developed prototype system can support the user in a number of everyday activities, providing collision-related cues within its near proximity.

Keywords: *electronic travel aid, wearability, flexible sensor, optic flow, shape sensing, vibrotactile display.*

Résumé

La mobilité est d'importance majeure pour la qualité de vie. Elle permet de réaliser la plupart des tâches quotidiennes telles que les déplacements pour le travail, faire du shopping ou maintenir notre condition physique en pratiquant une multitude de sports. A l'inverse, un manque d'autonomie en terme de mobilité réduit la qualité de vie d'une personne paralysée, ayant perdu un membre ou ayant une déficience sensorielle, et particulièrement les personnes malvoyantes. Pour augmenter leur autonomie, plusieurs moyens d'assistance existent, par exemple les cannes pour aveugle (cannes blanches) ou les chiens d'aveugles. Cependant, les grands progrès de la technologie de ces dernières décennies ont poussés les ingénieurs et les scientifiques à développer des outils électroniques plus modernes pour répondre au défi de l'autonomie de mobilité pour les personnes malvoyantes. Ces outils sont appelés des aides électroniques pour le déplacement [Electronic Travel Aid ou ETA]. A ce jour, l'appréciation et l'utilisation des systèmes d'ETA n'est pas répandue. Plusieurs études ont montré qu'il existe une barrière psychologique entre les personnes malvoyantes et les moyens d'assistance modernes due à l'aspect visuel, la faible ergonomie et aux informations non-intuitives fournies par ces moyens. Une des raisons de ces défauts découle de la difficulté des études holistiques interdisciplinaires nécessaires au développement d'un système ETA.

Dans cette thèse, je présente une approche holistique novatrice pour le développement d'un ETA et introduit le *VisionHat*, un chapeau contenant un système d'alerte contre les collisions basé sur des capteurs de flux optique flexibles. Ce principe de fonctionnement communément utilisé en robotique pour l'évitement de collisions ou l'estimation de déplacement n'a encore jamais été proposé pour un système destiné aux êtres humains. Le but du *VisionHat* est de permettre à l'utilisateur d'avoir une meilleure information relative aux risques de collision avec ce qui l'entoure. Le système dit *VisionHat* est complètement intégré dans une casquette de baseball, un couvre-chef qui présente l'avantage d'être ergonomique et confortable à porter. L'intégration dans un vêtement est possible notamment grâce à l'utilisation de capteurs de flux optique flexibles récemment développés, et mesurant seulement 0.9 mm d'épaisseur. Néanmoins, la flexibilité mécanique introduit un grand défi pour le traitement des informations visuelles. En effet, la forme du capteur affecte considérablement

Résumé

ses performances et réduit son usage pratique. Dans cette thèse, j'explique la raison d'un tel fonctionnement et propose une méthode pour maintenir les performances du capteur constante indépendamment de sa forme. La méthode proposée nécessite des informations relatives à la forme du capteur de flux optique.

Pour l'acquisition de ces informations, deux solutions pour mesurer la forme en temps réel sont proposées. Une méthode novatrice de détection de courbure sans contact permet de mesurer des formes complexes en deux dimensions avec une résolution angulaire de 0.8° . Cependant, les difficultés techniques liées à l'assemblage du prototype et à son intégration avec le capteur de flux optique flexible m'ont amené à développer une deuxième méthode. Les jauges de déformation hyper flexibles augmentent la plage de fonctionnement du capteur de détection de courbure sans contact, permettant d'augmenter la résolution spatiale pratiquement d'un facteur trois pour une résolution angulaire similaire de 0.8° . Une méthode de lecture des données novatrice appliquée à la jauge de déformation permet de découpler le signal utile du bruit parasite, ce qui permet d'améliorer considérablement les performances. Par ailleurs, son intégration avec le capteur de flux optique flexible est aisée.

Pour que le système du *VisionHat* soit utilisable, les informations de collisions possibles doivent être transmises à l'utilisateur de façon intuitivement compréhensible. Par conséquent, j'ai investi un grand effort dans le développement d'un système de feedback capable de transmettre ces informations rapidement et efficacement. Un système vibro-tactile attaché à la tête, testé durant plusieurs expériences réalisées sur 22 êtres-humains, est présenté dans ma thèse. Les tests ont permis d'identifier les paramètres optimaux du système de feedback tels que la configuration et le type de contrôle, la puissance de vibration et le nombre maximal de stimuli détectés simultanément.

Finalement, le prototype du système *VisionHat* est développé et testé. Les performances du *VisionHat* sont validées suite à des tests où il est porté en intérieur, dans un bureau, ainsi que sur un sujet marchant en plein air, afin d'imiter des situations de la vie de tous les jours. Les expériences réalisées montrent l'extraction du flux optique et sa normalisation en fonction de la mesure de la forme du capteur ainsi que l'activation des moteurs vibrants pour l'envoi du feedback. Malgré quelques limitations, il est démontré que le prototype développé peut aider l'utilisateur dans plusieurs activités quotidiennes en lui apportant des indications sur les collisions possibles dans son environnement proche.

Mots-clés : *aides électroniques pour le déplacement, système à porter, capteur flexible, flux optique, capteur de forme, interface vibrotactile.*

Contents

Acknowledgements	iii
Abstract (English/Français)	vii
Contents	xiii
Nomenclature	xv
List of figures	xix
List of tables	xxi
1 Introduction	1
1.1 Mobility as a Quality of Life	1
1.1.1 Electronic Travel Aids for Visually Impaired People - State of the Art	3
1.2 Thesis Outline	7
1.2.1 Novelties and Contributions	9
2 Vision Tape - Flexible Vision Sensor for Motion Extraction	11
2.1 Introduction	13
2.2 Vision Tape	14
2.2.1 Optical Properties of the Vision Tape	17
2.2.2 Characterization of the Vision Tape	18
2.2.3 Vision Tape - Second Prototype	22
2.2.4 Discussion	26
2.3 Optic Flow Normalization	29
2.3.1 Normalization Procedure	30
2.3.2 Discussion	32
2.4 Conclusions	33
3 Shape Sensing	35
3.1 Introduction	37
3.2 Shape Monitoring	38

Contents

3.2.1	Contactless Deflection Sensor	38
3.2.2	Concave and Convex Deflection Monitoring - Contactless Deflection Sensor with Mirror	47
3.2.3	Hyper-Flexible Strain Gauge	56
3.3	Conclusions	65
4	Vibrotactile Feedback System - Design and Control	67
4.1	Introduction	69
4.1.1	Vibrotactile Displays	69
4.2	Experimental setup	70
4.3	Experiments	72
4.3.1	Experiment 1: Minimum and Comfort Strength for Vibration Perception	73
4.3.2	Experiment 2: Multi-point Discrimination and Vibration Sources Localization	74
4.4	Discussion	79
4.5	Conclusions	81
5	VisionHat - System Integration and Tests	83
5.1	Introduction	85
5.2	System Design and Data Flow	86
5.2.1	Tape, Nerve and Brain Modules	87
5.2.2	Hat Integration	93
5.2.3	Information Processing and Feedback Activation	95
5.3	Experiments	98
5.3.1	Experiment 1: Sitting in an Office	98
5.3.2	Experiment 2: Outdoor Walking During a Cloudy Day	102
5.3.3	Discussion	105
5.4	Discussion	106
5.5	Conclusions	107
6	Conclusions and Outlook	109
A	Appendix A: Vision Tape	113
A.1	First Prototype Design, Image Formation and Image Processing	113
A.2	Experimental set-up	116
B	Appendix B: Shape Sensing	119
B.1	Contactless Deflection Sensor - Electromechanical Design and Signal Processing	119

B.2 Hyper-Flexible Strain Gauge Based on Stretchable-Gold-Deposited-on-PDMS Technology	121
Bibliography	134
C Publications	135
Curriculum Vitae	137

Nomenclature

Abbreviations and Acronyms	
1-D	one-dimension(al)
2-D	two-dimension(al)
3-D	three-dimension(al)
ADC	analog-digital converter
ANOVA	analysis of variance (name of a method)
Au	gold
bps	bits per second
CDS	contactless deflection sensor
CMOS	complementary metal-oxide-semiconductor
CURVACE	curved artificial compound eye(s) (project name)
DS	deflection sensor
DOF	degree(s) of freedom
ETA	electronic travel aid
FIR	finite impulse response
FOV	field of view
fPCB	flexible printed circuit board
fps	frames per second
GUI	graphical user interface
I2A	image interpolation algorithm
I ² C	inter-integrated circuit
IC	intergraded circuit
IO	input / output
IMU	innertia measurement unit
LED	light emitting diode
LR	linear regression
OF	optic flow
PC	personal computed
PCB	printed circuit board
PD	photodiode

Nomenclature

Abbreviations and Acronyms – continued from previous page

PDMS	polydimethylsiloxane
p-p	peak-to-peak
PVD	physical vapor deposition
PWM	pulse width modulation
R ²	correlation coefficient square
SD	standard deviation
SPI	serial peripheral interface
SS	shape sensor
UART	universal asynchronous receiver/transmitter
USB	universal serial bus
VT	vision tape

Symbols

β	deflection angle
$\Delta\rho$	acceptance angle
$\Delta\phi$	interommatidia angle
Γ	reflectivity index
λ	wavelength
Θ	surface contact angle
V	volume
X	resolution

List of Figures

1.1	<i>VisionHat</i> , a wearable electronic travel aid system for visually impaired people.	2
1.2	Review of wearable electronic travel aid systems substituting vision. . .	5
2.1	Review of flexible vision sensors.	13
2.2	Two Vision Tape prototypes.	15
2.3	Vision Tape integrated with various substrates.	16
2.4	Optimal and sub-optimal configuration of Vision Tape.	17
2.5	Vision Tape characterization - rotational and translational component of the optic flow	20
2.6	Amplitude of the rotational optic flow vs. geometry of the imager. . . .	21
2.7	Amplitude of the proximity vs. geometry of the imager.	22
2.8	Second prototype of the Vision Tape developed within the CURVACE project.	23
2.9	Single ommatidium of the second Vision Tape prototype.	24
2.10	Triplet of photodiodes.	24
2.11	Irradiance characteristics.	25
2.12	Rotational optic flow characterization curves for four different shapes of the second Vision Tape prototype.	27
2.13	Peak-to-peak amplitudes of the rotational optic flow of the second Vision Tape prototype under four different shapes.	28
2.14	Evolution of spatial gradient during rotation of Vision Tape	31
2.15	Amplitudes of the rotational optic flow before and after normalization for two Vision Tape prototypes.	32
3.1	Contact-based vs. contactless deflection sensor	39
3.2	Principle of operation of the light-based contactless deflection sensor .	40
3.3	Characterization of the contactless deflection sensor prototype.	41
3.4	Impact of ambient light on the contactless deflection sensor.	42
3.5	2-D model of the contactless deflection sensor based on ray tracing. . .	43

List of Figures

3.6	Angular intensity profile of the light source and angular sensitivity profile of the light sensor	45
3.7	Experimental data vs. simulation for the contactless deflection sensor prototype.	45
3.8	Shape monitoring system based on 12 contactless deflection sensors.	46
3.9	Contactless deflection sensor with mirror.	47
3.10	2-D model of a contactless deflection sensor with mirror based on ray tracing.	48
3.11	2-D representation of three tested profiles of mirrors.	49
3.12	Profile of the mirror vs. angular perception range.	50
3.13	Surface-tension-based manufacturing process of the mirrors.	51
3.14	Manufactured lenses and their subsequent coating.	53
3.15	The measured vs. the desired profile of the mirror.	54
3.16	Contactless deflection sensor prototype integrated with mirror.	55
3.17	Characterization curve of the contactless deflection sensor prototype with mirror	56
3.18	Sensing element of the hyper-flexible strain gauge.	56
3.19	Assembly of the hyper-flexible strain gauge and attachment to the Vision Tape prototype.	58
3.20	Stress simulations of bending the hyper-flexible strain gauge attached to Vision Tape.	59
3.21	The prototype strain-gauge attached to the Vision Tape prototype.	59
3.22	Electrical representation of the hyper-flexible strain gauge and the read-out circuit.	60
3.23	Characterization setup with the hyper-flexible strain gauge prototype attached.	61
3.24	Results of bending test of the hyper-flexible strain gauge prototype.	62
3.25	Shape reconstruction with the hyper-flexible shape sensor.	63
3.26	Macroscopic examination of the failed sensing element.	64
4.1	Experimental setup for head-attached vibrotactile display studies.	71
4.2	Position of the motors on the head.	72
4.3	Minimum and comfort vibration strength across 22 tested subjects.	74
4.4	Perception of number of simultaneously vibrating motors.	76
4.5	Perception of vibration location for one and multiple presented stimuli.	78
5.1	Modular design of the <i>VisionHat</i> system and the signal flow.	86
5.2	Angular perceptive range of the system with individual optic flow vectors marked.	87
5.3	<i>Tape</i> module.	88

5.4 <i>Nerve</i> module	89
5.5 <i>Brain</i> module.	91
5.6 Lithium-ion battery	91
5.7 Graphical user interface for data monitoring.	92
5.8 Baseball cap with <i>Tape</i> , <i>Nerve</i> and <i>Brain</i> modules integrated	95
5.9 Four colors of the baseball cap.	96
5.10 Vibration motors activation thresholds.	97
5.11 Experiment 1: sitting in an office - experimental setup.	98
5.12 Shapes of the vision chips left and right registered during the first experiment.	99
5.13 Optic flow and motor activation throughout the first experiment.	101
5.14 Experiment 2: outdoor walking during cloudy day - experimental setup.	102
5.15 Shapes of the vision chips left and right registered during the second experiment.	103
5.16 Optic flow and motor activation throughout the second experiment.	104
A.1 Mechanical layout of the first Vision Tape prototype.	114
A.2 Scheme of operation of the first Vision Tape prototype	114
A.3 Order of pixels for convex and concave configuration of flexible imager	115
B.1 Components and signal flow of the shape monitoring system based on the contactless deflection sensors.	120

List of Tables

1.1	Summary of existing electronic travel aid systems.	7
2.1	Comparison of the two developed Vision Tape prototypes.	29
4.1	Percentage of sequences in which the number of motors is correctly indicated with respect to the number of simultaneously active motors in a sequence, for three tested strengths of vibrations.	76
5.1	Summary of the weight, current consumption and number of units of the <i>VisionHat</i> system components.	94
A.1	Main geometrical and optical parameters of the first Vision Tape prototype.	116

*Co było wielkie, małem się wydało.
Królestwa bladły jak miedź zaśnieżona.*

*Co poraziło, więcej nie poraża.
Niebiańskie ziemie toczą się i świecą.*

*Na brzegu rzeki, rozciągnięty w trawie,
Jak dawno, dawno, puszczam łódki z kory.*

Czesław Miłosz,
Montgeron, 1959

Mojemu Ojcu.

1 Introduction

1.1 Mobility as a Quality of Life

It is not an exaggeration to say that mobility defines the quality of our life. It allows us to every day move to work places and relax practicing a variety of sports. Mobility gives freedom in exploring the world when diving in an open sea and climbing Himalayas' mountains. Moreover, it has been shown that practicing sports or even only performing intensive walking has beneficial effects for healthcare and fitness.

Lack of autonomy in mobility is particularly visible when coming to people with disabilities, paralyzed, with limb loses or sensory dysfunction. Researchers and engineers are trying to extend their mobility autonomy developing prosthesis, exoskeletons and Electronic Travel Aids (ETA) devices, supporting body posture, limb movements, allowing path planning and obstacle detection. However, despite great technological progress in the domain of prosthetic devices, vision prosthesis (commonly referred to as bionic eyes) are still behind a horizon. Although attempts are made to develop systems that stimulate the vision nerve in order to enhance or recover the lost vision [1–4], these systems apply to a very selected group of visually impaired patients and do not yet address the general challenge of mobility autonomy. ETA systems are more flexible in this manner and allow operation by nearly every visually impaired person. Yet, despite a long history of research and system development, there are few commercially available products.

As analyzed by Kaczmarek et al. [5] two equally important challenges must be addressed in an ETA system design: (i) wearability and ergonomics, reflected by a comfort in wearing in every-day operation and, (ii) information transfer, addressed by designing a feedback system capable of transferring intuitively-understandable information during long-time operation. Moreover, as derived by Mau et al. [6] from a series of interviews and ethnographic studies at the Blind and Visual Rehabilitation Service of Pittsburgh, the visual appearance of the assistive device during its utilization builds a



Figure 1.1: *VisionHat*, a wearable electronic travel aid system designed to extend mobility of blind and visually impaired people by providing collision-alert feedback (left); concept application - *VisionHat* supports visually impaired person in outdoor navigation.

psychological barrier and is perceived as a stigma among the visually impaired users. Hence, in order to make an ETA system successful, beside reliable operation and extended autonomy, such aspects as wearability, capability of transferring feedback in a comprehensive manner and unnoticeable integration with clothes must be targeted.

In this thesis I focus on the problem of mobility autonomy of blind and visually impaired people and design a wearable ETA system, the *VisionHat* (Fig. 1.1 (left)), addressing the mentioned challenges. As foreseen in Fig. 1.1 (right), the aim of the *VisionHat* is to provide information to a user regarding collision threats present in the surrounding environment during every-day activities. To acquire collision-related information the system extracts the Optic Flow (OF), the pattern of apparent motion of objects in the visual scene caused by the relative motion between an observer and the scene. This simple, yet, powerful bio-inspired principle proved robustness in many autonomous navigation systems [7–13] supporting collision avoidance and proximity estimation of robotics platforms, but has not yet been proposed for ETA. The *VisionHat* incorporates a specially developed flexible imager allowing on-board vision processing for OF extraction. Unnoticeably integrated with cloths and with long battery autonomy the *VisionHat* allows operation with no limitations to body movement of a user. Moreover, in this thesis I put great effort in understanding the optimal design and control of a display capable of transferring collision-related information. I propose head-displayed vibrations as a fast and intuitively understandable method for information transfer and perform human experiments assessing its efficiency. The display is unnoticeably integrated with the *VisionHat*. I believe, that the

research conducted towards the *VisionHat* will greatly contribute to of a development of a widely accessible ETA system extending mobility autonomy of visually impaired people.

1.1.1 Electronic Travel Aids for Visually Impaired People - State of the Art

To provide a general background to the research presented in this thesis I describe in the following section wearable ETA systems that address the challenge of mobility extension of blind and visually impaired people. I use this opportunity to discuss their advantages and drawbacks and how the described ETA systems comply with the previously mentioned challenges of wearability and information transfer. Here I focus only on those, which aim at substitution of vision, in order to give objects, motions, distances and, at the end, collision-threat feeling. These devices, equipped in various sensors provide vision-substituting feedback through sound, touch or vibrations. Specific state of the art regarding available flexible imagers and vibrotactile displays is given in the corresponding chapters, 2 and 4, respectively.

According to Aristotle, humans possess five basic senses: sight, hearing, touch, smell and taste [14]. Sensory substitution is an idea formalized by Paul Bach-y-Rita in 1960's to transform the characteristics of one human sensory modality into stimuli of another sensory modality. According to Bach-y-Rita, sensory substitution is possible due to the flexibility of human brain, which is reflected by humans ability to learn. The first successful experiment, proving the concept, was conducted in 1969 [15]. In the experiment low resolution vision was directly substituted with a set of vibrating pins. After 80-100 hours of training the blind patient claimed to have a fuzzy feeling of passing objects and distances, based on the substituted vision only. Going along the line of the first experiment conducted in 1969, many devices use vision as a main input signal. Sainarayanan et al. developed *NAVI* - a vision system for obstacle identification based on a single head-attached camera [16] (Fig. 1.2 A). The system translates an input image to an output sound, where vertical position of the image pattern is inversely proportional to the pitch of the sound. The pixel intensity corresponds to the loudness of the sound. Computational power required for image processing is achieved with a backpack carried portable computer, which limits the overall wearability. Commercially available *vOICe* (Fig. 1.2 B), a system developed by Meijer [17], translates visual information acquired from cameras attached to glasses into sound patterns. Due to the complexity of the feedback signal the system requires intensive training. Nonetheless, it is one of the two still commercially available systems. *Tyflos*, developed at Wright State University by Bourbakis et al. [18], is a stereo-camera based system

that provides multimodal feedback through a combination of sound and vibrations (Fig. 1.2 C). An image processing algorithm selects regions of interests within the Field Of View (FOV) of the cameras localizing potential collisions and identifying free paths. Additionally, *Tyflos* recognizes simple voice commands, which facilitates its operation by visually impaired people. However, similar to *NAVI*, wearability of *Tyflos* is limited by the carried portable computer needed in the image processing and voice recognition processes. In [19] Rodriguez et al. show a design and a prototype of an obstacle localization device based on a stereo-vision, providing feedback through stereo sound. The system runs an image segmentation algorithm that allows dynamic object localization in front of the user. Again, due to high computational power needed to handle image processing, the system requires a portable computer that has to be carried in a backpack.

In the so far described systems, the cameras are usually attached to the head or, as in case of *vOICE* or *Tyflos*, to sun glasses. The obtained feedback signal is rich in information not only about the motions or distances, but also, for instance, colors. As these devices are designed to mimic human vision, they operate under similar conditions to human vision - illuminance from -8 cd/m^3 to $+3 \text{ cd/m}^3$ [20] and good visibility. Distance perception varies from single centimeters to tens of meters, depending mostly on the type of cameras and lenses used. Unfortunately, vision processing algorithms proposed in these systems for objects detection and navigation are computationally expensive and require a portable computer, which significantly limits their wearability.

An alternative approach is the use of direct distance measurement like ultrasonic proximity sensors. Two main system design approaches can be distinguished: hand-carried systems and cloth-integrated, wearable systems. In the first approach, the devices are held in the hand and are similar in size, shape and weight to a hand torch. The feedback is transmitted through the handle equipped with vibration tips. Typically, the distance measurement is triggered by the user with a button. The FOV of these devices does not exceed 20° . Nevertheless, this narrow FOV can be compensated with hand rotation, which allows scanning of all desired directions. A good examples of such a device is the system developed at the New Jersey State University by Bouzit [21] (Fig. 1.2 D). This small and lightweight hand-held system is equipped with four sonar sensors and a 4×4 matrix of vibrating pins to provide feedback, supporting navigation in an unknown environment. Another example is the *CyARM* developed by Ito et al. [22] (Fig. 1.2 E). This device uses an ultrasonic sensor for proximity perception. The proximity-related feedback is provided through the tension of a wire attached to the belt of the user. This 500g device is able to detect ca. 90% of presented static obstacles. However, hand-carried devices limit objects interaction capabilities of the users.

1.1. Mobility as a Quality of Life

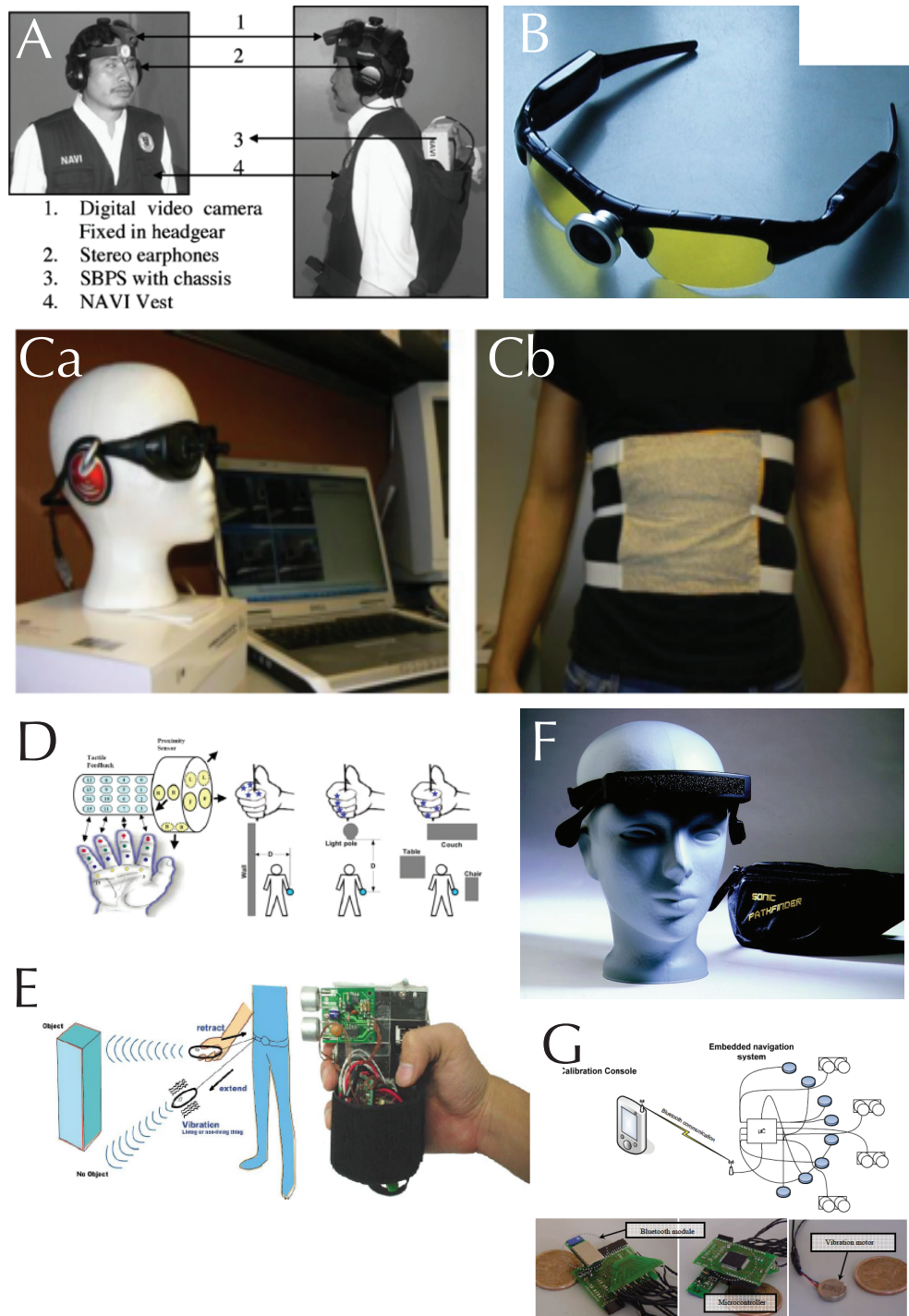


Figure 1.2: Wearable Electronic Travel Aid systems substituting vision.
Vision based: (A) NAVI, Sainarayanan 2007 [16], (B) *vOICE*, Meijer 1992 [17], (C) *Tyflos*, Bourbakis 2008, [18] (Ca) sensor and audio feedback, (Cb) vibrotactile belt;
distance based: (D) Bouzit 2004 [21], (E) *CyARM*, Ito 2005 [22], (F) *SonicPathfinder*, 2012, (G) Cardin 2006 [23].

Chapter 1. Introduction

The commercially available wearable *SonicPathfinder* (Fig. 1.2 F) is an ultrasound sonar-based system that allows to perceive objects in front as well as on the sides of a user. This head-worn device translates distance information into an auditory signal. Although this device increases the general awareness of obstacles on the path [24, 25], it has been shown that *SonicPathfinder* does not significantly improve efficiency of navigation or reduces number of collisions. Very similar in construction and principle of operation is a mobility aid device inspired by the echolocation of bats, developed by Ifukube et al. [26]. This head-attached device allows localization of objects down to 5 cm in diameters through an auditory feedback. A wearable system developed by Cardin [23] (Fig. 1.2 G) makes use of four ultrasonic distance sensors attached to a shirt. The system measures distances to surrounding objects providing feedback signal through eight body-attached vibration motors. The provided calibration console communicates wirelessly with the main control unit and allows to tune the feedback strength to a desired level.

In general, FOV of wearable devices is much wider than in case of hand-carried ETA, but still does not exceed 180° . Wearable systems require sensors-with-textile integration, which is usually difficult, due to flexibility of the substrate and rigidity of the electronic components. This is a particular problem in older systems, where bulky and heavy components greatly limit their practical usage. In wearable ETA systems sensors are typically placed on the torso or on the head of a user, and permanently attached to a jacket or a hat. Although the majority of the described systems does not support alerting against collision, but focus on providing continuous information about surrounding environment, collision-sensitive situations can be deduced by the user from the temporal profile of the feedback signal.

In none of the presented systems an extensive evaluation of feedback perception is performed. The provided information indicate, that users exposed to auditory feedback perform well in experiments involving objects detection and navigation. However, although sound allows to understand information of much higher density, sound-based feedback diminishes overall hearing capabilities limiting understanding sound-related cues naturally picked from a surrounding environment. For this reason in most of the described ETA systems a vibrotactile feedback is used. However, for good information transfer vibrating elements need to be with direct contact or close proximity to human skin. Therefore, careful placement and fine attachment have to be performed before every usage.

All the described devices, sorted with respect to the year of appearance, are summarized in the Table 1.1.

Table 1.1: Summary of existing electronic travel aid systems for human.

	Principle of perception	Feedback signal	Sensors placement
P. Bach-y-Rita, 1969 [15]	single camera vision	tactile, vibration pins attached to users back	no attached to the user, stand behind
T. Ifukube et al., 1991 [26]	ultrasound proximity sensor	sound through headphones	attached to the head
<i>vOICe</i> P. Maijer, 1992 [17]	stereoscopic camera	stereoscopic sound through headphones	behind the sun glasses
<i>SonicPathfinder</i> , 1999 [24, 25]	ultrasound proximity sensor	stereoscopic sound through headphones	attached to the head
M. Bouzit et al., 2004 [21]	ultrasound proximity sensor	tactile, vibrating pins attached to the device	hand-carried
<i>CyARM</i> K. Ito et al., 2005 [22]	ultrasound proximity sensor	tactile, vibrating pins attached to the device	hand-carried
S. Cardin et al., 2006 [23]	ultrasound proximity sensor	tactile, vibration motors attached to user body	attached to the torso
<i>NAVI</i> G. Sainarayanan et al., 2007 [16]	single camera	stereoscopic sound through headphones	attached to the head
<i>Tyflos</i> , Bourbakis et al. 2008 [18]	stereoscopic camera	stereoscopic sound through headphones + belt displayed vibrations	sun glasses
Rodriguez et al. 2012 [19]	stereoscopic camera	stereoscopic sound through headphones	behind the sun glasses

1.2 Thesis Outline

In this thesis I describe my steps towards the development of a wearable ETA system called *VisionHat*. This system addresses the challenge of wearability and the challenge of information transfer.

In Chapter 2 I describe the Vision Tape (VT) - a novel class of flexible compound-eye-like linear vision sensor dedicated to motion extraction and proximity estimation. Despite low spatial resolution VT allows perception and subsequent processing of motion-related information with a frequency of up to 300 frames per second (fps). Characteristics of the VT regarding image perception and motion processing are presented and discussed. VT significantly facilitates the problem of wearability and integration with cloths in a comfortable and an unnoticeable manner by supporting

Chapter 1. Introduction

deformations of the textiles during every-day operation. Moreover, low power consumption supports long-time operation under battery supply. In Chapter 2 it is also shown that information about the shape of the VT is crucial for image processing.

Therefore Chapter 3 describes my work on custom developed shape sensors capable of real-time shape monitoring of a VT, even during active bending. In particular I describe the novel contactless deflection sensing method, which allows to perform measurements without a physical contact between the sensor and the substrate in the point of deflection. The method allows to remove the impact of the sensor on the deflection measurement, particularly important when measuring very flexible substrates, as one used in the VT. Nonetheless, the method presents technological difficulties when integrating with the VT and does not allow to obtain the desired spatial resolution. To address this issue I investigate the second method, based on the hyper-elastic strain gauge. Thanks to the custom-designed read-out strategy, the method supports high spatial and temporal resolutions and simplifies the integration process with the VT.

The challenge of information transfer is addressed in Chapter 4 of this thesis. This chapter describes human-related experiments which conclude on the optimal design and control of a head-attached vibrotactile display, proposed as a feedback system for the *VisionHat*. I focus on understanding influence of parameters of the system on efficiency of information transfer. In particular, the obtained results answer the questions regarding: placement of the vibration motors, amplitude of vibrations allowing perception by every tested user and maximum possible number of simultaneously operating motors.

The *VisionHat* is introduced in Chapter 5, and emerges from a combination of the VT and the vibrotactile feedback system. Main focus of this chapter is put on the system design. The presented modular approach, reflected by three module types used in the system, support fast communication and scalability. Tests related to system wearability are described. In particular I show performance of the *VisionHat* when walking in a natural outdoor environment and when sitting on an office-like room. The tests confirm that the system is capable of perceiving moving objects and alerting against potential collisions.

Chapter 6 concludes the thesis and gives outlook to possible system extensions and future work.

1.2.1 Novelties and Contributions

This thesis contributes to the areas of robotic research, sensors and biomedical engineering through several innovative ideas and technologies that could have applications beyond the purpose of the *VisionHat* development. The three main contributions are summarized here:

- Development of a flexible vision sensor and understanding of the impact of its flexibility on acquisition and processing of an obtained image. In particular, introduction of the sensor fusion method linking shape of such a sensor with the extracted OF. The method allows normalization of the motion vectors and preservation of the sensor performance at an optimal level for an arbitrary geometry.

The developed sensor, along with the normalization method, may be useful in many areas of robotic research including soft and flying robotics, as well as wearable systems.

- Development of a concept and a subsequent prototype of a contactless deflection sensor. The main novelty of the sensor, the capability of measuring deflections with no contact to the substrate in the place of deflection and hence no impact on its inherent flexibility, allows applications to systems where flexibility is of the highest priority. Moreover, due to the principle of operation, the sensor shows no hysteresis which significantly facilitates deflection measurements.

The proposed concept addresses many challenging applications providing fast and precise shape monitoring of hyper-flexible substrates as, for instance, artificial skin or e-textiles.

- Studies of the perception of vibrations applied to the skin of a human head. In particular, finding that moderate strength of vibrations guarantees successful perception by every user, identifying best locations for motors placement and understanding how multiple simultaneously presented stimuli affects the success of their perception.

The conducted studies not only give hints on the design and control of a head-attached vibrotactile display, but also contribute to the general understanding of the vibration-sensitivity of human skin and its distribution along the head.

2 Vision Tape - Flexible Vision Sensor for Motion Extraction

In this chapter, I introduce Vision Tape (VT), a novel class of flexible compound-eye-like linear vision sensor dedicated to motion extraction and proximity estimation. This novel sensor possesses intrinsic mechanical flexibility that provides wide-range adaptive shape, allowing adjustable field of view as well as integration with numerous substrates and curvatures. VT extracts OF of the visual scene to calculate the motion vector, which allows proximity estimation and collision detection based on the motion parallax principle. In order to validate the functionality of VT two prototype devices were developed and characterized, which consist of an array of photodiodes attached to a flexible printed circuit board that acts as mechanical and electrical support. The prototypes performs image acquisition and processing with an integrated microcontroller, even during bending of the sensor. With these, the effect of VT shape on motion perception and proximity estimation is studied and, in particular, the effect of pixel-to-pixel angle is discussed. The results of these experiments allow estimating an optimal configuration of the sensor for OF extraction. In this chapter I also propose a normalization method to enhance the capabilities of the VT in sub-optimal configurations. The experimental results show that, by applying the proposed method to VT in a sub-optimal curvature, the quality of the OF can be increased approaching the one extracted with optimal configuration of the imager.

Adapted from the journal article:

[27] *Vision Tape - A Flexible Compound Vision Sensor for Motion Detection and Proximity Estimation* (2012)

M.K. Dobrzynski, R. Pericet-Camara and D. Floreano,

Sensors Journal, IEEE **12**(5), pp: 1131-1139

DOI: 10.1109/JSEN.2011.2166760

Fig. 2.3 has been selected for the front page of the volume.

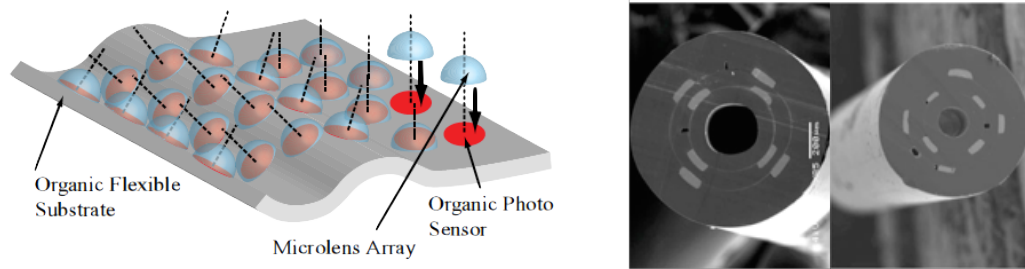


Figure 2.1: Flexible vision sensors. A: matrix of flexible photodiodes developed with an organic polymers technology [28], B: microfiber with integrated silicon photodiodes [30].

2.1 Introduction

Flexible imagers promise many interesting features with respect to conventional, single-lens, rigid cameras, such as adjustable FOV, multi-directional vision, thin packaging, or the possibility of integration onto deformable substrates [28–30]. The properties of thin flexible imagers are suited well to wearable ETA systems. For instance, they could replace bulky and heavy stereoscopic cameras [17, 18] or ultrasonic sensors [23, 26] in collision alert systems for visually impaired people, providing smaller weight and size, enlarging the global FOV and increasing the spatial and temporal resolution. But also, flexible cameras could extend the functionality of skin-like touch sensors, such as those described in [31], with motion detection and proximity estimation. Rigid compound cameras have already been used in mobile robots for obstacle avoidance and navigation [11, 32–34], and could be replaced by flexible equivalents allowing, for example, tunable FOV and robustness on collisions. In the field of soft robotics, flexible cameras could allow deformability of the vision sensors of robots that shrink to get through narrow openings [35].

Development of a flexible vision sensor is particularly challenging. In 2005, Saito et al. [28] presented a flexible skin-like imager consisting of a matrix of 16x16 polymer photodiodes integrated with a layer of microlenses (Fig. 2.1 left). Although the possibility of capturing the image while bending the sensor was reported, the difference in flexibility between the layer of photodiodes and the layer of microlenses caused optical misalignments that decreased the quality of the image. More recently, a set of silicon photodiodes integrated with a polymer microfiber was described [30] (Fig. 2.1 right). Nevertheless, this system is still far from being applied in a real scenario, as a dual-wavelength monochromatic light source is required in the image acquisition process.

In this chapter, I introduce a new class of mechanically flexible compound linear vision sensor, known as Vision Tape along with the conceptual design, two developed prototypes and characterization results. Flexibility of the imager and its thin packaging promise easy integration with textiles and robustness in long-time wearing by complying with deformations naturally present in cloths.

VT presents several advantages over the already existing flexible cameras, namely, the possibility of image acquisition under a wide range of curvatures and fast image extraction and visual data processing. On the other hand, the low spatial resolution of the imager makes it more suitable for motion extraction and proximity detection than for image recognition. Herein, the characteristics of VT are described and the effect of its shape on motion perception and proximity estimation is analyzed with the help of a the prototype device, built using off-the-shelf elements. The optimal curved configuration for the best possible performance of such tasks is determined and compared with sub-optimal arrangements. Conclusions drew from the obtained results lead to design and fabrication of a second prototype, developed within the CURVACE project. Moreover, in this chapter I propose a method to enhance the capabilities of the VT in sub-optimal configurations. This simple normalization method allows to maintain amplitude of the OF extracted with a VT during active bending of the imager.

2.2 Vision Tape

VT is a novel class of mechanically adaptive vision sensor with a design based on the compound-eye concept that can adapt its shape to a wide range of underlying surfaces due to its inherent flexibility. Although the required electronic elements may introduce rigid regions, the flexible spaces between them allow easy bending, which may reach up to 360° in the direction of the pixel array. VT is aimed to extract motion and estimate proximity to objects within its vision field even if the characteristics of the attachment surface are not known *a priori*. The first prototype, developed in 2009, consists of eight linearly arranged photodiodes (pixels) and one microcontroller that is responsible for the acquisition and processing of the images (Fig. 2.2 left). This prototype is used in studies over the mechanical behavior of the sensor, textile integration and image formation and processing under non-planar configurations of the sensor. The second prototype (Fig. 2.2 right), developed in 2012, instantiates the knowledge and experiences gathered through the characterization process of the first prototype. In particular, the dynamic range, the spatial resolution of the pixels and the FOV of a single pixel are enhanced. The second prototype consists of two, custom-developed, vision chips integrated with a layer of micro lenses to create 68 artificial ommatidia. Also, it possesses a central-placed microcontroller for on-board

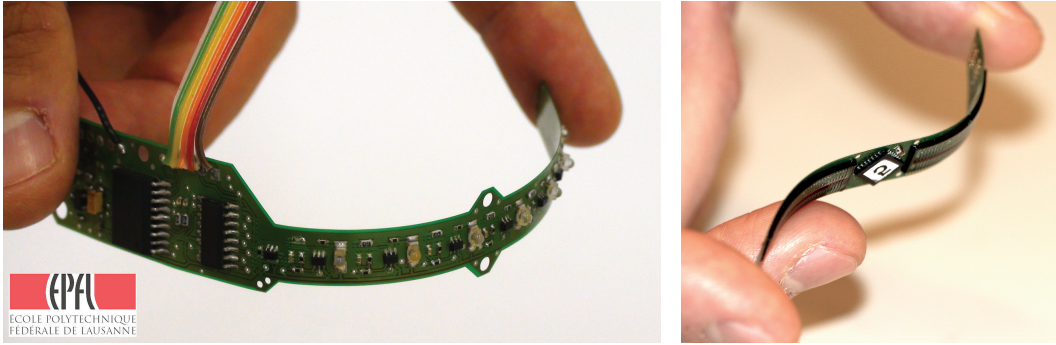


Figure 2.2: Image of the first (left) and second (right) VT prototypes with curved configurations, developed in 2009 and 2012 respectively. The devices recover a planar shape when released.

image acquisition and processing. Every ommatidium incorporates 3 pixels, what allows processing images obtained directly within an ommatidium. The flexibility of both prototypes is achieved by using a flexible Printed Circuit Board (fPCB) made of 100 μm thick KAPTON[®] (DuPont, USA) as the only mechanical support. VT can be either glued, since one of its sides is left free of electronic components, or sewed using holes made at the PCB to attach it to varied substrates (see Fig. 2.3).

The main function of VT is object motion detection and proximity estimation by extracting OF - the pattern of apparent motion of objects in the visual scene caused by the relative motion between an observer and the scene [36, 37]. Irrespective of the complexity of the motion, the OF (\mathbf{p}) can be expressed as a result of its rotational (\mathbf{R}) and a translational (\mathbf{T}) component [38]. In the the 2-D case the OF can be expressed as:

$$\mathbf{p}(\alpha) = \left[-\frac{\mathbf{T} - (\mathbf{T} \cdot \mathbf{d}(\alpha))\mathbf{d}(\alpha)}{D(\alpha)} \right] + [-\mathbf{R} \times \mathbf{d}(\alpha)], \quad (2.1)$$

where $D(\alpha)$ is the distance between the sensor and the object seen in direction $\mathbf{d}(\alpha)$. In the VT prototype, I extract the amplitude p of the motion vector \mathbf{p} from two subsequent images $I(t)$ and $I(t+1)$ using a simplified one-dimensional (1-D) version [39] of the Image-Interpolation Algorithm (I2A) [40]:

$$p = 2 \frac{\sum_n [I(n, t+1) - I(n, t)][I(n-1, t) - I(n+1, t)]}{\sum_n [I(n-1, t) - I(n+1, t)]^2}, \quad (2.2)$$



Figure 2.3: Examples of Vision Tape integration onto various substrates. Wooden cupboard (left), wool glove (middle), polymeric turret of wheeled robot [47] (right).

where $I(n, t)$ denotes the intensity value of the n_{th} pixel at time t . The I2A is a simple, non-iterative algorithm that does not require calculation of high order spatial or temporal derivatives, what significantly simplifies its implementation. In the implemented here version only one division operation per OF vector is required. Although minimum of three pixels are necessary to calculate a single OF vector, what in case of low resolution imager may present certain limitation, this algorithm is suitable for OF extraction with the simple design of the VT prototype. Proximity to objects is estimated from purely translational motion of the imager based on the *motion parallax* principle [41]. Further details of the design and operation of the first prototype of the VT are given in Appendix A.1.

However, the mechanical flexibility of VT introduces a major challenge in the image reconstruction process. It is well known that compound eyes in nature [42, 43] and rigid artificial compound imagers [44–46] achieve an optimal performance when the angle between neighboring sensing units (ommatidia or pixels, respectively) matches the FOV of a single one, *i.e.*, the acceptance angle. In the case of VT, the orientation of the sensing units depends on the shape of the underlying substrate due to its mechanical adaptivity (see Fig. 2.3), and thus, the match between angles cannot be taken for granted.

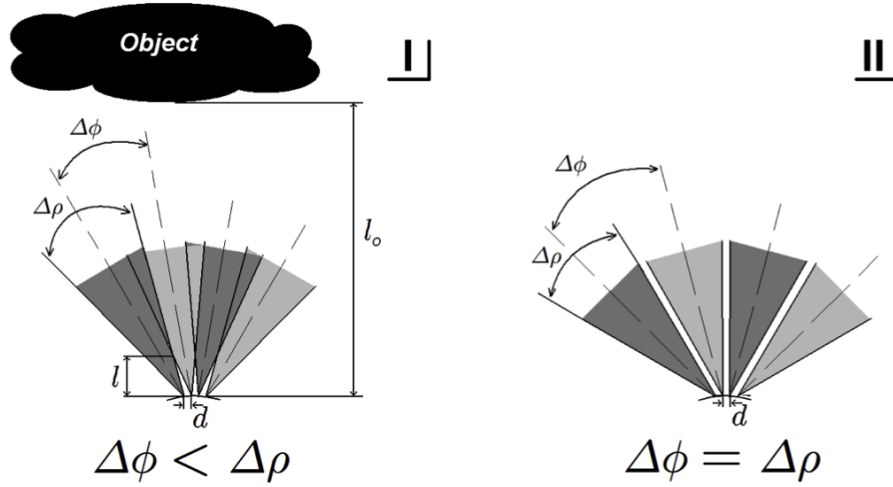


Figure 2.4: Schematic image of four pixels of the VT with different bent configurations (I-II), with FOV of an individual pixel marked in gray color. The two gray intensities are just a guide to differentiate two neighboring pixels. The dashed lines indicate the center of the FOV of every pixel. The two images display the configurations where the pixel-to-pixel angle is smaller than the acceptance angle ($\Delta\phi < \Delta\rho$) and the depth of focus equals l (I) and the pixel-to-pixel angle equals the acceptance angle ($\Delta\phi = \Delta\rho$).

2.2.1 Optical Properties of the Vision Tape

In this section, I detail the main optical characteristics of VT and various related concepts that are necessary to further explain the functionality of the device along this manuscript. Fig. 2.4 displays schematic image of four pixels of a VT with its main optical parameters. Here, $\Delta\rho$ represents the acceptance angle of a single pixel, which can also be considered in this case as its FOV. $\Delta\phi$, named here as the pixel-to-pixel angle, quantifies the difference in angular orientation between two pixels. If it is not explicitly mentioned, this angle lies between two neighboring pixels of the VT. Further, l represents the depth of focus of the device, which states the distance from the compound imager where objects can be faithfully reproduced. l_o represents the distance of the imaged object to the VT, and d is the pixel pitch.

In a compound camera, all the pixels are optically independent. When the FOVs of two adjacent pixels overlap ($\Delta\phi < \Delta\rho$) and the registered objects are farther than the depth of focus equals l (Fig. 2.4 I) the extracted image is blurred. On the contrary, the image yields spatial discontinuities when the FOVs of adjacent pixels are not correlated, that is, when $\Delta\phi > \Delta\rho$. Best image of objects at all distances from the camera can only be obtained when $\Delta\phi = \Delta\rho$ (Fig. 2.4 II), which I will refer here as the optimal relation between both parameters [48]. This relation is a characteristic of the compound eyes

in the visual system of many invertebrates [49]. Therefore, $\Delta\rho$ constrains the spatial resolution of the imager (X) defined as the number of pixels needed to cover 360° of the FOV of the camera ($X = 360^\circ / \Delta\rho$).

In previous works [44–46], where rigid compound cameras were developed, the above-mentioned parameters of the imagers were clearly identified and optimized for their aimed functionality. However, not all the optical parameters of VT can be defined *a priori* due to its mechanical adaptivity. Consequently, the functionality of the camera in terms of image acquisition strongly depends on its shape. By changing the shape of the imager, the pixel-to-pixel angle $\Delta\phi$ is affected, and thus, the preservation of the relation $\Delta\phi = \Delta\rho$ cannot be guaranteed for all possible configurations. This fact arises certain limitations of the VT that we need to consider for its characterization. For instance, it is necessary to establish a correlation of the information from contiguous pixels in order to have a good OF extraction [37], a condition that is specially important for low resolution imagers. If there is no continuity in the global FOV of the VT, such correlation is restricted and compromises the functionality of the device. Thus, only configurations where the pixel-to-pixel angle is equal or smaller than the pixel acceptance angle ($\Delta\phi \leq \Delta\rho$) are considered for the VT. Additionally, the order of the pixels composing an image frame is preserved only in case of convex and flat configurations of the VT, but not in concave curvatures and, especially, in non-uniform ones (see Appendix A.1). Even though it still would be possible to extract OF with concave curvatures, it would require further image processing to reorder the image pixels with no major added value to the functionality of the VT. Therefore, only convex and flat configurations are characterized.

2.2.2 Characterization of the Vision Tape

In this section, I characterize the motion detection and proximity estimation functions of the VT and how these are affected by the adaptive shape of the device. The first VT prototype is used through out these experiments. The experiments are reproduced with the VT prototype bearing four representative shapes namely, the VT in flat configuration (**A**), in optimal optical configuration by fixing $\Delta\phi = \Delta\rho$ for all the pixels (**D**), and two exemplary intermediate shapes fixing the interpixel angles to $\Delta\phi = 0.25\Delta\rho$ and $\Delta\phi = 0.5\Delta\rho$ (**B** and **C**, respectively). To attain these configurations, the first VT prototype is attached to a curved surface perpendicular to the ground with the required radius of curvature. This ensemble is mounted onto a wheeled robot, which provides controlled motion for the characterization. The experiments are carried out in an arena consisting of a flat ground surrounded by a vertical wall. This wall

displays a pattern of vertical black and white stripes to provide high contrast to the visual information acquired by the VT (see Appendix A.2 for further details).

Rotational Component of The Optic Flow

Herein, I characterize motion detection with the VT prototype by describing the rotational OF for the range of studied shapes [50–53], [54, Chapter 5]. For this, the curved VT prototype is rotated around its central axis and OF is extracted. Following (2.1), the rotational OF is linearly dependent to the rotational speed and independent of the distance to the surrounding objects. Thus, the VT can be validated for motion detection in configurations where these two conditions are fulfilled.

Fig. 2.5 (left column) shows the characteristics of the rotational OF for the four studied VT shapes as a function of the rotational speed. OF is calculated over the whole FOV of the imager, *i.e.* 8 pixels. It can be observed that the shape of the OF characteristic changes with the geometry of the imager. The OF value reaches two peaks at about $45.8^\circ/\text{s}$ in both rotation directions. These two peaks limit the linear relation between the rotational OF and the rotational speed. Thus, it defines the range of operation in terms of angular speed of the VT, which is similar for all configurations. For the configuration where $\Delta\phi = \Delta\rho$ and depth of focus $l = \infty$, the peak-to-peak (p-p) amplitude is the highest of all the studied shapes. The value of the p-p amplitude decreases with $\Delta\phi$, reaching 40%, 28% and 23% of the amplitude for optimal configuration **D**, for configurations **C**, **B** and **A** respectively (see Fig. 2.6). As the value of the standard deviation (SD) for all four configurations is similar, the highest sensitivity for the rotational OF extraction is obtained with configuration **D**. The sensor resolution for rotational OF detection can be calculated as $\frac{p-p}{SD}$ and equals, respectively for configurations **D-A**: 19.76, 11.24, 10.75 and 5.46. This confirms that the best rotational OF extraction is achieved for the optimal optical configuration **D**. Thus, the VT shapes where $\Delta\phi < \Delta\rho$ can be considered as sub-optimal for rotational OF extraction.

Proximity Estimation with the Vision Tape

The proximity D to objects can be estimated by extracting the translational OF component and using the *motion parallax* equation (see Appendix A.1, (A.1)). This expression shows that the translational component of the OF is inversely proportional to the distance to the object in relative motion. To characterize this, the VT is moved towards the patterned wall of the experimental arena with constant speed and the OF is extracted separately from the left and right side of the imager. Global OF is calculated as

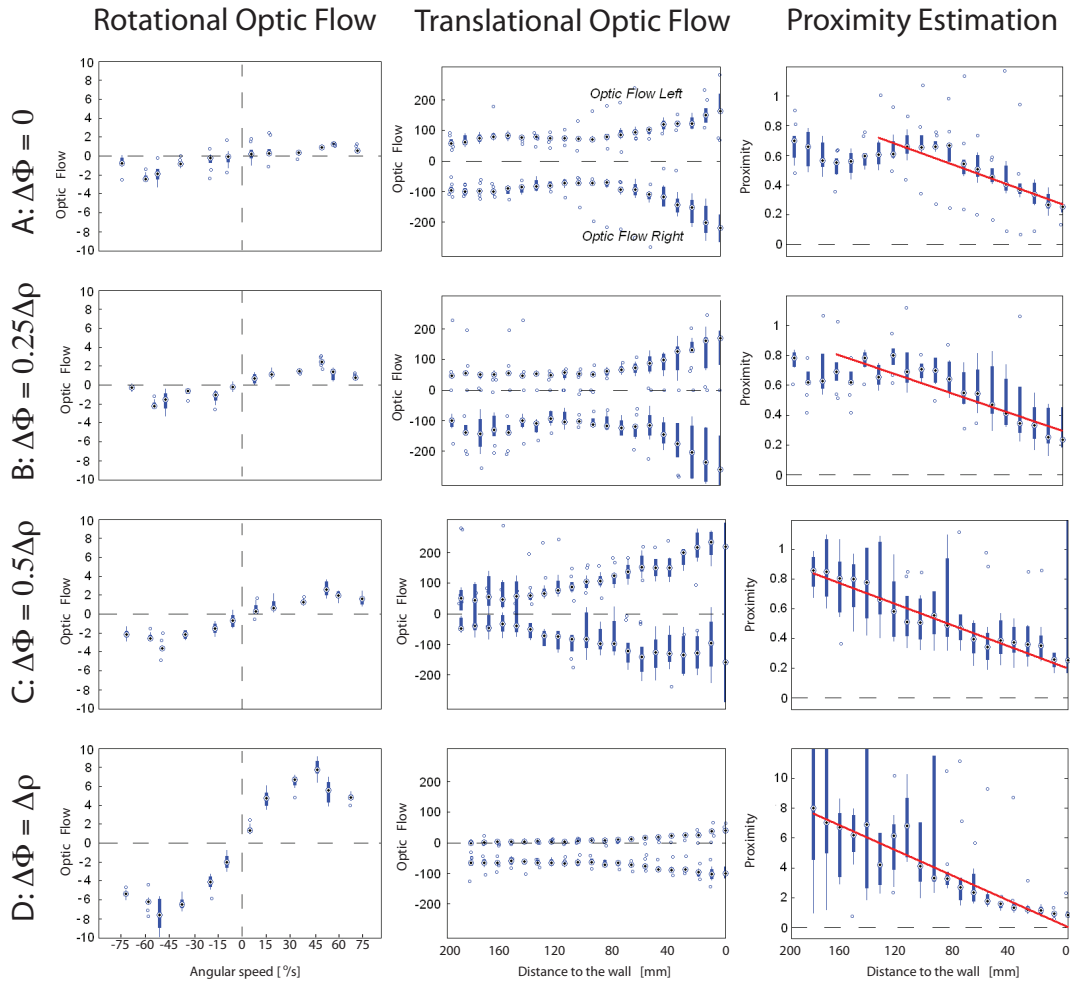


Figure 2.5: Characterization graphs of the VT for motion detection and proximity estimation. The rotational OF as a function of the rotational speed (left column), translational OF (middle column) and proximity values with linear regression applied (right column) as a function of distance to the wall are displayed for the four studied configurations of the imager (in rows). To illustrate the spread of the calculated OF in-between the ten trials of every experiment, the median value, upper and lower 25th percentiles and upper and lower 75th percentiles are presented in the figures. Please, mind that the proximity graph for $\Delta\phi=\Delta\rho$ displays a different scale.

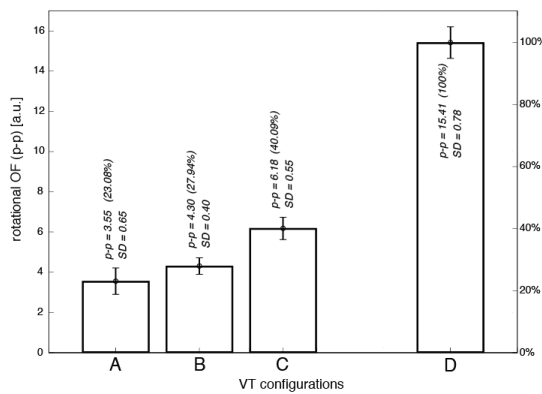


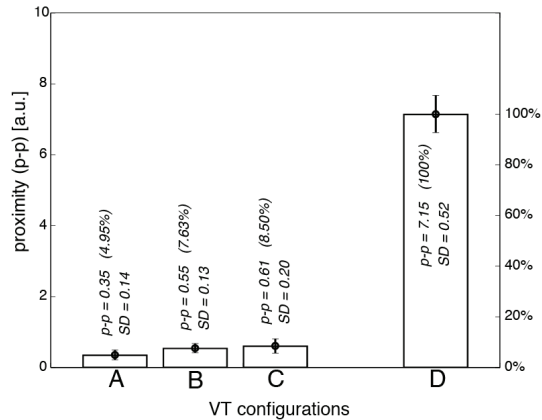
Figure 2.6: P-peak amplitude of the rotational component of the OF and the SD for the four geometrical configurations of the VT. p-p amplitude is expressed in arbitrary units [a.u.] and percentage of the amplitude of configuration **D** (optimal).

a sum of the local ones extracted independently over the left and right region. The result is plotted as a function of the distance to the wall and shown in the middle column of Fig. 2.5 for the four shapes of the VT. It can be observed that the shape of the OF characteristic changes with the geometry of the imager. Indeed, the trend for lower pixel-to-pixel angles is reciprocal with respect to wall distance (Fig. 2.5 **A** and **B**), whereas it becomes linear for $\Delta\phi \geq 0.5\Delta\rho$ (Fig. 2.5 **C** and **D**). I interpret that the change of intensity in a single pixel during the translation toward the wall depends on its relative orientation with the wall. This different orientation affects directly the shape of the translational OF when the imager approaches the object. The orientation is the same for every pixel only in the case of flat configuration **A**. The low values of the translational OF in configuration **D** are caused by the slow change in the sequence of images due to the high global FOV of the imager. However, the trend is more regular and it bears much less noise than configurations with lower pixel-to-pixel angle and far from optimal.

Also, a certain asymmetry between left and right OF values can be observed. I repeated the translational OF experiment with the VT in configuration **C** attached to the robot upside down. It was observed that the asymmetry of the data was also inverted. Indeed, further experiments showed lower average light sensitivity at the photosensors placed on the left with respect to the ones at the right side of the VT, which projects on lower left OF values.

The characterization of proximity estimation as a function of distance to object, in this case the patterned wall, is presented in the right column of Fig. 2.5. To test for linear relation between proximity and distance to the wall, theoretically expected, linear regression (LR) is applied to the median values of proximity (Matlab Curve Fitting Toolbox). The range of operation for proximity estimation is determined for the data intervals that comply with a linear model, *i.e.*, correlation coefficient square $R^2 \geq 0.8$. As a consequence, the range of operation equals 130 mm for VT in configuration **A**,

Figure 2.7: P-p amplitude of the proximity and the SD for the four geometrical configurations of the VT. P-p amplitude is expressed in arbitrary units [a.u.] and the percentage of the amplitude of the configuration **D**.



160 mm for VT in configuration **B** and ≥ 200 mm for VT in configurations **C** and **D**. Within the range of operation, the p-p amplitude is calculated as a difference between the first and the last point value and is presented in Fig. 2.7. The value of SD is calculated excluding the outliers from the data set. Similarly to the rotational OE, the resolution for proximity estimation is expressed as $\frac{p-p}{SD}$ and equals, respectively for configurations **D-A**: 13.64, 3.02, 4.16 and 2.57. Again, the best resolution is obtained for configuration **D**. Moreover, the VT in configurations **A-C** present significantly worse estimation of the proximity, reaching 4.95%, 7.63% and 8.5% respectively of the p-p amplitude of configuration **D**.

2.2.3 Vision Tape - Second Prototype

A second prototype of the VT was developed within the CURVACE (CURVed Artificial Compound Eye) project¹ and aimed at overcoming the perviously encountered limitations, namely the low spatial resolution of the pixels and wide FOV of a single ommatidium. To manufacture the second VT prototype process equivalent to one described in [55] is used. A flat CMOS vision chip is developed and integrated with a layer of micro lenses. The chip-lenses assembly is subsequently glued and wire-bonded to a fPCB that provides mechanical support and electrical interconnection for power supply and read-out. Dicing process, carefully applied between every ommatidium releases the mechanical constrains and provides the stack with a flexibility.

The second VT prototype (Fig. 2.8) incorporates two vision sets of artificial ommatidia and a central-placed microcontroller (dsPIC33FJ128GP802, Microchip) responsible for data acquisition and processing. Every set consists of 34 ommatidia. The chip-

¹The project CURVACE received financial support from the Future and Emerging Technologies (FET) programme within the Seventh Framework Programme for Research of the European Commission, under FET-Open grant number: 2009-237940.

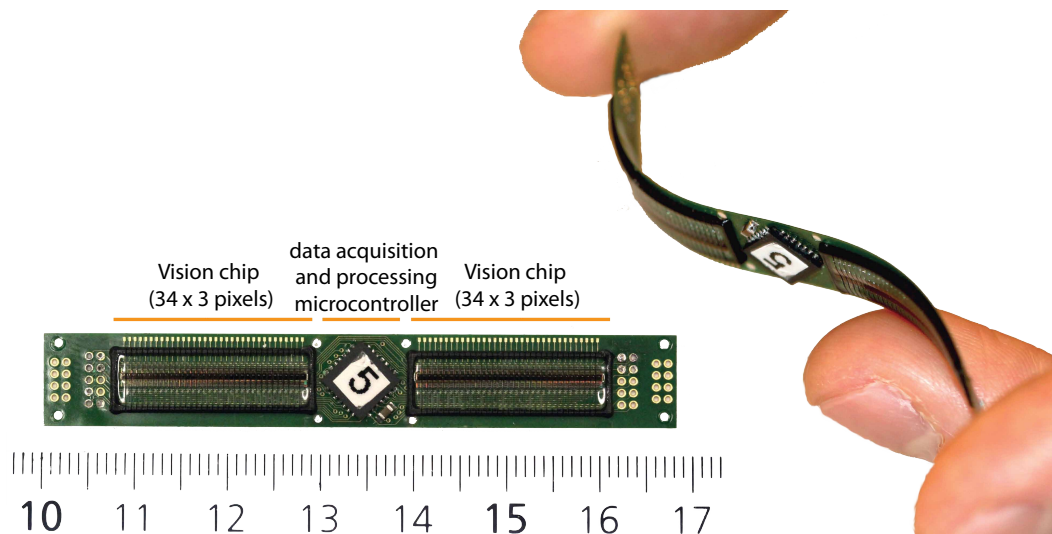


Figure 2.8: Vision Tape - second prototype developed within the CURVACE project. The prototype consists of: two vision chips (34 ommatidia each, 3 pixels within each ommatidium), central-placed microcontroller responsible for data acquisition and processing and a flexible printed circuit board substrate, that provides mechanical support and electrical interconnections.

integrated 10-bits Analog-Digital Converter (ADC) provides digital signal on the DOUT pin, when SYNC pin is excited and clock pin CLK is modulated.

Beside obvious differences between the first and the second prototype in the size of the imager and density of the ommatidia another significant difference can be seen in a design of a single ommatidium (Fig. 2.9). The ommatidium of the second prototype consists of a triplet of photodiodes (pixels) placed under a micro lens, which, although not explored in this thesis, may allow image processing for motion extraction directly within a single ommatidium. The optical characterization of an ommatidium, showed an angular FOV of a single pixel of approximately 4.4° , derived from the angular sensitivity profiles of the photodiode doublets (Fig. 2.10, graph and experiments courtesy of Aix-Marseille University, Biorobotics Dpt, Institute of Movement Sciences). It is measured as an angular width of the bell-shape profiles on the half-sensitivity level. The overall FOV of the triplet ($\Delta\rho$) equals approximately 8.8° .

Also, characterization of the optical parameters of the prototype revealed that the prototype operates under wide range of irradiance from 10^{-7} W/cm^2 to 10^{-3} W/cm^2 (Fig. 2.11, graph and experiments courtesy of Aix-Marseille University, Biorobotics Dpt, Institute of Movement Sciences) following the logarithmic compression scheme

Chapter 2. Vision Tape - Flexible Vision Sensor for Motion Extraction

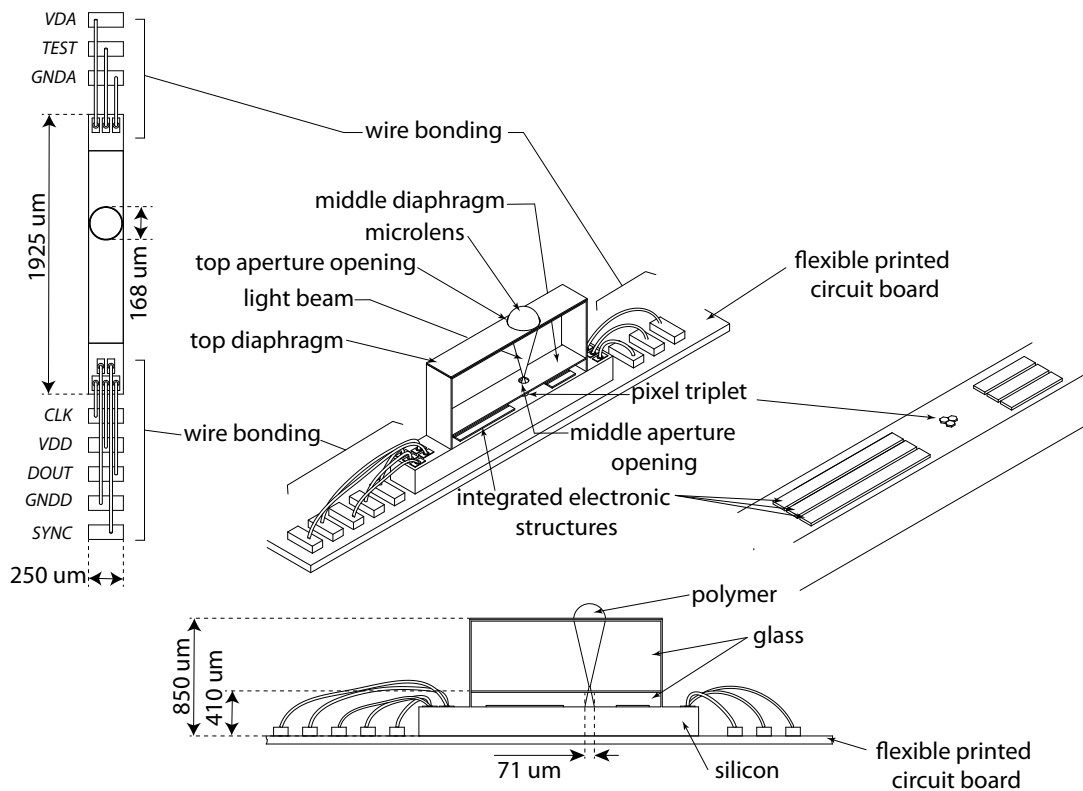


Figure 2.9: Single ommatidium of the second VT prototype. The ommatidium consists of a light sensor (pixel triplet), integrated electronic structures, middle and top diaphragms and a micro lens. The diaphragms are added to prevent optical crosstalk. An ommatidium is bonded with golden wires to a fPCB.

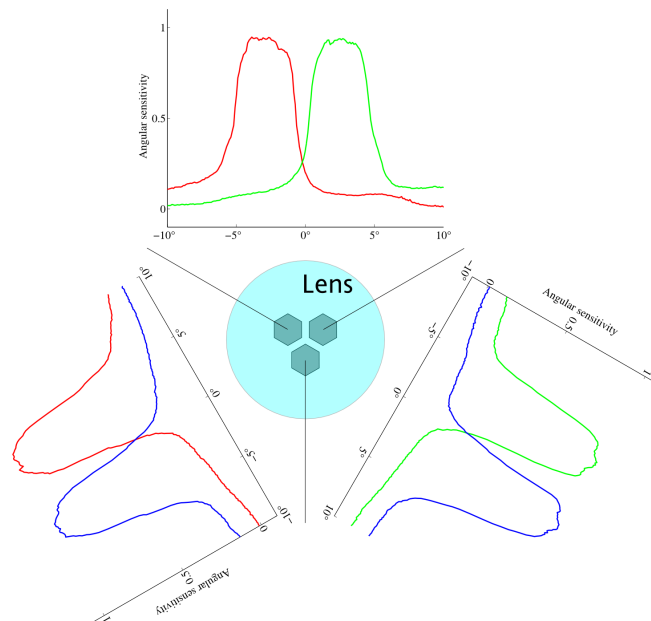


Figure 2.10: Triplet of photodiodes inside an ommatidium of the second VT prototype along with angular sensitivity profiles.

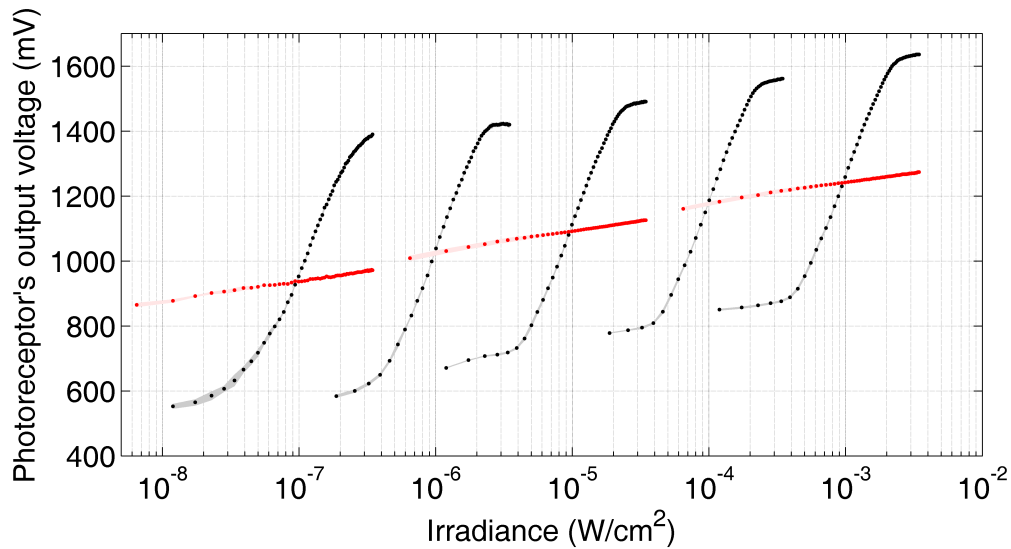


Figure 2.11: Second VT prototype response to irradiance ranging from 10^{-7} to 10^{-3} W/cm^2 . The characteristics present low frequency steady-state response (red) and a high frequency dynamic response (black).

[56]. The output signal from every pixel varies due to the low frequency steady-state response and a high frequency dynamic response.

OF is extracted with the I2A algorithm, the same as used with the first VT prototype, implemented on-board the microcontroller. The algorithm can be applied across the whole imager (34 ommatidia) or a selected patch of ommatidia larger than two units, and may operate under the maximum frame rate of approximately 300 fps.

Here I characterize the rotational component of the OF under four different shapes of the imager, namely the imager in flat configuration ($\Delta\phi = 0$) and three sub-optimal configurations: $\Delta\phi = 0.15\Delta\rho$, $\Delta\phi = 0.3\Delta\rho$ and $\Delta\phi = 0.45\Delta\rho$. Optimal configuration can not be achieved due to the geometry of the imager. In the optimal configuration the 34 ommatidia of one vision chip would have to be bent into an arc of nearly 300° what implies their partial occlusion by the remaining segment of the prototype. To achieve the four configurations, the prototype is attached to a curved surface perpendicular to the ground with the required radius of curvature. This ensemble is mounted on a rotary platform driven by a DC motor, whose supply voltage affect the rotational speed in a linear manner. The experiment is carried out in an arena consisting of a flat ground surrounded by a vertical wall displaying a random chess board pattern. The light of 700 lux illuminance is provided through a three tungsten bulbs placed above the arena.

Chapter 2. Vision Tape - Flexible Vision Sensor for Motion Extraction

In this experiment the OF is calculated across the whole FOV of one vision chip, *i.e.* 34 ommatidia. Only one photodiode, out of the triplet, is used. For every rotational speed data over one minute operation of the sensor are recorded. To acquire the characterization data an OpenLog module is used (<https://github.com/sparkfun/OpenLog>). The OpenLog is a serial logger that automatically writes the received data (UART protocol under maximum bandwidth of 115200 bits-per-second (bps)) to a micro SD card. Due to a low communication speed of the logger the frame rate of the prototype is reduced to 40 fps.

The mean value and SD of the rotational components of the OF are presented in Fig. 2.12. Similarly to the results obtained with the first prototype it can be observed that the shape of the OF characteristic changes with the geometry of the imager. The OF value reaches two peaks at about $137.5^\circ/\text{s}$ in both rotation directions limiting the range of operation of the sensor. It should be mentioned that the range is limited due to the reduction of the frame rate caused by the data logging device. Under higher frame rate an increase of the range of operation would be expected.

The p-p amplitudes for the four configurations and the mean SD are presented in Fig. 2.13. The highest p-p amplitude of 1.46 a.u. is obtained with the imager showing the highest FOV, *i.e.* when $\Delta\phi = 0.45\Delta\rho$. The value of the amplitude decreases with $\Delta\phi$ reaching 1.19 a.u. for the configuration where $\Delta\phi = 0.3\Delta\rho$, 0.96 a.u. for the imager in configuration where $\Delta\phi = 0.15\Delta\rho$ and 0.41 a.u. for the configuration where $\Delta\phi = 0$. The resolution follows the same behavior reaching respectively 4.52, 3.26, 2.49 and 2.2.

2.2.4 Discussion

The results of the characterization of the first VT prototype have shown that the device has a good performance for motion detection and proximity estimation. In optimal bent configuration, the extracted OF possess a high amplitude in a wide range of rotational speeds. On the other hand, the values of the translational OF used for proximity estimation show a more complex behavior. The configurations that are farther from the optimal one show a lower range of operation and a more erratic performance.

We can deduce that some limitations observed in the first VT for its functionality in motion detection and proximity estimation are originated in the characteristics of the utilized prototype. Certainly, the first VT prototype has a very low spatial resolution and wide FOV of a single pixel. Nonetheless, it achieves good performance provided that some assumptions are granted like good environment light and contrast, a curva-

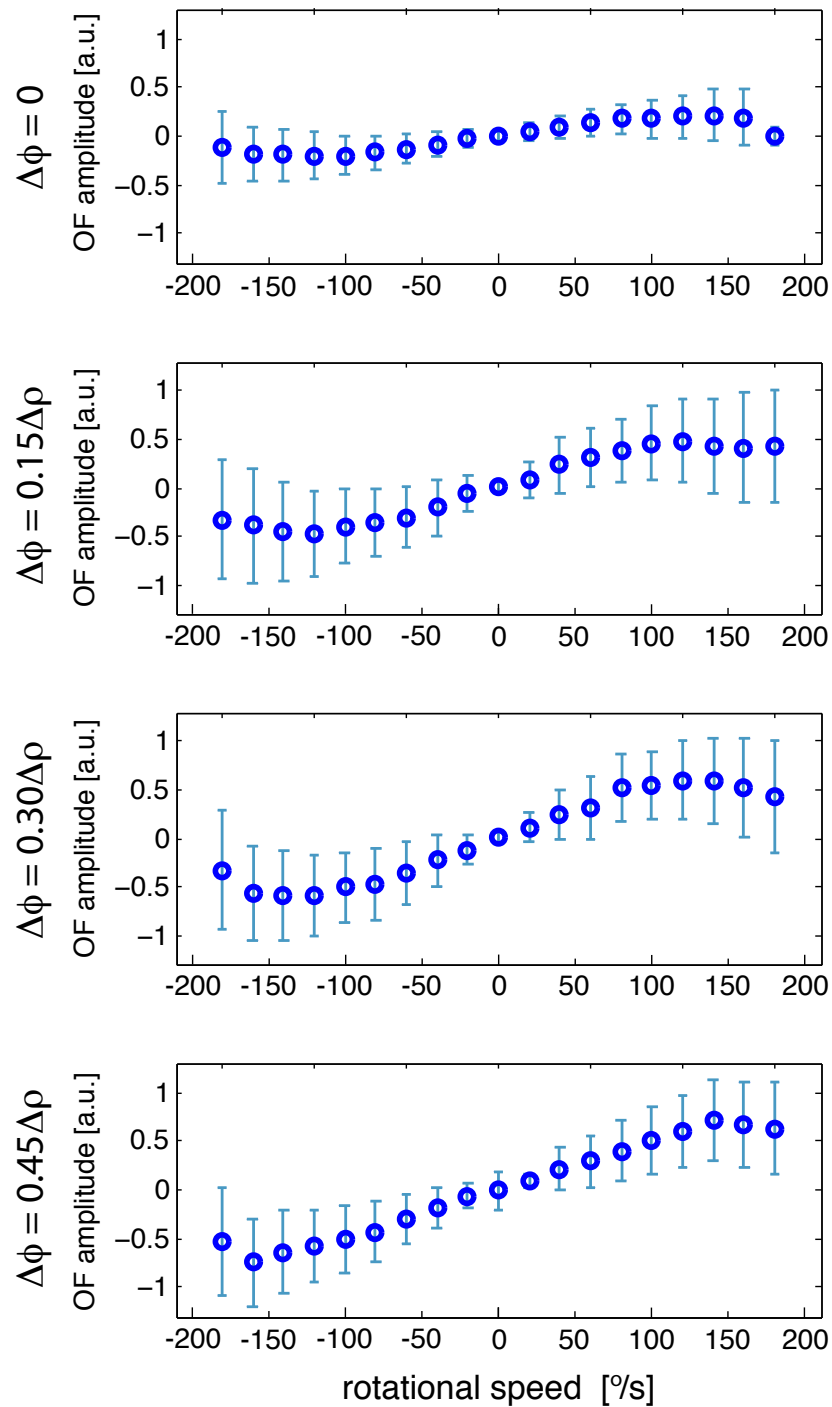


Figure 2.12: Characterization of the second VT prototype. Mean value and SD of the rotational component of the OF under four different shapes of the sensor: flat configuration ($\Delta\phi = 0$) and three sub-optimal configurations $\Delta\phi = 0.15\Delta\rho$, $\Delta\phi = 0.3\Delta\rho$ and $\Delta\phi = 0.45\Delta\rho$.

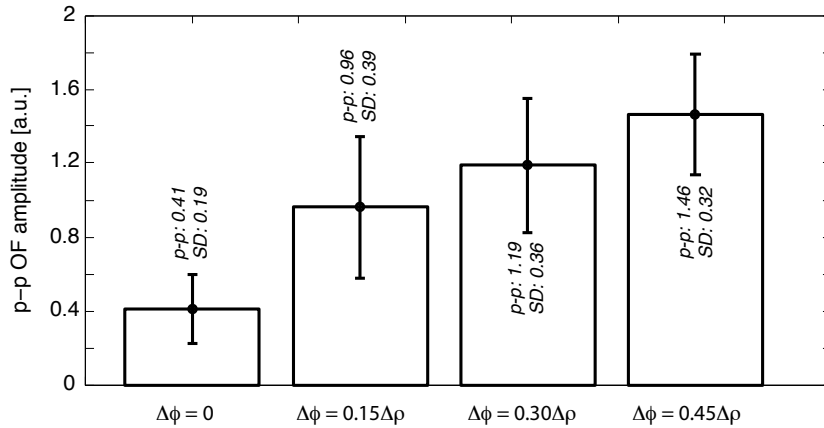


Figure 2.13: P-p amplitude of the rotational component of the OF and the SD for the four geometrical configurations of the second VT prototype: flat configuration ($\Delta\phi = 0$) and three sub-optimal configurations $\Delta\phi = 0.15\Delta\rho$, $\Delta\phi = 0.3\Delta\rho$ and $\Delta\phi = 0.45\Delta\rho$. P-p amplitude is expressed in arbitrary units.

ture between pixels not higher than their acceptance angle, previous knowledge of the underlying surface curvature or constant pixel-to-pixel angle.

Some of the limitations are overcome by developing the second VT prototypes. The evident advantages of the second prototype are the higher number of ommatidia, higher spatial density of ommatidia, and lower FOV of a single ommatidium, as compared in the table 2.1. In particular a higher number of ommatidia allows extraction of more OF vectors within the overall FOV of the prototype. When applying the I2A method over the minimum possible number of pixels, three, up to 11 vectors can be extracted with the second and only 2 with the first prototype. Lower acceptance angle limits the blurring effect caused by the gaussian distribution of the angular sensitivity of a photoreceptor. Moreover, benefiting from the micro manufacturing processes, ommatidia of the second prototypes are smaller allowing more compact size of the prototype under much higher number of the ommatidia units. The compact size and shape of the sensor facilitates its integration with various substrates. Nonetheless, just as the first one, the second prototype suffers from drop of the OF amplitude when operating under sub-optimal configuration.

Table 2.1: Comparison of the two developed Vision Tape prototypes.

	First prototype	Second prototype
ommatidia number [units]	8	2 x 34
number of pixels per ommatidium [units]	1	3
ommatidia density [units/mm]	0.06	0.68
acceptance angle $\Delta\rho$ [°]	30	8.8
maximum length [mm]	136	100
maximum width [mm]	17	10
maximum thickness [mm]	2.5	0.9

2.3 Optic Flow Normalization

The characterization of the first and the second VT prototype shown in the previous sections yields that the shape of the imager affects considerably its functionality for motion detection and proximity estimation. The more the VT is flattened away from the optimal optical configuration ($\Delta\phi = \Delta\rho$ and depth of focus equals infinity), the lower the p-p amplitude and resolution of extracted rotational OF and proximity estimation. Such behavior of the OF amplitude can not be intuitively explained by the change of the FOV of the imager because, as observed in the case of single lens cameras, narrowing (enlarging) the FOV should cause an increase (decrease) of the OF amplitude. Nonetheless, correlation between the amplitude of the OF registered during the rotational experiment and the applied rotational speed is noticeable.

To explain such behavior of the OF amplitude I shall point on the main difference between the compound imager and a single lens camera, *i.e.* the independence of the optical channels (pixels). When narrowing the FOV of a single lens camera, the FOV of a single pixel ($\Delta\rho$) and the angular displacement between consecutive pixels ($\Delta\phi$) are reduced simultaneously. On the contrary, in the flexible compound imager, the reduction of the global FOV is caused by the reduction of the angular displacement between consecutive pixels ($\Delta\phi$) under unchanged values of the FOV of the individual pixels ($\Delta\rho$). This fact has great effect on the perceived spatial and temporal gradient calculated from the intensities of the consecutive pixels during motion of the sensor. To explain the evolution of the gradient during the motion, let's consider the case of a two-pixel compound imager in its optimal configuration ($\Delta\phi = \Delta\rho$, Fig. 2.14 left column) and compare it to the same imager of $\Delta\phi = 0.5\Delta\rho$ (Fig. 2.14, middle column) and $\Delta\phi = 0.25\Delta\rho$ (Fig. 2.14, right column). The sensors, placed in the round arena painted in black (corresponding pixels intensity value 1) and white (corresponding pixels intensity value 0) stripes, are rotated with a rotational speed $\omega(\epsilon)$, where ϵ denotes the angular position of the pixels. The two presented

cases, ϵ_1 and ϵ_2 , correspond to the two angular positions of the pixels, namely the initial position before the rotation and the final position after the rotation by the angle $\Delta\phi$. Δg_{ϵ_1} and Δg_{ϵ_2} denote spatial gradients calculated as a difference between the intensity value of the first and the second pixel, in the angular positions ϵ_1 and ϵ_2 , respectively. Evolution of the Δg gradient as a function of the angular position of the pixels (ϵ) is shown in the three figures (Fig. 2.14 bottom).

It should be observed, that the three discussed cases present three different angular gradient profiles under the same rotation by the angle $\Delta\phi$. The gradient produced by the compound imager in its optimal configuration during the rotation shows the p-p amplitude of value 2. Under the same rotation the compound imager of in sub-optimal configuration $\Delta\phi = 0.5\Delta\rho$ shows a half smaller p-p amplitude of value 1, while in the configuration $\Delta\phi = 0.25\Delta\rho$ only a quarter of the optimal value.

Based on the conducted analysis it should be implied that flattening the flexible imager causes reduction of the gradient amplitude, and hence, the amplitude of the gradient-based OF. Since the drop of the p-p amplitude is linearly proportional to the $\Delta\phi/\Delta\rho$, this ratio could be used to normalize the amplitude of the OF to the one obtained with the optimal configuration. Nonetheless, the angular profile of the signal of the sub-optimal configuration, although being different from the profile of the optimal one, is preserved.

2.3.1 Normalization Procedure

To normalize the OF amplitude to the one obtain under the optimal configuration of the imager a functional relation between the amplitude and the $\Delta\phi/\Delta\rho$ must be found. The relation can be derived through the characterization process applied to the imager in two geometrical configurations only, due to an expected linear character of the function. The normalization factor for the OF is inversely proportional to the value of the derived function at the point of the current $\Delta\phi/\Delta\rho$ ratio. To normalize the OF to the amplitude obtained under an optimal configuration of the imager, the amplitude of the sub-optimal configuration has to be multiplied first, by the normalization factor and second, by the value of the OF amplitude derived with the optimal configuration of the sensor.

For instance, let's apply the normalization procedure to the rotational component of the OF of the two developed prototypes. The LR analysis performed on the p-p amplitudes of the rotational OF obtained during the characterization of the first VT prototype show that the extracted OF under the three measured configurations B, C and D ($\Delta\phi = 0.25\Delta\rho$, $\Delta\phi = 0.5\Delta\rho$ and $\Delta\phi = \Delta\rho$ respectively) indeed follow the

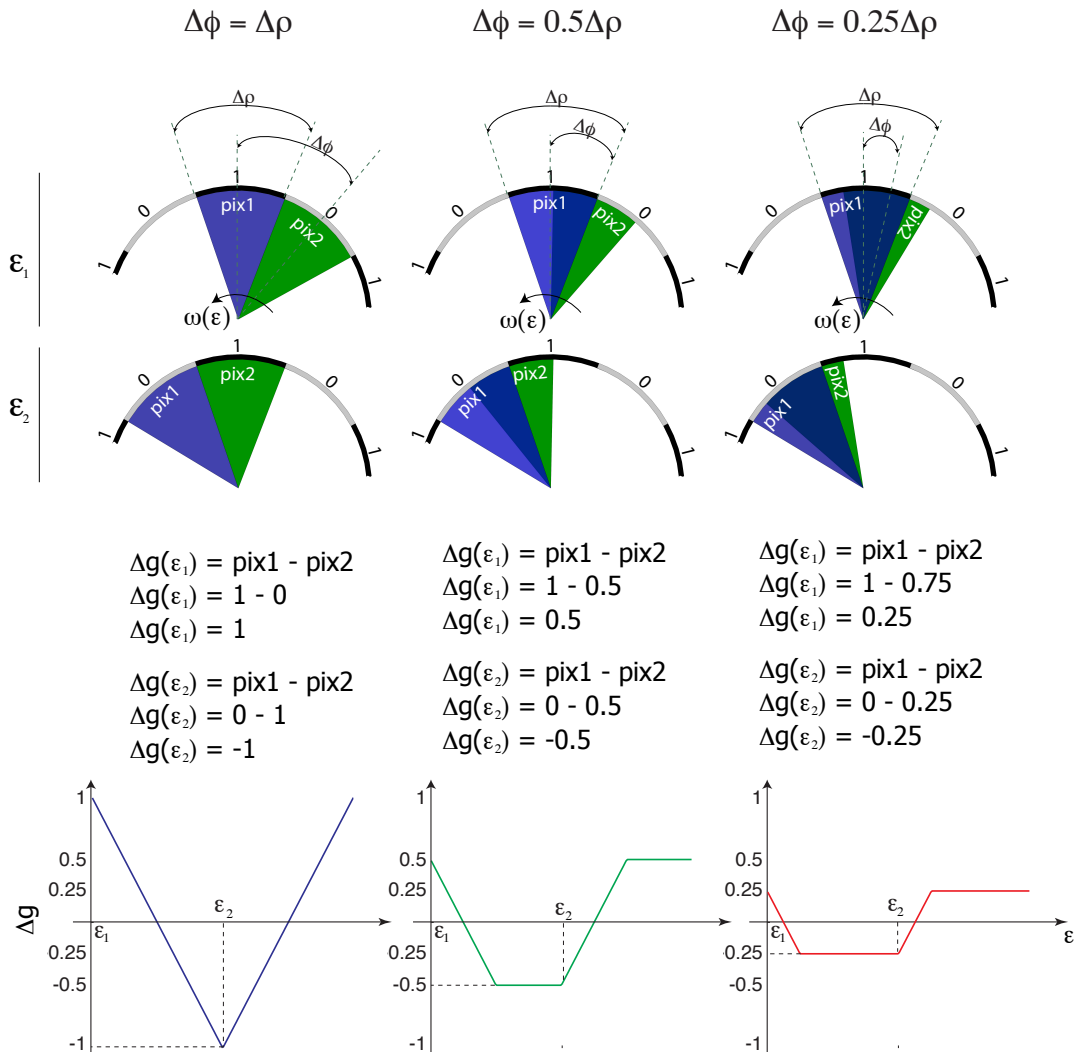


Figure 2.14: Two consecutive pixels (pix1 and pix2) of the compound camera in three geometrical configurations: $\Delta\phi = \Delta\rho$, $\Delta\phi = 0.5\Delta\rho$ and $\Delta\phi = 0.25\Delta\rho$, presented in three columns left, middle and right, respectively. The two presented pixels are placed in a circular arena with walls painted in black-white stripes. The intensity value perceived by the pixels corresponds to the ratio between the black/white stripe covered by the pixels' field of view. Two angular position of the pixels in the arena, the initial ϵ_1 and the final ϵ_2 , after rotation by angle $\Delta\phi$, are presented. Δg_{ϵ_1} and Δg_{ϵ_2} denote spatial gradients calculated as a difference between the intensity value of the first and the second pixel, in angular positions ϵ_1 and ϵ_2 , respectively. Evolution of the Δg gradient as a function of the angular position of the pixels (ϵ) is shown in the three bottom figures.

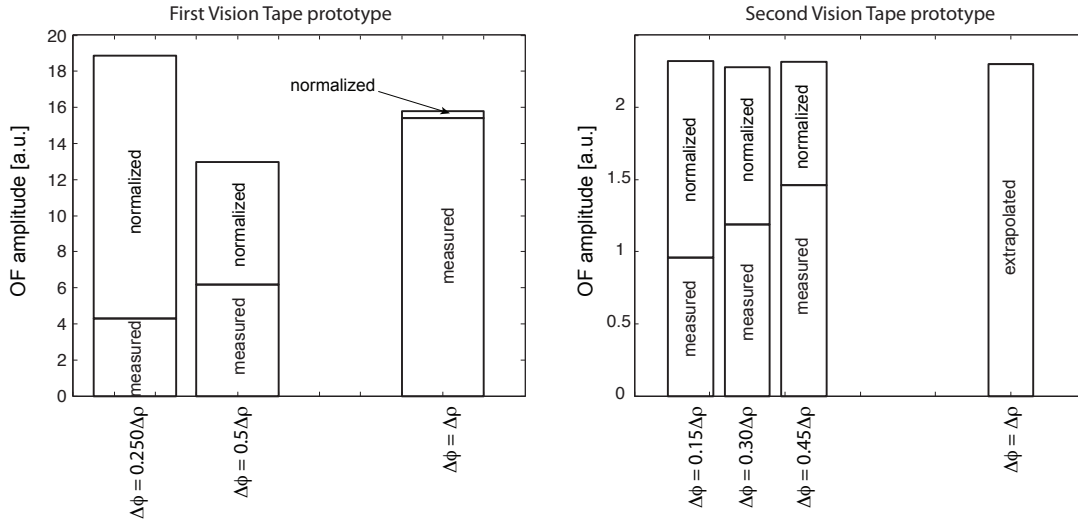


Figure 2.15: P-p amplitudes of the rotational component of the OF derived during the characterization process of the first (left) and the second (right) VT prototype before and after applying the normalization procedure.

expected linear pattern ($OF_{p-p} = 15.33(\Delta\phi/\Delta\rho) - 0.315$, $R^2 = 0.97$). The three corresponding OF_{p-p} values equal 4.3 a.u., 6.18 a.u. and 15.41 a.u.. The normalization factors for the three geometries of the imager equal respectively 0.2843, 0.1361 and 0.0666. The normalized amplitudes approach the optimal one and equal 18.83 a.u., 12.96 a.u. and 15.81 a.u. respectively, as shown in Fig. 2.15 (left). The procedure can be further applied to the second prototype when considering OF extracted under the three measured configurations $\Delta\phi = 0.15\Delta\rho$, $\Delta\phi = 0.3\Delta\rho$ and $\Delta\phi = 0.45\Delta\rho$ ($OF_{p-p} = 1.6(\Delta\phi/\Delta\rho) + 0.7$, $R^2 = 0.99$). The unknown amplitude of the OF for the optimal configuration of the sensor is derived through linear extrapolation of the measured values and equal 2.3 a.u. For these configurations the measured OF amplitude equal 0.96 a.u., 1.19 a.u. and 1.46 a.u. The normalization factors equal 1.052, 0.833 and 0.689. The normalized amplitudes again approach the optimal one and equal 2.32 a.u., 2.28 a.u. and 2.3 a.u., as shown in Fig. 2.15 (right).

2.3.2 Discussion

Despite normalizing the OF amplitude under bent configurations in both prototypes, the rotational component of the OF observed under flat configuration of the imager ($\Delta\phi = 0$) can not be explained with the presented analysis of the gradient. To address this, I should point out the simplicity of the presented analysis, in particular the fact of not including the pixel-to-pixel distance, naturally present in any imager. In the presented case of zero-distance between the ommatidia, the overlap of the FOV of two

consecutive pixels in the flat configuration of the imager is complete. The presence of a finite distance induces an additional gradient due to only partial overlap of the FOV.

As the goal of the VT is to exploit its flexibility and operate under any geometrical configuration, the presented linear approximations can be used to normalize the OF amplitude. Nonetheless, the shape of the imager must be known in order to normalize the OF amplitude. Thus, new solutions to recover the curvature of the device, that is, the orientation of the pixels, must be adopted. Indeed, it is feasible to calculate the orientation of a simplified eight-pixel VT, but this task becomes more complex if the pixel density is increased. An optical calibration procedure [57, 58] could be performed to recover such angle for the whole pixel array or the most significant ones. Nonetheless, a calibration procedure does not provide a solution during dynamic deformation of the imager, like the ones most probably encountered in certain wearable applications. Alternatively, the prototype can incorporate shape sensors to provide information about the shape of the imager, and through this, extract the relative orientation of the individual pixels.

2.4 Conclusions

In this chapter, a novel class of compound vision sensor has been introduced: the Vision Tape. The main special attributes of VT come from its inherent mechanical flexibility, which makes the relative orientation of the pixels dependent on the shape of the underlying substrate. The main functions of this sensor are motion perception and proximity estimation based on the OF principle.

Two prototypes of the VT were developed and described. The first prototype of VT has been built from off-the-shelf elements. It consists of eight photodiodes linearly arranged onto a flexible PCB that acts as mechanical and electrical support, which flexibility allows bending up to 360° in the direction along the pixels. The second prototype has been developed within the CURVACE project and benefits from the micro fabrication techniques. The design of the second prototype preserves mechanical flexibility of the imager by placing the components on the flexible substrate, while, at the same time, increasing number of ommatidia from 8 to 68, their spatial density from 0.06 units/mm to 0.68 units/mm and reducing their FOV from 30° to 8.8° . Mechanical flexibility of the substrate make both prototypes easily integrable into surfaces of various shapes and made of different materials, in particular textiles. Just as the first prototype has been developed to test and prove the concept, the second one can be found useful in robotics and wearable real-life scenarios.

Chapter 2. Vision Tape - Flexible Vision Sensor for Motion Extraction

The prototypes are characterized by extracting the rotational (both prototypes) and translational (first prototype only) component of the OF and by estimating the proximity to an approaching wall. The functionality of the VT has been validated under various shapes from 0° to 270° of the global FOV. It has been shown that the shape of the imager plays a crucial role in the sensor performance. It is observed that the quality of the extracted OF is enhanced for configurations where the pixel-to-pixel angle approaches or matches the acceptance angle. Furthermore, for the case where the shape of the imager is far from optimal, a normalization method is proposed to increase the amplitude of the extracted OF. This method derives the normalization factor based on the current geometrical configuration of the sensor and operates based on the expected linear relation between the shape of the imager (expressed as a $\Delta\phi/\Delta\rho$ ratio) and an OF amplitude. It is easy to implement, robust, and only requires the pixel orientation as input.

3 Shape Sensing

In this chapter I summarize my work on two shape sensors developed for shape monitoring of the VT. First, I discuss the contactless deflection sensor based on the novel sensing method, which allows to perform measurements without a physical contact between the sensor and the substrate in the point of deflection. The method allows to remove the impact of the sensor on the deflection measurement, particularly important when measuring very flexible substrates. Nonetheless, the method presents technological difficulties when integrating with the VT and currently does not allow to obtain high spatial resolution. To address this issue, an alternative method is pursued. The second sensor - the developed hyper-elastic strain gauge - bases on the stretchable-gold-deposited-on-PDMS technology. Thanks to the novel custom-designed read-out strategy, the method supports high spatial and temporal resolutions and significantly simplifies the integration with the VT prototype.

Adapted from the conference proceedings:

[59] *Contactless Deflection Sensor for Soft Robots* (2011)

M.K. Dobrzynski, R. Pericet-Camara and D. Floreano,
Intelligent Robots and Systems (IROS) IEEE/RSJ International
Conference on, pp: 1913-1918
DOI: 10.1109/IROS.2011.6094845

[60] *Contactless deflection sensing of concave and convex shapes
assisted by soft mirrors* (2012)

M.K. Dobrzynski, I. Halasz, R. Pericet-Camara and D. Floreano,
Intelligent Robots and Systems (IROS) IEEE/RSJ International
Conference on, pp: 4810-4815
DOI: 10.1109/IROS.2012.6385505

[61] *Hyper-Flexible 1-D Shape Sensor* (2013)

M.K. Dobrzynski, H. Vanderparre, R. Pericet-Camara,
G. L'Eplattenier, S. Lacour and D. Floreano,
17th International Conference on Solid-State Sensors, Actuators and
Microsystems, *Accepted*

3.1 Introduction

As presented in the previous chapter shape of a flexible compound vision sensor plays a crucial role for OF normalization. To properly calculate the normalization factor, it is desired to monitor, in real time, deformation of the imager down to the level of an angular orientation of a single pixel. However, the problem of real-time shape monitoring in wearable applications is not trivial due to highly dynamic deformations of the textiles caused by body movements. Moreover, designing a shape monitoring system capable of tracking viewing directions of every pixel of the second VT prototype is challenging due to high spatial resolution of the imager (0.68 ommatidia/mm) and high flexibility of the fPCB (<2 N/m).

In this chapter I propose two designs of sensors addressing the challenges of high spatial resolution of the imager, high flexibility of the substrate and the need for a real-time monitoring of dynamic deformation. In particular, I introduce a novel Contactless Deflection Sensing (CDS) concept and demonstrate the possibility of measuring angular displacement without physical contact between the sensor and the substrate at the place of deflection. The concept is based on using a light sensor and a light source, whose light intensity depends on the emission angle in a monotonically increasing way. However, due to the principle of operation, the proposed concept presents a significant drawback, *i.e.*, the possibility of measuring concave deflections only. I overcome this limitation by redirecting part of the light emitted from the source towards convex deflections using a mirror placed above the light source. Nonetheless, practical integration of the CDS with the second VT prototype is complex and leads to poor spatial resolution, if off-the-shelf components are used only. Since this thesis does not solely focus on the CDS development, I do not proceed towards miniaturization of the sensor. Instead, I propose an alternative solution exploiting the already known technology of stretchable-gold-deposited-on-PDMS [62]. Although the developed hyper-elastic strain gauge requires physical contact with the substrate during deflection measurement process, its impact is diminished by high elasticity of the polydimethylsiloxane (PDMS) substrate. Moreover, the developed prototype sensor, in combination with the novel, custom-designed, read-out strategy, allow high spatial resolution when monitoring dynamic shape changes of the second VT prototype.

3.2 Shape Monitoring

Deflection sensors (DS) measure the angular displacement between two points which lie on a common substrate. Since the displacement corresponds to the deformation of the substrate, DS may indicate the stress of the material accompanying the deformation [63, 64]. By measuring the displacement between many consecutive points, shape can be recovered and monitored [65, 66]. Shape monitoring is beneficial in many applications. For instance, in the field of soft robotics, where the need for fast and reliable DS for real-time morphology monitoring is growing [67] shape monitoring could improve control over the morphing process or movement ability of numerous soft robots [68–70].

However, as already mentioned, development of a deflection sensor for monitoring shape of a VT is particularly challenging due the high flexibility of the fPCB, the flexible substrate of the VT. Attachment of a DS to a substrate, typically done by stiff adhesives (Fig. 3.1 A), affects substrate's flexibility by shifting the stress neutral layer towards the sensor. The shift, proportional to the elasticity ratio between the material of the substrate and the material of the DS, should be minimized as it leads to falsification of the deflection measurements. Hence, a desired shape sensor should possess infinite elasticity, or at least one significantly exceeding the elasticity of the VT substrate. Although there already exist a sensor of intrinsic high elasticity, its practical use is limited. The hyperelastic pressure sensor proposed by Park et al. [71] encapsulates conductive fluid in a polymeric channel. By applying strain to the channel its cross section changes affecting the electric resistance of the fluid. However, electrical interconnection between the conductive fluid and the attaching electrodes is challenging and limits its practical applicability.

3.2.1 Contactless Deflection Sensor

Here, I present a DS which does not impact the flexibility of a substrate by performing the deflection measurement using light (Fig. 3.1 B). The operational concept for the DS is based on using a light source, whose light intensity depends on the emission angle in a monotonically increasing way. I validate the concept by building five identical prototype DS. I characterize them along a wide range of deflections. To better understand how the DS characteristics depend on the parameters of the source, the sensor and their geometrical arrangement, I create a model using ray tracing [72, 73]. Finally, I build a system composed of 12 individual DS and apply them to the real-time shape monitoring of a 100 μm thin, flexible polyimide substrate, the same as used in the VT prototypes.

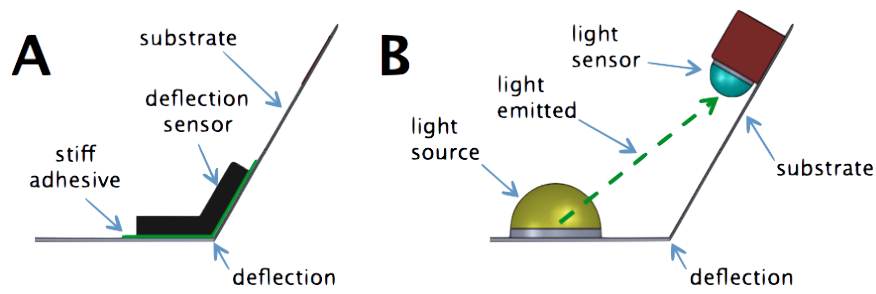


Figure 3.1: A: contact-based deflection measurement concept, common in today's deflection sensors. The contact between the deflection sensor and the substrate affects the substrate's stiffness and therefore, the deflection measurement. B: to overcome this problem a contactless deflection measurement concept is proposed, based on light.

Principle of Operation

The general aim of a DS is to provide information about the angular displacement in-between two points lying on a common plane. The principle of operation for the contactless light-based DS is shown in Fig. 3.2. In this case, the common plane is a deflected substrate and the angular displacement β is measured between the source and the light sensor. The displacement corresponds to the intensity of the light registered by the sensor. This is due to the fact that the source presents a monotonically increasing relation between the intensity of the emitted light and the emission angle α_d . It is worth noting that such a property is common to many off-the-shelf LEDs.

To calculate β , the three following characteristics of the DS must be known:

- the angular intensity profile of the source $f_{source}(\alpha_d)$ - the relation between the intensity of the emitted light and the emission angle α_d ;
- the angular light sensitivity profile of the sensor $f_{sensor}(\epsilon_d)$ - the relation between the light sensitivity and the reception angle ϵ_d ;
- the geometrical arrangement of the source and the sensor around the deflection, d_1 and d_2 ;

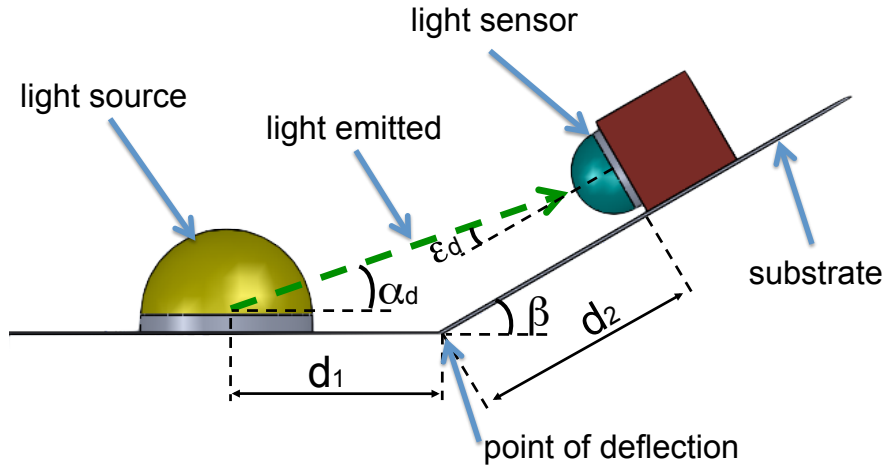


Figure 3.2: Operational concept for a contactless deflection sensor, composed of a light source and a light sensor, both attached to a substrate which is a subject of deformation. The aim of the sensor is to determine the deflection β by measuring the intensity of the light emitted from a light source and captured by the light sensor. The light source is placed at a distance d_1 and a light sensor at a distance d_2 from the deflection point.

The relation O between the light intensity registered by the sensor and the deflection β is expressed as:

$$O(\beta) = f_{source}(\alpha_d) \cdot f_{sensor}(\epsilon_d) \quad (3.1)$$

where:

$$\alpha_d = \beta - \arcsin \left(\frac{(d_2 \cdot \sin(\beta))}{\sqrt{d_1^2 + d_2^2 + 2 \cdot d_1 \cdot d_2 \cdot \cos(\beta)}} \right) \quad (3.2a)$$

$$\epsilon_d = \arcsin \left(\frac{(d_1 \cdot \sin(\beta))}{\sqrt{d_1^2 + d_2^2 + 2 \cdot d_1 \cdot d_2 \cdot \cos(\beta)}} \right) \quad (3.2b)$$

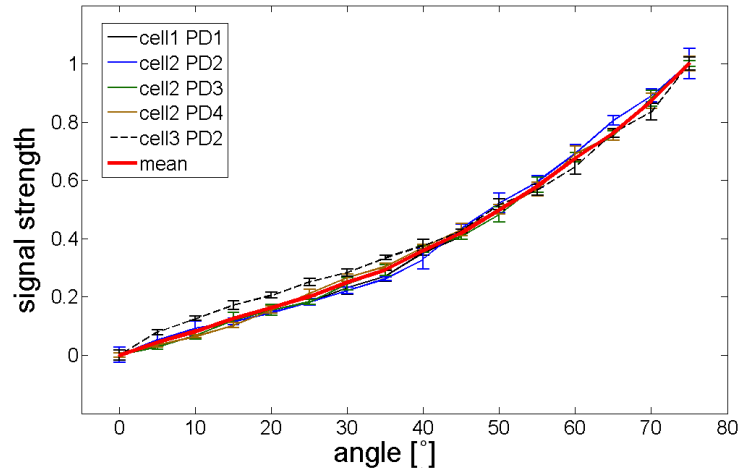


Figure 3.3: Characterization curves of five deflection sensors and a global mean value. Every characterization curve shows mean value and a standard deviation of five tests taken for every of the five DS from $\beta = 0^\circ$ to $\beta = 75^\circ$ with $\Delta\beta = 5^\circ$. Signal strength is normalized to the $[0, 1]$ range.

In order to intensify the signal registered by the sensor, angle ϵ_d should be as close as possible to 0° for every given deflection β . This is because the angular characteristic of a typical light sensor, like a photodiode (PD) or a phototransistor, shows maximum sensitivity around this angle. Therefore, following (3.2), distance d_1 should be as small as possible, *i.e.* the light source should be placed as close to the deflection region as possible, while distance d_2 should be enlarged.

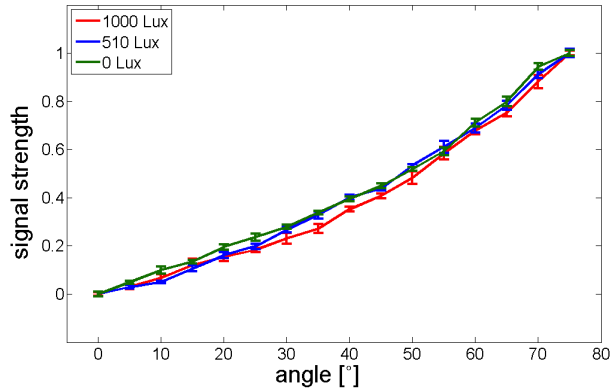
Prototype Realization and Characterization

To validate the concept, five identical prototype DS devices were built using off-the-shelf components. In this realization, I use a HSME C191 LED (Avago) and a PD SFH3710 (OSRAM). The distances d_1 and d_2 are both set to the smallest value possible within the manufacturing limits and equal to 3 mm.

The prototypes are characterized in the range of $\beta \in < 0^\circ : 75^\circ >$ with $\Delta\beta = 5^\circ$, using 16 plastic elements of a known deflection angle, manufactured using 3-D printing technology. The characterization is done by measuring the intensity of the incident light of a DS attached to the plastic elements starting from a flat configuration (0°) and ending with 75° . The characterization is repeated 5 times for every DS.

The mean value and the SD of the light intensity (signal strength), obtained during characterization of all five DS, are presented in Fig. 3.3. The purpose of the graph

Figure 3.4: Dependence of the DS on the ambient light conditions for three ambient light illumination equal to 0 lux, (dark room), 510 lux, (office light illumination) and 1000 lux, (indirect sun light illumination). Signal strength is normalized to the [0, 1] range.



is to visually present the coherence of all five characterization curves and derive a global characterization curve expressed here as a global mean value. The "mean" curve corresponds to the mean value of the signal strength of all measurements for every given angle β . The signal strength is normalized for every characterization to the [0, 1] range. This is to remove the spread brought by the difference in-between the values of electronic components of the 5 prototype DS. The average SD = 0.0172. The obtained average deflection resolution, measured as a relation between the average SD and the maximum signal strength value, is equal to 1.29° .

To exclude the influence of ambient light on the measurement, the level of the ambient light perceived by a photodiode is registered prior to every deflection measurement. This is done by registering the digitalized value of the photodiode output with the LED being switched OFF. Next, the LED is switched ON and the second measurement of the photodiode value is registered. Last, the subtraction of the first measurement from the second measurement is done. The total time for the dual measurement and the subtraction is approximately 2.5 ms (400 Hz). I assume the invariance of ambient light conditions during this time due to the fast data acquisition process. Please note that the possibility of light source ON/OFF control and very fast data acquisition process are essential for reliable sensor operation under various illumination conditions.

The impact of the ambient light on the characteristic of the DS is measured for one, randomly chosen DS, and is displayed in Fig. 3.4. The mean value and SD for five measurements for three different light conditions of illuminance equal to 0 lux (dark room), 510 lux (office light illumination) and 1000 lux (indirect sun light illumination) are presented. The illuminance is measured using a light meter LX-02 (Lutron Electronic).

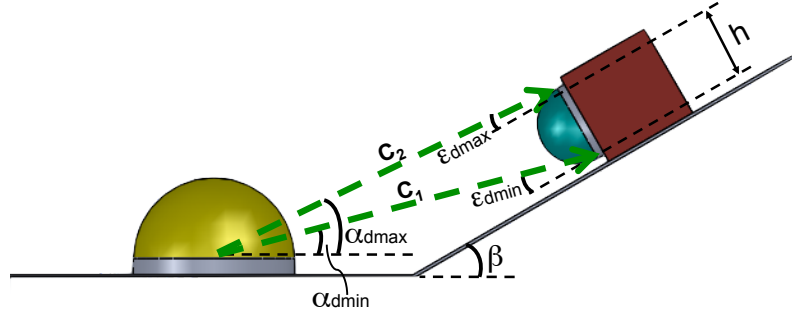


Figure 3.5: The 2-D model of a deflection sensor based on the ray tracing. Every light ray carries an intensity dependent on the emission angle α_d and the angular intensity profile of a light source $f_{source}(\alpha_d)$; while every light ray perceived by a light sensor is weighted according to angle ϵ_d and an angular light sensitivity profile $f_{sensor}(\epsilon_d)$. The model is based on determining the angular ranges for the light emission angles ($\alpha_{dmin}, \alpha_{dmax}$) and light reception angles ($\epsilon_{dmin}, \epsilon_{dmax}$) for given geometrical arrangement of the source-sensor (d_1, d_2, h) around the point of deflection and angle β , following (3.3).

Simulations

As to realize the described DS, components of various characteristics and in various geometrical arrangements can be used, a complete understanding of the DS operation is a necessity. Therefore, a 2-D model is created using ray tracing which captures the relation between the DS characteristics and the signal strength, for every desired deflection β . The model allows to simulate the performance of the device for a particular source – sensor pair, based on the datasheet information and the geometrical parameters.

In addition to the previously described characteristics of the DS, namely, $f_{source}(\alpha_d)$, $f_{sensor}(\epsilon_d)$, d_1 and d_2 , the height h of the photosensitive area of the sensor is added, as presented in Fig. 3.5. Based on these, I calculate four angles for every given deflection β :

α_{dmin} , minimal ray emission angle, as:

$$\alpha_{dmin} = 90^\circ - \arcsin\left(\frac{(d_2 \cdot \sin(\beta))}{c_1}\right)$$

α_{dmax} , maximal ray emission angle, as:

$$\alpha_{dmax} = 90^\circ - \alpha_{dmin} + \arcsin\left(\frac{(h \cdot \sin(90 - \epsilon_{dmin}))}{c_2}\right)$$

Chapter 3. Shape Sensing

ϵ_{dmin} , minimal ray reception angle, as:

$$\epsilon_{dmin} = \beta - \alpha_{dmin}$$

ϵ_{dmax} , maximal ray reception angle, as:

$$\epsilon_{dmax} = 90 - \epsilon_{dmin} - \arcsin\left(\frac{(h \cdot \sin(90 - \epsilon_{dmin}))}{c_2}\right)$$

where:

$$c_1 = \sqrt{d_1^2 + d_2^2 + 2 \cdot d_1 \cdot d_2 \cdot \cos(\beta)}$$

$$c_2 = \sqrt{c_1^2 + h^2 - 2 \cdot c_1 \cdot h \cdot \cos(90 - \epsilon_{dmin})}$$

In the simulation, 9000 rays are emitted from the source R_e (from $\alpha_1 = 0^\circ$ to $\alpha_{9000} = 90^\circ$) with $\Delta\alpha = 0.01^\circ$. Every ray carries information about its intensity given by $f_{source}(\alpha_n)$ and the emission angle α_n . From this pool of rays only those, where $R_e \in \langle \alpha_{dmin} : \alpha_{dmax} \rangle$, are taken. The associated reception angles ϵ_n are calculated $\epsilon \in \langle \epsilon_{dmin} : \epsilon_{dmax} \rangle$, based on which a reception sensitivity S_n for every ray is obtained using angular sensitivity profile of a sensor $f_{sensor}(\epsilon_n)$. Finally, the output light intensity O , registered by a sensor for every given deflection β is:

$$O(\beta) = \sum_{\substack{(\alpha_n \leq \alpha_{rmax}; \epsilon_n \leq \epsilon_{rmax}) \\ (\alpha_n \geq \alpha_{rmin}; \epsilon_n \geq \epsilon_{rmin})}} R_e(\alpha_n) \cdot S_n(\epsilon_n) \quad (3.3)$$

To simulate the DS prototype, I use the $f_{sensor}(\epsilon_d)$ and the $f_{source}(\alpha_d)$ taken from the datasheets of the components SFH3710 (Avago) and HSME C191 (OSRAM), and presented in Fig. 3.6 left and right respectively. The values of d_1 , d_2 and h are measured manually and are equal to 3 mm, 3 mm and 2 mm respectively.

In Fig. 3.7 the experimentally acquired global mean value is compared to the one obtained from simulations. The maximum difference between the simulation and measurements occurs for the angle $\beta = 40^\circ$ and equals to 8.94%, while the average difference for angular range $\beta \in \langle 0^\circ : 75^\circ \rangle$ equals 5.07%. This is due to the simplified assumption of the theoretical model, which neglects the three dimensional character of the light emission and additional phenomena, like light reflection or light scattering, occurring on the substrate surface. Although, by incorporating these phenomenas in

3.2. Shape Monitoring

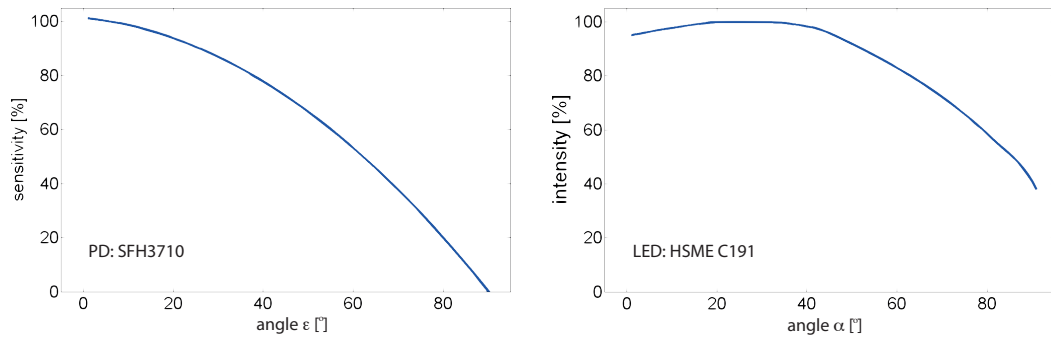


Figure 3.6: Angular sensitivity of the SFH3710 PD (left) and angular intensity profiles of the HSME C191 LED (right). The characteristics are symmetrical with respect to the Y-axis.

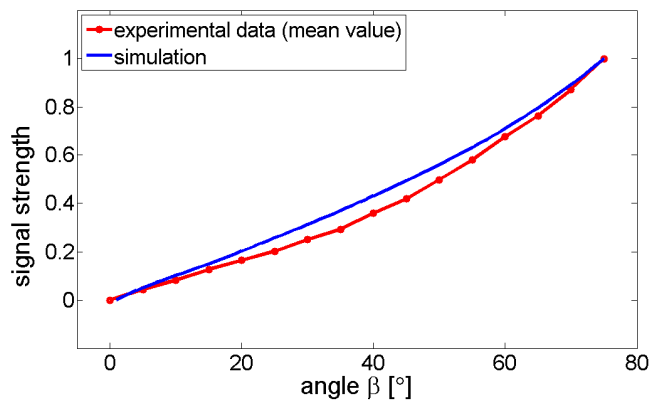


Figure 3.7: Signal strength of the sensor output wrt. angular deflection β for experimentally obtained data and the simulation. Signal strength is normalized to the $[0, 1]$ range.

the model more accurate theoretical prediction can be made, the aim of the model is to facilitate the understanding of the DS operation, and to give hints for the DS realization.

Deflection Monitoring System

The shape of a deformed object can be recreated by measuring the consecutive angular displacement using multiple DSs. Therefore, the application to the real-time shape monitoring of a fPCB, made of $100 \mu\text{m}$ thick polyimide, similar to the one used in the VT prototypes, is described here. The aim of the monitoring system is to provide the information of the overall shape of the system and the angular displacement between the consecutive modules.

The realization is presented in Fig. 3.8B. It consists of 12 prototype DSs, grouped into three cells of four DSs each, as presented in Fig. 3.8A. The DSs are grouped into cells

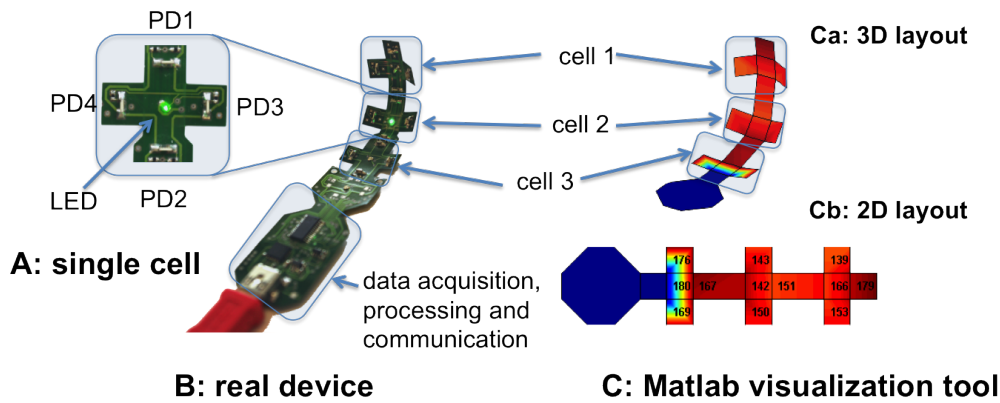


Figure 3.8: Contactless deflection monitoring system attached to flexible surface. The deflection monitoring system is realized using 12 DSs operating based on the proposed concept. A: single sensing cell composed of a central LED light source and four cross-arranged photo sensors (PD1-PD4); B: realized device composed of 3 sensing cells and a data acquisition, processing and communication module; C: Matlab visualization tool composed of Ca: 3-D visualization of a current geometry of the system and Cb: 2-D layout visualizing angular displacement of every DS.

to allow two-directional deflection detection, to decrease the power consumption and to facilitate the geometrical design of the system. Such a modular design allows to enlarge or decrease the number of the cells according to the requirements of a particular application. In addition, the device is equipped with a data acquisition, processing and communication module. A Matlab interface is created (Fig. 3.8C) displaying the global geometry of the system in real-time (Fig. 3.8Ca) as well as current angular deflection of every DS (Fig. 3.8Cb).

Electromechanical design of the system along with the signal flow are explained in Appendix B.1.

Application to Vision Tape

The novel method of deflection sensing presented here allows monitoring of the shape of a VT substrate without an effect to its inherent flexibility. Moreover, the sensor shows no hysteresis, which significantly facilitates data processing and reliability in a long time operation. The experimentally obtained angular resolution equals 1.29° , for deflections from 0° to 75° .

Nonetheless, the prototype device presents drawback which limit its applicability to the VT. The proposed CDS device supports recognition of concave deflections only. Due to the operational principle, the deflection is measured only if the light is emitted

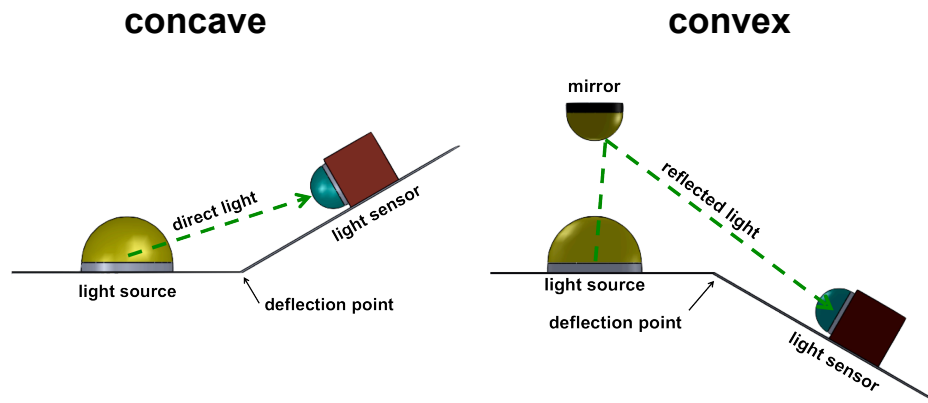


Figure 3.9: Left: operational concept for a contactless deflection sensor composed of a light source and a light sensor, both attached to a substrate that is a subject of deflection. Due to the principle of operation, the contactless deflection sensor in its original configuration can perceive concave deflections only. Right: to overcome this limitation I added a mirror that redirects light towards the light sensor. This factor allows to detect convex deflections.

in the given direction. As light sources capable of emitting light for $\alpha < 0^\circ$ are not common, the angular deflection is limited to $\beta \in < 0^\circ : 90^\circ >$ only. Moreover, even if a source with $\alpha < 0^\circ$ is used, this can lead to subsequently worse results in deflection resolution, as light intensity emitted for $\alpha < 0^\circ$ is typically very low. To extend the angular range of operation of the sensor I propose to implement a mirror above the light source, which redirects a part of the emitted light towards convex deflections.

3.2.2 Concave and Convex Deflection Monitoring - Contactless Deflection Sensor with Mirror

Here, I propose a solution that allows to overcome the problem of limited light perceptibility for convex deflections, by redirecting part of the light emitted from the source with a mirror placed above the light source (Fig. 3.9, right). However, two challenges arise. The first one is to find the profile and the position of the mirror maximizing the range of operation of the CDS and preserving the monotonically increasing relation between the perceived light intensity and the deflection angle. I address this challenge by performing ray tracing simulations that allow to evaluate the potential parameters of the system and to choose the best ones. The second challenge is the manufacturing of a mirror with the modeled profile. This problem is solved by extending the microlens manufacturing method based on surface-tension, proposed in [74] and further developed and modeled in [75], to macroscopic scale. The method promises

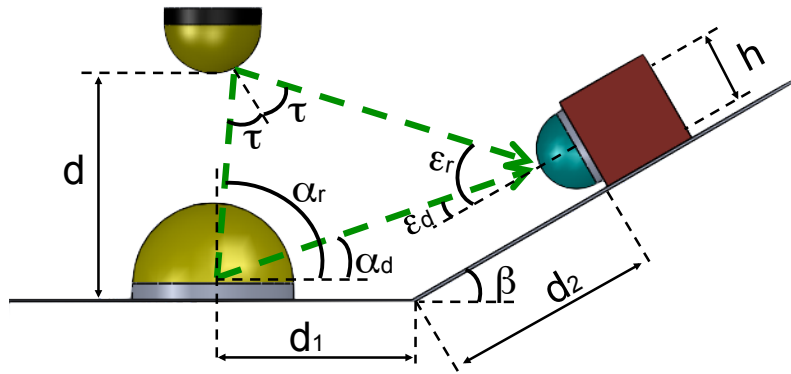


Figure 3.10: The 2-D model of a CDS with integrated mirror based on ray tracing. The light perceived by the light sensor is composed of a direct light and a reflected light. Every light ray carries information about its intensity depending on the emission angle α and the angular light intensity profile of the source $f_s(\alpha)$. The sensitivity of light perception by a light sensor depends on the reception angle ϵ and the light sensor sensitivity profile $f_p(\epsilon)$.

quick and inexpensive lens prototyping and can easily lead to batch-production of the lenses. Subsequently, the lens is coated with a reflective layer of gold to obtain the mirror. Finally, I introduce the mirror to three CDS prototypes and prove that their range of operation can be significantly extended towards convex deflections.

Simulations

The profile of the mirror and all the model parameters (d, d_1, d_2, β, h) are found using the previously developed 2-D simulator based on ray tracing. In the simulator, for every given angle β , $n=900$ rays are emitted from a source from $\alpha_1 = 0^\circ$ to $\alpha_{900} = 90^\circ$ with $\Delta\alpha = 0.1^\circ$. Every ray carries information about its intensity given by $f_s(\alpha_n)$. Only rays that reach the light sensor are kept for calculations. For these, reception angles ϵ_n are calculated and the summed ray intensity is weighted by the sensitivity profile of the sensor $f_p(\epsilon_n)$. In particular, I differentiate between rays reaching the sensor in a direct way with associated angles α_d and ϵ_d , and rays reaching the sensor after reflection with associated angles α_r and ϵ_r . Such division allows one to include the

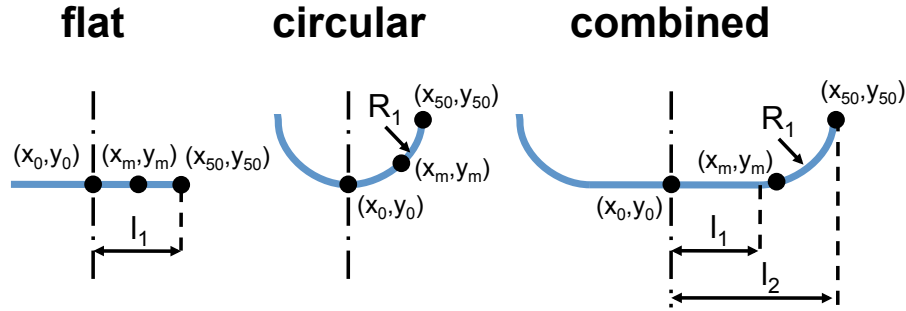


Figure 3.11: 2-D representation of the three tested types of mirror profile parametrized by length of the flat part l_1 , radius of curvature R_1 , and maximum external length l_2 . Every mirror shape is symmetrical with respect to its center. I use 50-points piecewise approximation in a 2-D cartesian coordinate system (x_0, y_0) -to- (x_{50}, y_{50}) to describe the profile of every mirror in our simulator. Such an implementation provides flexibility in manipulating the shape of the tested mirror.

reflectivity index of the mirror $\Gamma \in [0,1]$ in the model. Finally, the output light intensity O , registered by the sensor for every given deflection β equals:

$$O(\beta) = \sum_{\alpha_n=0^\circ}^{90^\circ} \begin{cases} f_s(\alpha_n) f_p(\varepsilon_n) & \text{if } \alpha_n \in \alpha_d; \\ \Gamma f_s(\alpha_n) f_p(\varepsilon_n) & \text{if } \alpha_n \in \alpha_r; \\ 0 & \text{otherwise.} \end{cases} \quad (3.4)$$

Angles α_d , ε_d , α_r , and ε_r are derived analytically based on the geometrical relations presented in Fig. 3.10.

To describe the profile of the mirror I used 50-points piecewise approximation in a 2-D cartesian coordinate system. There are three types of mirror profiles that I test, *i.e.*, flat, circular, and combined flat-circular, as shown in a 2-D representation in Fig. 3.11. These profiles are parametrized by the length of the flat part l_1 , the radius of curvature of the curved part R_1 , and the maximum external length l_2 .

I focus on finding the profile of the mirror and its position maximizing the convex range of operation for the geometry of the CDS prototype proposed previously ($d_1=3$ mm, $d_2=3$ mm, and $h=2$ mm). I test 27 combinations of mirror profile parameters $l_1 \in [1 \text{ mm}, 6 \text{ mm}]$, $R_1 \in [1 \text{ mm}, 3 \text{ mm}]$, and $l_2 \in [1 \text{ mm}, 6 \text{ mm}]$ for three different positions of the mirror above the light source $d \in \{2 \text{ mm}, 4 \text{ mm}, 6 \text{ mm}\}$ against the maximum perceived convex deflection β . The value of l_2 is limited to 6 mm ($2 \times d_1$)

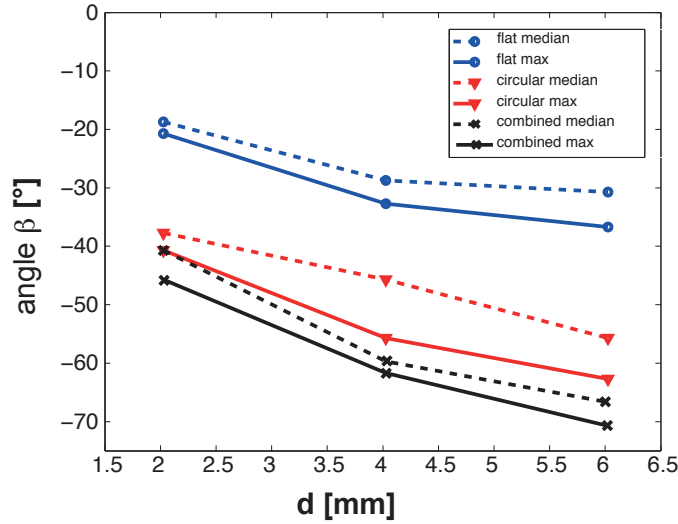


Figure 3.12: Solid line: maximum perceived convex deflection of the three best mirror profiles flat (blue), circular (red) and combined (black), one for each type, depends on the position of the mirror above the source d . Dashed line: equivalent median values. Profile parameters: flat median ($l_1=2$ mm), flat max ($l_1=6$ mm), circular median ($R_1=2$ mm), circular max ($R_1=6$ mm), combined median ($l_1=2$ mm, $l_2=4$ mm, $R_1=1$ mm), combined max ($l_1=4$ mm, $l_2=6$ mm, $R_1=2$ mm).

to guarantee the possibility of the physical implementation of the mirror on the previously developed CDS prototype.

In Fig. 3.12 (solid line) I show how the maximum perceived convex deflection of the three best mirror profiles (one for each type) depends on the position of the mirror above the source. The dashed line presents the corresponding median results. It can be observed that for every profile type, the maximum convex deflection β increases with distance d , which suggests placing the mirror relatively high above the source. The combined profile achieves the best value, outperforming the flat type by approximately 40° and the circular type by approximately 10° . The highest detected convex deflection, $\beta = -70^\circ$, is obtained for $d=6$ mm, $l_1=4$ mm, $l_2=6$ mm, and $R_1=2$ mm.

Fabrication of PDMS Mirrors

A fabrication principle based on the surface tension [74, 75] of PDMS Sylgard 184 (DowCorning) is used to produce polymer lenses bearing the previously modeled profile. Subsequently, to obtain the mirror, I coat the lens with a reflective layer of gold, using Physical Vapor Deposition (PVD).

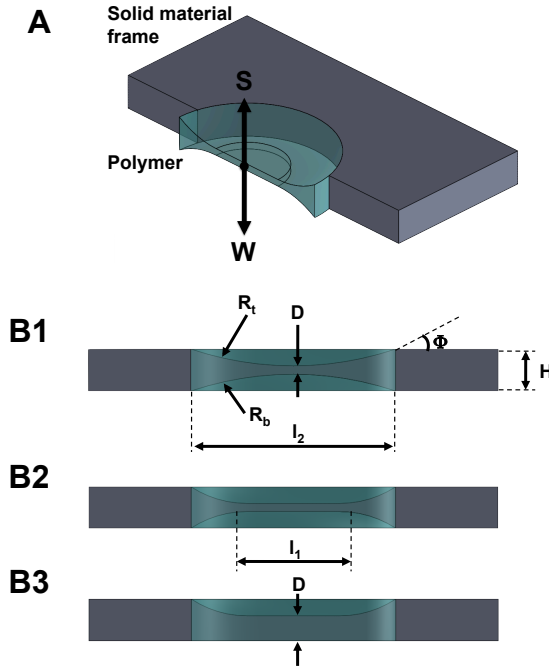


Figure 3.13: A: Schematic diagram of the surface-tension-based lens. Liquid polymer is trapped inside an opening due to an equilibrium between the surface tension force S and the gravity force W . B1: As discussed in [75], the volume $V(H, l_2, R_t, R_b)$ of the induced polymer affects the output profile of the lens (R_t and R_b). In the case of relatively small volume (microlenses), the double-concave profile is obtained. The volume does not affect the contact angle Θ , which is a material parameter. B2: Enlargement of the trapped polymer volume, obtained by enlargement of the opening size l_2 leads to flattening of the central part of the lens (l_1) and subsequently to B3: collapse of the bottom concavity (R_b).

Modeling. The concept of manufacturing the lens is presented in Fig. 3.13A. The uncured polymer (liquid state) is trapped inside an opening made in a solid material frame due to the surface tension force S and the viscosity of the polymer. As presented by Hsiao *et al.*, [75] for micrometer-scale lenses, the lens takes a double-concave spherical shape with radii of curvature R_t and R_b , which can be tuned by modifying the volume $V(H, l_2, R_t, R_b)$ of the induced polymer material (Fig. 3.13B1). However, I hypothesize that the flattening of the central part of the lens could be obtained with a significant increase of the opening size l_2 (Fig. 3.13B2). Moreover, I assume that farther increase of polymer volume will lead to collapse of the bottom concavity, leaving a concave-flat shape of the resultant lens (Fig. 3.13B3).

Based on this hypothesis, I modify the model proposed by Hsiao *et al.* to calculate the volume $V(H, l_2, R_t)$ of the polymer needed to obtain the desired curvature R_t for a given geometry of the opening (H, l_2):

$$V = \frac{\pi}{4} H l_2^2 - \frac{2\pi}{3} R_t^3 + \frac{\pi}{3} \left[2R_t^2 + \left(\frac{l_2}{2} \right)^2 \right]^{\frac{1}{2}} \quad (3.5)$$

Chapter 3. Shape Sensing

For the given radius R_t , I estimate the length of the flatness l_1 as:

$$l_1 \lesssim 2\sqrt{R_t^2 - (R_t \sin(90 - \Theta) + H)^2} \quad (3.6)$$

where Θ is a contact angle between a liquid polymer and a solid frame.

Manufacturing. The lenses are fabricated by following the manufacturing process proposed in [75]. I have chosen PDMS for the lens material due to its universality, transparency, and well known physical parameters. In order to meet the profile of the mirror found in 3.2.2 ($l_1=4$ mm, $l_2=6$ mm, and $R_1=2$ mm), I decided to use a $H=2$ mm thick mild steel frame with a circular opening of $l_2=6$ mm. I measured the PDMS-steel contact angle $\Theta=87^\circ$ and calculated the radius $R_t \approx 3$ mm (3.6) to obtain the expected flatness of $l_1=4$ mm. Therefore, the corresponding PDMS volume equals $V=5.44$ mm³ (3.5).

In addition to the $l_2=6$ mm, I have manufactured $l_2=4.5$ mm lenses to demonstrate the possibility of manufacturing lenses of various diameters. These lenses are shown in Fig. 3.14 A. In Fig. 3.14 A2 the side profile can be seen. In Fig. 3.14 A3, I show the optical effect produced by looking through the lens. The milky edges observed in Fig. 3.14 A4 reflect the roughness of the internal walls of the solid frame.

Mirrors are obtained by coating the lenses using PVD. For this purpose the lenses are attached to a 4" wafer using a thin layer of PDMS and a KAPTON® tape and are placed in an evaporator. Then, 5 nm of titanium is deposited to enhance adhesion followed by a 25 nm layer of gold.

The wafer-attached coated lenses of height $H=2$ mm and diameters $l_2=4.5$ mm and $l_2=6$ mm are shown in Fig. 3.14B1. It can be observed, that the whole surface of PDMS is gold-coated. Fig. 3.14B2 presents the coating quality of the $l_2=6$ mm lens. Although the deposited gold generally presents a smooth and uniform layer, radially arranged cracks and other sporadic imperfections can also be observed.

Measurements. A DropSnake tool [76] is used to measure the profile of the lenses. This tool, which was originally developed for contact angle measurements [77], allows for the piecewise approximation of the lens profile with a defined number of points. The points are placed manually based on visual analysis of the side-view image of the lens,

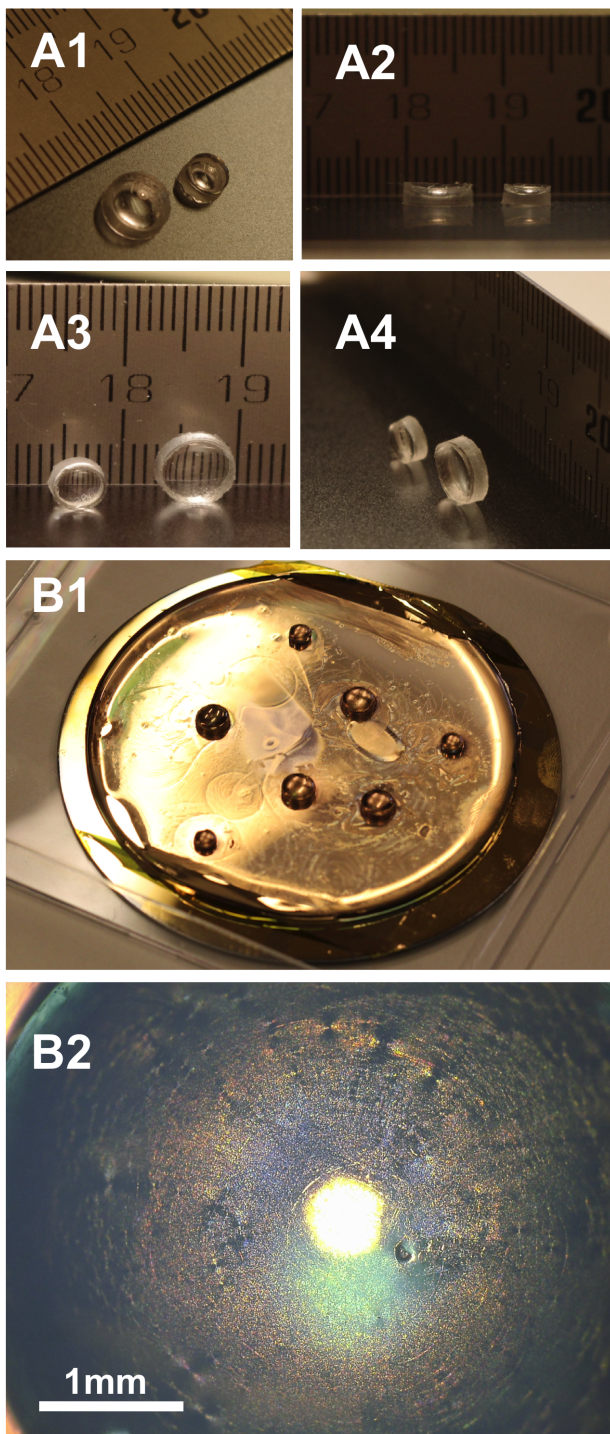
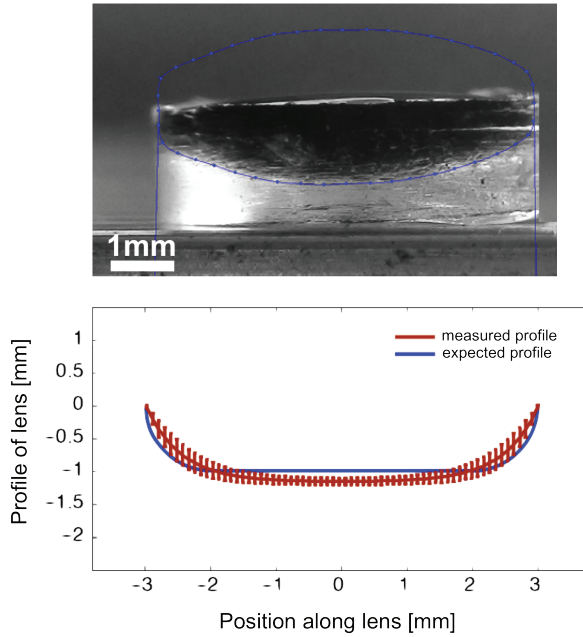


Figure 3.14: The surface-tension PDMS mirrors. A1-A4: circular lenses of height $H=2$ mm and diameters $l_2=4.5$ mm and $l_2=6$ mm. Lens effect can be observed in A3. Milky side-walls in A4 reflect the roughness of the internal walls of the solid frame opening. B1: wafer attached gold-coated PDMS lenses. B2: coating displays small cracks and imperfections.

Figure 3.15: To measure the parameters of the lenses the Drop-Snake tool is used. Top: the tool bases on piecewise approximation of the lens profile on the captured image. Black ink is added to the concavity of the lens to improve contrast. Bottom: mean value and SD of the measured profile of four manufactured lenses (red line) of $l_2=6$ mm and the expected profile (blue line)



as presented in Fig. 3.15 (top). Black ink is added into the concavity of the lens to increase contrast of the image.

In Fig. 3.15 (bottom), I compare the mean value and SD of the profiles obtained from four samples of the $l_2=6$ mm lenses with the expected profile. As hypothesized, the measured profile presents a flat central part between position ≈ -1.75 mm and ≈ 1.75 mm along the lens. Therefore, the length of the flatness, initially estimated to 4 mm, is 0.5 mm shorter from the the expected one.

I estimated the reflectivity index of the mirror for the wavelength of $\lambda=570$ nm to 70% ($\Gamma=0.7$).

Results

To validate the functionality of CDS with mirror, I used the previously developed CDS prototype with further integration of a $l_2=6$ mm mirror 6 mm above the light source using a 3-D printed holder, as shown in Fig. 3.16. Here I characterize three CDS prototypes in the range of $\beta \in [-75^\circ, +75^\circ]$ with $\Delta\beta = 5^\circ$ using 27 plastic elements of known deflection angles. The characterization is done by measuring the intensity of the incident light of a CDS attached to the plastic elements starting from $\beta = -75^\circ$ and ending with $\beta = +75^\circ$. I repeated the characterization five times for each CDS prototype.

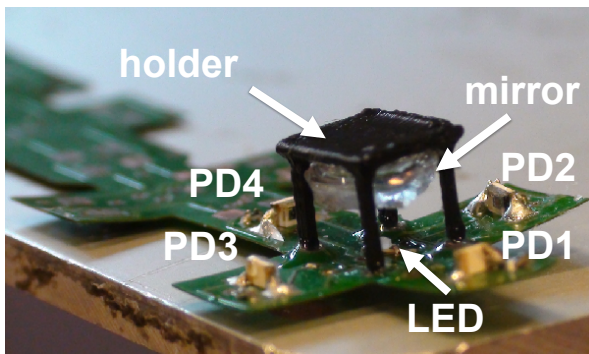


Figure 3.16: CDS prototype consist of an central-placed LED, 4 PD and the $l_2 = 6$ mm surface-tension-based mirror attached 6 mm above the light source with a 3-D printed holder.

The actual highest detected convex deflections is $\beta = -55^\circ$. I observed no light intensity registered by the light sensor for deflections below this angle. Therefore throughout the results, I present measurements for the range of $\beta \in [-55^\circ, +75^\circ]$.

The mean value and SD of the light intensity (signal strength) for three tested CDS are compared to simulation results in Fig. 3.17. I normalize the signal strength to the [0,1] range, for $\beta = 0^\circ$ and $\beta = +75^\circ$ respectively, to remove the variation brought by the differences in the values of the electronic components used in the prototypes. Also, such normalization allows us to compare these results to the ones obtained with the CDS prototype described previously. The average SD=0.00615. The average deflection resolution of 0.8° is measured as a relation between the average SD and the range of operation. Whereas the maximum difference between the measured characteristics and simulations is observed for $\beta=35^\circ$ and equals 16.1%, the average difference in the range of $\beta \in [-55^\circ, +75^\circ]$ equals 8.3%. Although the result of simulation does not capture the exact values of sensors' characteristics, it reflects its essential behavior that allows assessment of the general performance of the sensor before manufacturing.

Application to Vision Tape

The obtained characterization curves confirm the functionality of the CDS for convex deflections, which significantly extends its range of operation with respect to the previously presented prototype. However, spatial resolution of the sensor, in its current instantiation, is limited due to the utilization of off-the-shelf components only. The obtained spatial resolution does not exceed 6 mm, which, in case of an integration with the second VT prototype, provides only three deflection values per vision chip (34 ommatidia). Moreover, complexity of sensor integration onto the VT substrate is not trivial with the CDS without the mirror, and is further enhanced by the need of placing a mirror above every light source and its careful alignment. Since development of shape sensing method is just a step towards the main focus of this

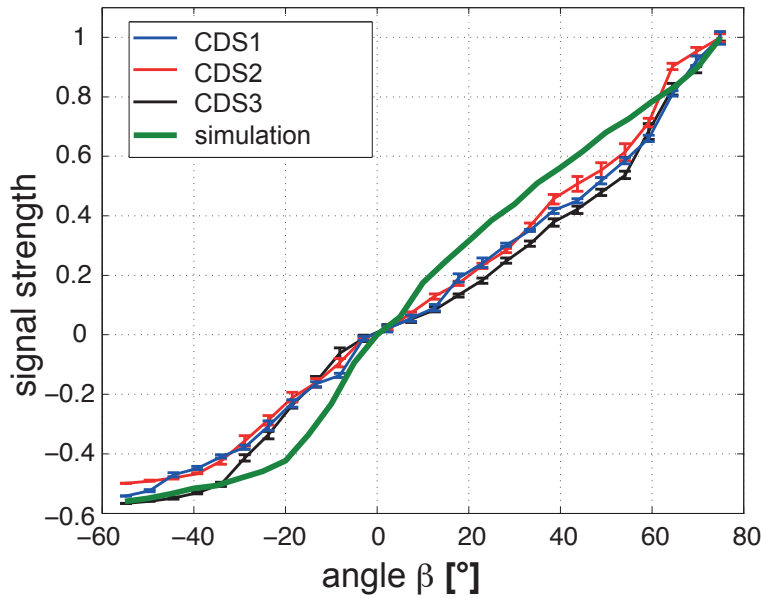
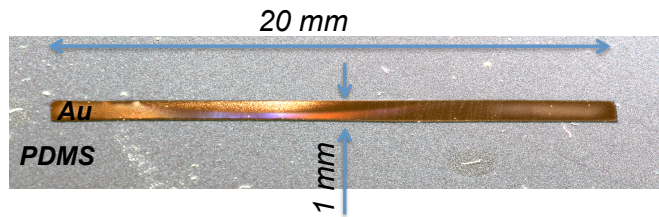


Figure 3.17: Characterization curves of three CDS with mirror integrated showing mean value and SD of four tests taken for $\beta \in [-55^\circ, +75^\circ]$ and simulation results. Signal strength is normalized to the $[0,1]$ range respectively for $\beta = 0^\circ$ and $\beta = +75^\circ$.

Figure 3.18: Sensing element. Stripe of <50 nm thick stretchable gold conductor deposited on a $100 \mu\text{m}$ thick PDMS using PVD.



thesis – the development of the ETA system – I do not proceed towards miniaturization of the CDS sensor and pursue an alternative solution of hyper-flexible strain gauge.

3.2.3 Hyper-Flexible Strain Gauge

To overcome the limitations encounter with the CDS, I develop a hyper-elastic strain gauge, exploiting the already known technology of stretchable-gold-deposited-on-PDMS [62].

Manufacturing and Assembly

The sensing element is a <50 nm thick stretchable gold conductor, deposited on a $100 \mu\text{m}$ thick PDMS by PVD. A titanium layer is added prior to gold deposition to

aid adhesion to the PDMS. I pattern the conductor in a 20 mm x 1 mm stripe using stencil lithography (Fig. 3.18). The Shape Sensor (SS) emerges from bonding the hyper-elastic sensing element to a 100 μm thick fPCB of a VT, using 80 μm thick off-the-shelf double-sided adhesive tape (Fig. 3.19). Eight adhesive elements are laser cut and glued around the fPCB connectors (Fig. 3.19 B) to provide mechanical bonding and to allow stable electrical connection. Shape of the elements is optimized for stress distribution simulated using Solidworks2011 software (Dassault Systems). Please notice, that stress concentrates in the openings left for electrical interconnections and may damage them if brittle interconnecting material is used (Fig. 3.20). Instead, an electrically conductive carbon grease paste (M.G. Chemicals) is used to fill the openings. Finally, the sensing element is aligned and attached (Fig. 3.19 C).

The top view of the SS prototype attached to the back side of the second VT prototype is shown in Fig. 3.21.

Read-Out Scheme

I reconstruct a global 1-D shape of a deformed substrate from a number of linearly arranged consecutive deflections, measured using the sensing element. Indeed, the SS acts as a series of hyper-elastic strain-gauges, which change the resistances with strain [78]. Due to a significant difference between the PDMS-fPCB elasticity, the stretching (compressive) forces act mostly on the PDMS-embedded sensing element, enforcing its elongation (shortening) and affecting little the immanent flexibility of the substrate.

The overall length of the sensor is electrically divided into seven segments by eight equally spaced electrical connectors designed on the fPCB of the VT underneath every fifth ommatidium. The electrical connectors are aligned with the ommatidia and place directly below to preserve maximum flexibility of the free spaces between the ommatidia. Electrically, the SS is represented as series of seven strain-sensitive resistances, R_{x_1} to R_{x_7} , and eight parallel pressure- and temperature-sensitive carbon grease connection resistances, R_{c_1} to R_{c_8} , (Fig. 3.22). I find the individual resistances, R_{x_2} to R_{x_6} and R_{c_2} to R_{c_7} , and the combined resistances, $R_{c_1} + R_{x_1}$ and $R_{c_8} + R_{x_7}$, by consecutive excitation of every connection R_c with a reference voltage U_s , followed by a measurement of the voltage drop U_r on the reference resistor R_{ref} . Such a procedure leads to a system of 28 Kirchhoff's equations (see Appendix B.2 (B.1)), out of which 13 equations (see Appendix B.2 (B.2-B.14)) are linearly independent and can be solved analytically. In this prototype, a 12-bits ADC measures the voltage drop. I perform the measurements and subsequently solve the system of equations on-board a digital signal processing microcontroller (dsPic33, Microchip) with a frequency of 100 Hz.

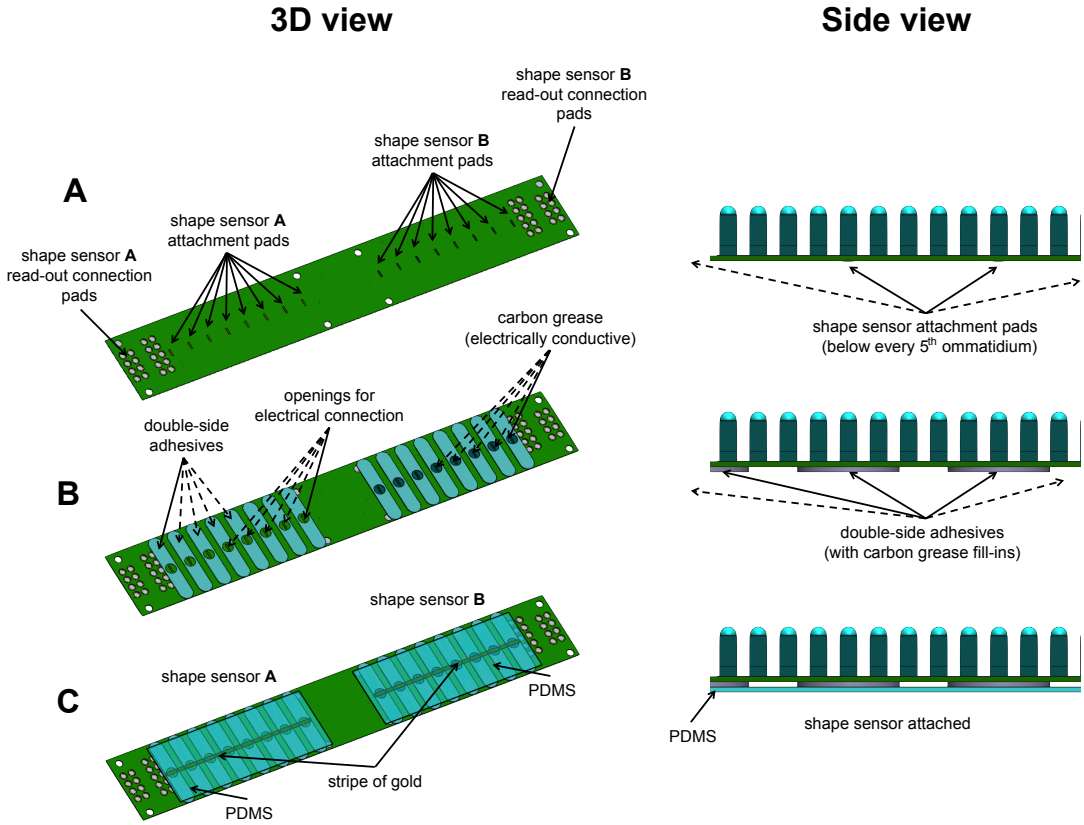


Figure 3.19: The assembly process of the SS with the VT. A: back side of the VT with eight electrical connectors allows to connect two sensing elements (A and B), each underneath a vision chip. The attachment pads are spaced every fifth ommatidium. B: carbon grease-filled voids of a double side adhesive; C: the attached sensing element.

3.2. Shape Monitoring

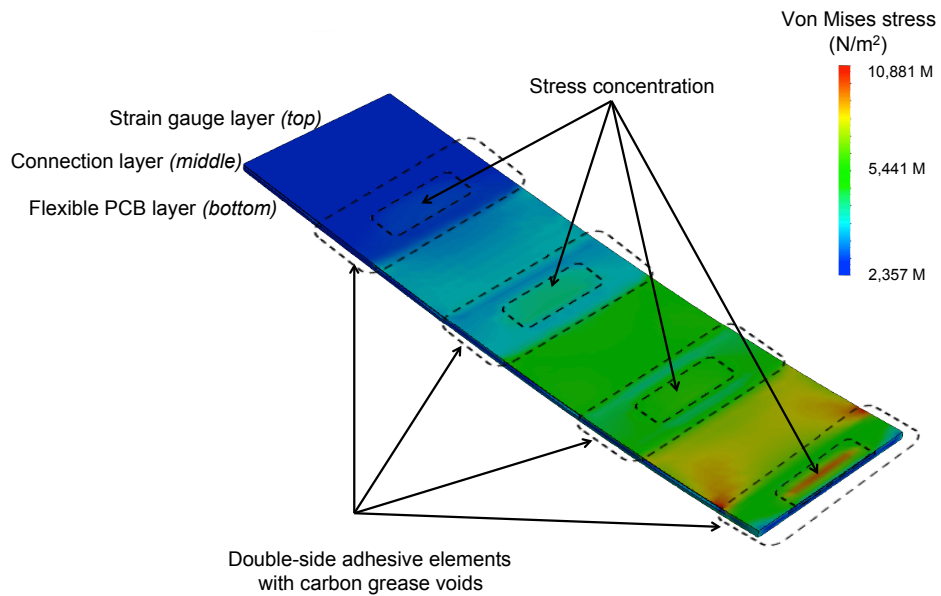


Figure 3.20: Stress simulations of the sensor-VT assembly (Solidworks2011, Dassault Systems). Stress concentrates in the voids left for electrical interconnection.

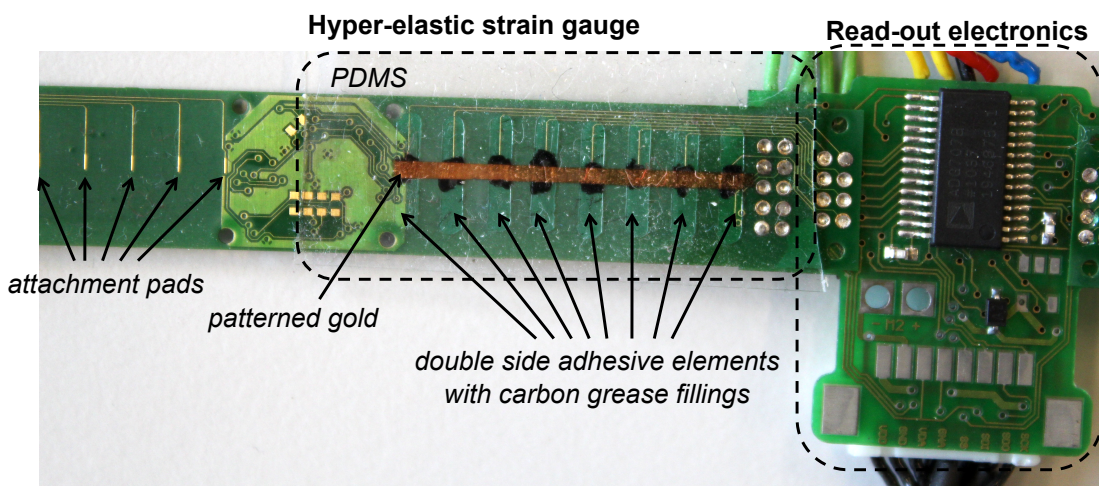


Figure 3.21: Top view of the prototype shape sensor attached to the back side of the second VT prototype. The read-out electronics exploits the proposed scheme allows to collect, process and subsequently send the resistances of the sensing element between the eight attachment pads.

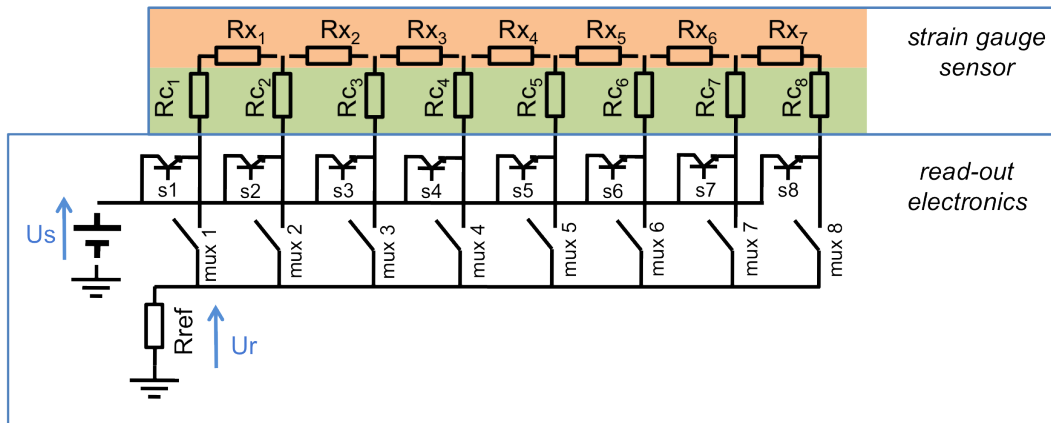


Figure 3.22: Electrical representation of the SS as a series of strain-sensitive resistances R_x and connection resistances R_c , and the read-out electronics

Characterization Setup and Tests

To characterize the SS, I developed an automated setup consisting of a linear stage, two ball-bearing-suspended clamps for fixing the sensor, and the read-out electronics with a USB transceiver for PC data acquisition (Fig. 3.23). The sensor is bent due to linear movement applied by the stage platform. First, I characterize performance of the sensor for a range of positive deflections from $\beta = 0^\circ$ (flat) to $\beta = 35^\circ$ (linear stage platform movement from 0 mm to 20 mm). Correspondingly, each of the seven R_x segments of the SS is deflected from $\beta_s = 0^\circ$ to $\beta_s = 5^\circ$. I restricted the characterization range to positive deflections considering properties of the target application - shape monitoring of the second VT prototype. As discussed in Chapter 2 (in particular in Appendix A), concave geometry of the VT sensor must be avoided, as in this geometry order of the pixels for image reconstruction can not be preserved. Hence, only flat-to-convex configurations are of the interest.

I conducted six consecutive runs of loading and unloading the sensor, collecting for each run ten measurements every *ca.* $\beta = 0.8^\circ$ of angular deflection of the sensor (1 mm of a linear movement of the platform). Before the experiment the sensor has been several times pre-bent to diminish for the presence of eventual material meta-stabilities or irregularities.

Second, the characterization setup is used to perform a fatigue test. The sensor is bent cyclically from $\beta = -35^\circ$ to $\beta = +35^\circ$ under a constant speed of $35^\circ/\text{s}$. To determine functionality of the sensor I test the electrical conductivity between the two extreme connection pads.

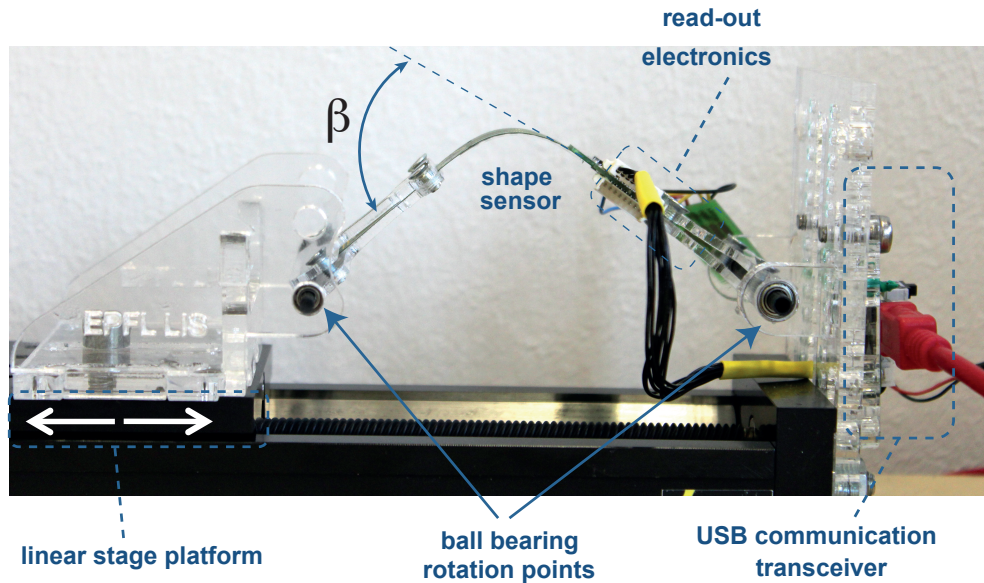


Figure 3.23: The characterization setup, consisting of a linear stage, a ball-bearing-suspended SS fixation, and a USB communication transceiver for PC data acquisition. β denotes the global deflection of the sensor throughout the characterization process. The attached sensor is presented in its final, $\beta = 35^\circ$, configuration.

To measure impact of the attached sensing element onto the flexibility of the VT prototype I use a force sensor SI-12-0.12 (ATI industrial automation) of a force resolution of $1/160$ N. The force sensor is pushing on the two-points-suspended VT substrate vertically with a round pin of a contact surface of 3.14 mm^2 . Stiffening caused by attachment of the sensing element is determined as a difference between the stiffness (flexibility) of the VT substrate with and without the sensing element attached. I perform the measurements three times for one, randomly chosen, sample.

Results

Fig. 3.24 shows the mean value and the SD of the exemplary resistances R_{x_5} (left) and R_{c_5} (right) across the six runs. Despite differences in absolute values, the six remaining resistances R_x and seven remaining resistances R_c display similar characteristic pattern. The density of the points is not uniform due to a projection of the linear motion of the stage onto an angular deflection of the sensor. I calculated mean sensitivity $SR_{x_{5load}} = -27 \Omega/^\circ$ (loading) and $SR_{x_{5unload}} = -45 \Omega/^\circ$ (unloading). While the measured angular resolution of the R_{x_5} strain gauge segment (for loading the sensor) equals 0.2° the mean angular resolution of the whole sensor, measured

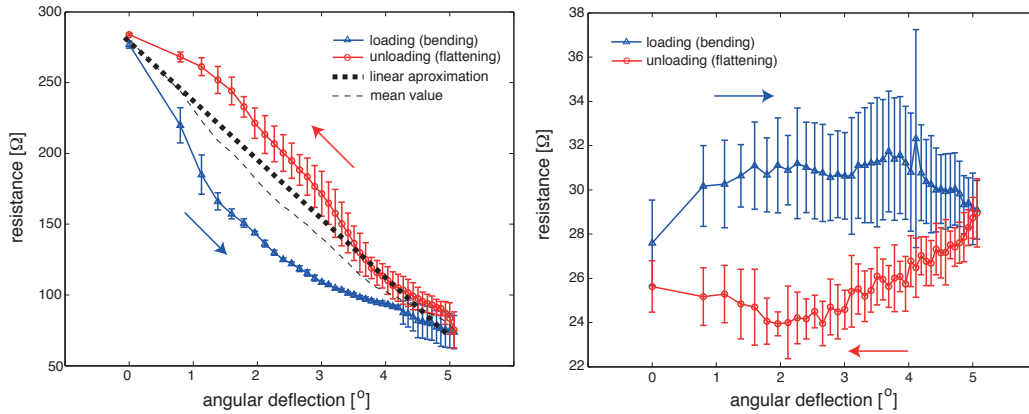


Figure 3.24: The results of the bending tests: output resistance (mean value and SD) vs. angular deflection of resistances for R_{x_5} (left) and R_{c_5} (right). The dashed line shows the mean value between the loading and unloading curves and is added as a guideline for eyes only. The dotted line in the left figure presents linear approximation (slope of $-36 \Omega/^\circ$) of the two curves.

as a mean value across the seven segments, equals 0.22° . Dashed line, illustrating mean value between the loading and the unloading curves, emphasizes the observed hysteresis loop. The hysteresis takes its maximum at 2.55° and equals -0.9° (loading), $+0.6^\circ$ (unloading). Saturation of the sensor takes place for deflections above 5° and has not been reached within the experiment.

The LR analysis performed separately on the loading and unloading curves show that the data complies with a linear model, *i.e.*, correlation coefficient square $R^2 \geq 0.8$. Since the characterization curves present linear behavior in the range of performed measurements, I approximate them with a line of a slope of $-36 \Omega/^\circ$ (Fig. 3.24, left, dotted lines). The slope is chosen as a mean value between the mean sensitivities for loading and unloading the sensor, and varies between the seven characterized sensor's segment (R_{x_1} - R_{x_7}). Due to a difference between the real characteristic and the linear approximation the mean angular resolution of the sensor is reduced to approximately 0.8° .

The R_{c_5} , presented in Fig. 3.24 (bottom), shows the mean variation of the connection resistance throughout the six runs. Despite a low average value ($\sim 30 \Omega$) this resistance would contribute as a noise to the system if not decoupled throughout the read-out process.

To assess performance of the sensor for shape reconstruction a bending test is done using the previously described setup. The sensor is bent (eight times) from $\beta = 0^\circ$

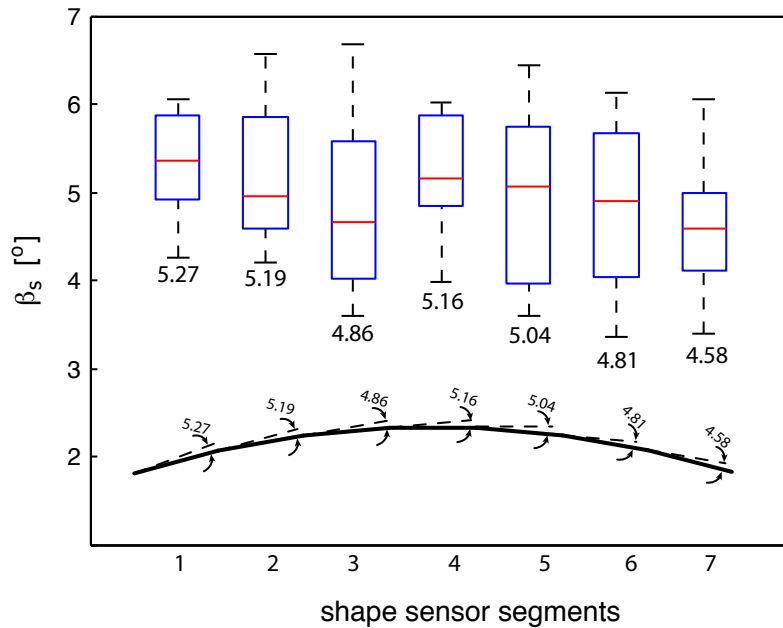


Figure 3.25: Reconstruction of the angular deflections of the seven segments of the shape sensor. Boxplots obtained after eight characterization cycles of loading the sensor into the $\beta = 35^\circ$ configuration. Median values are reported below the boxplots. The shape, the line presented on the bottom, is obtained by consecutive addition of the deflections of the subsequent segments of the sensor.

to $\beta = 35^\circ$ and the seven resistances are measured in the final, 35° , position. From the previously performed characterization and linearization the angular deflection is obtained for each segment separately. Median value and lower and upper quartiles are shown in the seven boxplots corresponding to the angular deflections of the seven segments (Fig. 3.25). The overall shape of the sensor is reconstructed through the consecutive addition of the deflections of the subsequent segments of the sensor.

The performed fatigue test showed sensor functionality during *ca.* 900 cycles proving good robustness against intensive bending. The microscopic evaluation of the broken sensor (Fig. 3.26) showed: (i) sloped, wrt. sensor's axis, micro-cracks on the stretchable gold layer, naturally developed during the pre-stretching phase, (ii) parallel, wrt. sensor's axis, wrinkles on the PDMS layer developed during the fatigue test and (iii) perpendicular, wrt. sensor axis, major cracks of the conductive gold layer which were identified as the source of failure.

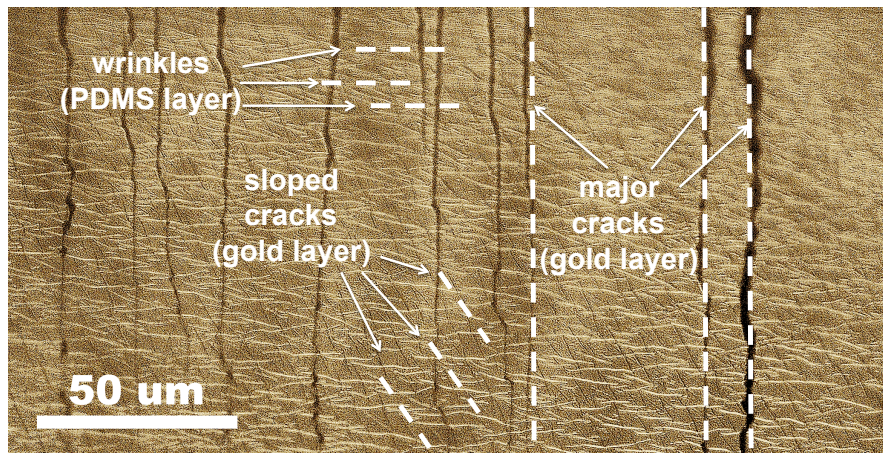


Figure 3.26: The sensing element after approximately 900 cycles of the fatigue test. Apart from the major cracks, perpendicular to the sensor's axis and responsible for the electrical failure, the sloped cracks developed during the pre-stretching phase and the parallel wrinkles caused by the fatigue of the PDMS can be observed.

Finally, observed stiffness change due to attachment of the sensing element to the VT is 0.25 N/m (SD: 0.2 N/m). It is approximately 11 % of the overall stiffness of the VT-SS assembly.

Application to Vision Tape

The hyper-flexible shape sensor prototype presented here is capable of monitoring shape of an underlying substrate in a static and dynamic manner with little effect on its inherent flexibility. Moreover, fabrication of the sensing element and its attachment to the fPCB of the VT prototype are fairly simple. Good spatial resolution of 2.86 mm supports seven individual deflection measurements per vision chip (34 ommatidia).

Nonetheless, in contrary to the CDS, the sensor impacts the flexibility of the VT, increasing its value by 0.25 N/m. Moreover, the sensor shows hysteresis, what impede the process of shape monitoring of a VT by reducing the angular resolution to 0.8° .

3.3 Conclusions

In this chapter I presented two designs of shape sensors custom-developed for, but not limited to, the monitoring of a geometrical configuration of a VT – the contactless deflection sensor and the hyper-flexible strain gauge sensor. The two developed solutions support high flexibility of the VT substrate.

In particular a novel CDS is presented that, in contrary to the contact-based DS, does not affect the flexibility of the deflected substrate. This is due to the fact that deflections are measured using light, relying on a particular property of the light source, namely the monotonically increasing relation between the light intensity and the emission angle. The CDS is validated by building five prototype devices, capable of deflection monitoring with a frequency of 400 Hz. The CDS is immune to ambient light conditions due to active ambient light subtraction from the measured signal. In combination with custom-designed mirror the CDS provides angular resolution of 0.8° , for deflections from -55° to 75° .

A model of the sensor is created allowing to describe the relation between the angular deflection of the substrate and the output from the light sensor. The model characterizes the impact of the parameters of the CDS, such as intensity profile of the source, sensitivity profile of the sensor and the geometrical arrangement of the elements on the output characteristic of the CDS. The simulation results are in close agreement with the experimental data, showing an average error of 5.07%.

Nonetheless, the difficulties with implementing the CDS to the shape monitoring of a VT, caused mainly by the fact of using off-the-shelf components only, made me pursue an alternative approach. Development of a hyper-flexible strain gauge is done using a known technology of stretchable-gold-conductor-deposited-on-PDMS. To measure the shape of a VT, an array of seven hyper-flexible strain gauges is proposed. The main novelty – the custom developed read-out strategy – allows decoupling the strain-sensitive resistances of the strain gauges from the pressure- and temperature-sensitive resistances of the interconnecting pads. The strategy allows quick and accurate read-out of the sensor. The developed prototype device, along with a read-out electronics exploiting the proposed strategy, shows an average sensitivity of $45 \Omega/^\circ$ and average resolution of 0.8° in the measured range of deflections from 0° (flat configuration) to 35° . The impact on the flexibility of the VT substrate is small as the added stiffness does not exceed 0.25 N/m . Moreover, the fatigue test proves the sensor's robustness against intensive bending, withstanding *ca.* 900 loading cycles.

The sensors developed here will be useful in a variety of other applications, such as smart textiles or soft robots due to high flexibility, high resolution and robustness against fatigue.

4 Vibrotactile Feedback System - Design and Control

One of the key question, when designing a wearable ETA system, is how to provide the desired information to a user in a quick, yet understandable manner. In this chapter I describe my work towards the design and control of a head-attached vibrotactile system capable of transferring information quickly and intuitively. As the effectiveness of head-attached vibrotactile displays has never been thoroughly tested, I present the results obtained from experiments with 22 subjects equipped with a display containing 12 coin-type motors equally-spaced in a horizontal plane around the upper head region. My display allows single- as well as multi- motor activation with up to six simultaneously active motors. I identify the minimum and comfort strength of vibrotactile stimulation, measure the precision in perceiving the accurate number of active motors, as well as the precision in localizing the stimuli on the head. While subjects identified the correct number of active motors in 94% of the cases when presented with only one active motor, this precision dropped to 40% for two, down to 5% for five simultaneously active motors. This result strongly suggests to avoid multi-point stimulation, even though the precision of localizing a position of a stimulus on the head is barely affected by the number of simultaneously active motors. Localization precision, however, varies significantly with the region of the head, suggesting that the most front and most back regions of the head should be avoided if high precision is required.

Adapted from the journal article:

[79] *Quantifying Information Transfer Through a Head-Attached Vibrotactile Display: Principles for Design and Control* (2012)

M.K. Dobrzynski, S. Meiri, S. Wischmann and D. Floreano,
Biomedical Engineering, IEEE Transactions on **59**(7), pp: 2011-2018

DOI: 10.1109/TBME.2012.2196433

Awarded 2012 NCCR Robotics Best PhD Paper Award

4.1 Introduction

There are two senses commonly proposed for replacing the missing sense of vision. Sense of *sound* [16–19, 24, 26, 80], the best recognizable one, utilized for communication and, hence, capable of transferring information of high complexity. Sound provides number of possibilities for information transfer, as modulation of frequency or amplitude. Moreover, stereoscopic sound allows creation of volume sensation or a virtual position of a sound source in space. On a higher level sound allows the sensation of music or utilization of voice commands, both intuitively understandable. Sadly, sound, so rich in information, is also a source of navigation by itself. We unconsciously utilize sound cues, picked from the environment, to locate moving objects, possible sources of collisions and to find our way in situations of low visibility [81, 82]. Furthermore, sound-based navigation is enhanced in visually impaired people [83] to a rare extend of echolocation [81].

Touch provides the sensation of texture, allows us to deduce the applied force when grasping objects and to perceive gentle vibrations when applied to the skin. Vibrotactile displays, although capable of transferring information of much lower density, are also popular information-transfer systems for ETA [15, 21–23, 26, 84].

4.1.1 Vibrotactile Displays

Vibrotactile displays are arrays of vibrating actuators that can transfer environmental information via the actuators' amplitude, frequency, waveform or signal duration. Vibrotactile displays can enhance the mobility of blind or visually impaired persons, assisting with spatial orientation and navigation in unknown environments [85, 86], compensating for deficiency in vision [5, 15] and helping in rehabilitation [87–92]. Typically, vibrotactile feedbacks are applied to fingers [21, 22, 84, 93–95] and tongue [96–98] as these are the two most sensitive areas of the human body [99]. However, attaching mechanical devices to hands and tongue reduces object manipulation and speaking capabilities - a major drawback especially for blind or visually impaired persons for whom verbal communication and touch sensation are of vital need. Thus, alternative locations of lower sensitivity have been explored, such as the torso [23, 100], the belt [101], the forearm [92], the back [15, 95] and the head [91]. Compared to the back and torso, information transfer by tactile stimulation of the head has the advantage of easy attachment and detachment of vibrotactile displays [102].

Despite the great effort undertaken so far to understand the underlying principles of vibration perception [103–105] and to formulate general guidelines for designing vibrotactile systems [106], there exists only limited information about optimal dimen-

sioning and control of head-attached vibrotactile displays. In one of the few available studies, Myles and Kalb [107] measured vibration amplitude thresholds for vibration perception at seven head locations for three different frequencies. Their results agree with Weber [108] on the general vibration sensitivity pattern of the scalp, showing the crown to be the most sensitive area of the head followed by the temples and the back head. However, the study of Myles and Kalb lacks information about the precision of stimuli localization. By studying up to 12 sites across the parietal meridian of the head, Gilliland and Schlegel [102] showed that even though their test subjects always perceived the presented stimuli, the rate of successful localization of the stimuli dropped from 93% for 6 sites down to 47% for 12 sites. However, only a small group of subjects (3-4 male and 3-4 female) was tested leading to a low reliability of the obtained results. Thus, there is still a need to quantify the localization precision of head-attached vibrotactile displays. Furthermore, there exists no data yet on the ability to recognize the number and location of multiple simultaneously presented stimuli. Finding the optimal density of motor placements for such multi-point discrimination allows to estimate the quantity of information transfer through the display.

Here I perform an extensive examination of 12 head locations for vibration perception on a group of 22 volunteers, and identify the minimal perceivable strength of detected vibration, the comfort strength for vibration perception, the maximum number of simultaneous stimuli that can be distinguished, and the precision of stimuli localization. The obtained results allow formulating suggestions for the optimal vibration strength and preferable head locations for effective information transfer of head-attached vibrotactile displays.

4.2 Experimental setup

The experimental setup is shown in Fig. 4.1. I used a coin-type vibration motor C0834B011F (JinLong) to provide tactile stimuli. Since this motor is commonly used in mobile phones and pagers, it is optimized for size, power consumption, long-time operation and price. The motor operates on 3.3 V DC and consumes 100 mA of current in continuous mode of operation. Under such conditions mechanical vibrations of 200 Hz were obtained. The vibrations are created based on the unbalanced mass principle. This causes the vibration amplitude being tied to the vibration frequency. Therefore, throughout this chapter, I refer to the amplitude-frequency pair as motor strength and express it as single-pulse energy per motor-skin contact surface area, calculated as:

4.2. Experimental setup

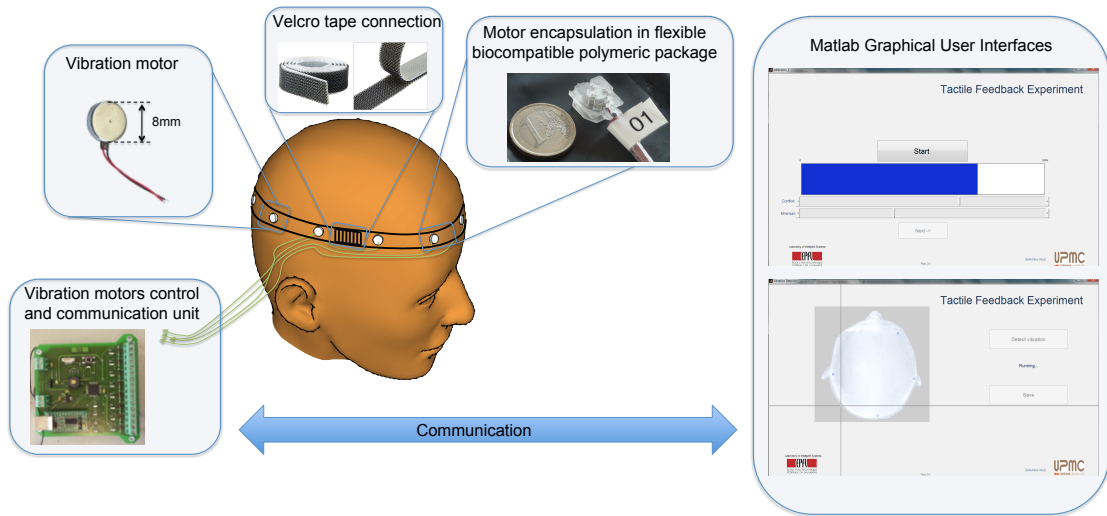


Figure 4.1: Experimental setup for head-attached vibrotactile display studies. The setup consisted of 12 vibration motors encapsulated in flexible biocompatible polymeric package. The motors were attached to the head by the elastic band fixed with velcro tape. The vibration motors were controlled by an electronic unit capable of individual motor activation/deactivation for a given time and strength. This electronic unit was commanded via a Matlab GUI throughout the experiment.

$$E = \frac{U_{avg}^2 \cdot p}{R \cdot S} \quad (4.1)$$

where U_{avg} is the average value of the supply voltage, p is a pulse length, R (constant, equal 33Ω) is the motor coil resistance and S is the contact surface.

A PDMS encapsulation around the motor is realized to prevent skin infections or allergic reactions to the metal case of the motor. PDMS is a biocompatible and easily mouldable polymer common in medical applications [109, 110] resistant to most of the existing cleaning agents. The encapsulation allows regular disinfection of the motor package. The polymer-to-skin contact surface S (4.1) is a 12 mm x 12 mm square. The thickness of the polymer in between the skin and the motor was 2 mm.

An elastic band connected by velcro tape is used to attach the motors to the head. Marks on the band allowed correct positioning of the motors for various head sizes.

The vibration motor control and communication unit operated using a dsPIC33FJ128MC506 microcontroller (Microchip) that is also responsible for com-

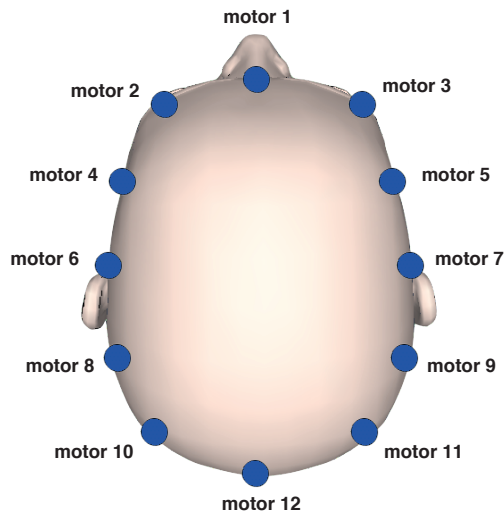


Figure 4.2: Top view of the head with 12 equally-spaced vibration motors. Odd (even) numbers are given to the motors on the right (left) side of the head.

municating with a PC-based Graphical User Interface (GUI). The unit allowed to individually control the strength of the 12 vibration motors. The strength of a motor and, therefore, the vibration sensation is controlled by adjusting the supply voltage U_{avg} (4.1) using Pulse Width Modulation (PWM).

The motors are equally placed around the head (Fig. 4.2). Odd and even numbers are given to the motors on the right and left side of the head, respectively.

4.3 Experiments

For the experiments 11 male subjects of age 23-35 (mean: 26.8, SD: 4.2) and 11 female subjects of age 21-39 (mean: 27.5, SD: 6.5) were recruited. All the subjects were generally healthy, with no history of chronic headaches or epilepsy. The subjects had skills to operate a computer and were working with computer mouse and various types of GUIs before.

The experiments were conducted in a quiet room and supervised by an assistant, following the experimental protocol¹. The subjects sat on a chair in front of a 14" computer screen. The motors were attached by the assistant and adjusted by the subjects, so that a moderate pressure was created between the encapsulated motors and the skin. Before placing the motors on the head a test run was performed to confirm the operation and capability of producing similar tactile outputs by every motor.

¹The experiments were approved by the Swiss Cantonal Commission of Ethics and Human Research of canton Vaud (CER-VD) under the protocol number 304/11 with the decision taken on September 28th, 2011.

4.3.1 Experiment 1: Minimum and Comfort Strength for Vibration Perception

The goal of the first experiment was to determine the minimum vibration perception strength (also referred to as the vibrotactile threshold [107]) and the comfortable vibration perception strength. Due to reported difference between the sensitivity of glabrous and hairy skin [111, 112], and between forehead and back head [99, 107, 108], the experiment was conducted separately for the forehead (involving motors 1-5 according to Fig. 4.2) and the back head (involving motors 6-12). Moreover, both forehead and back head were examined for possible hysteresis in vibration strength perception - the difference in perceiving the vibration strength when increasing the strength from zero-to-maximum and when decreasing it from maximum-to-zero. Therefore, every subject experience four runs - forehead zero-to-max, forehead max-to-zero, back head zero-to-max and back head max-to-zero taking overall approximately 45 minutes (including a 1 min break between the runs).

The strength of the stimuli changed gradually with a 0.58 mJ/cm^2 step. In this experiment three random motors for the forehead and four random motors for the back head were selected for every vibration strength. The selected motors were driven to create three 1 Hz pulses p (4.1) of signal frequency (0.5 s on - 0.5 s off) for every tested vibration strength, keeping the carrier frequency of 200 Hz.

The subjects received a visual feedback representing the currently applied vibration strength. The subjects were asked to indicate the strength for which they started and stopped feeling the vibrations and the strength for which they felt comfortable with. Subjects indicate their choices by moving the sliders presented on the GUI to the position corresponding to the desired vibration strength level (see Fig. 4.1 Matlab GUI - top).

The mean value and the SD of minimum and comfort strength for the 22 subjects are shown in Fig. 4.3. Despite the significant difference in the minimum vibration strength detection obtained for the forehead with respect to the values obtained for the back head while increasing strength from zero-to-max (Wilcoxon rank sum test, $p < 0.001$), this difference diminishes when decreasing strength from max-to-zero (Wilcoxon rank sum test, $p = 0.05$) and disappears for the comfort vibration strength (ANOVA, $df = 3$, $F = 0.92$, $p = 0.435$). Similarly, statistically significant hysteresis is observed in minimum strength for the forehead (Wilcoxon rank sum test, $p < 0.001$), it diminishes for the back head (Wilcoxon rank sum test, $p = 0.01$) and disappears for the comfort strength (ANOVA, $df = 3$, $F = 0.92$, $p = 0.435$).

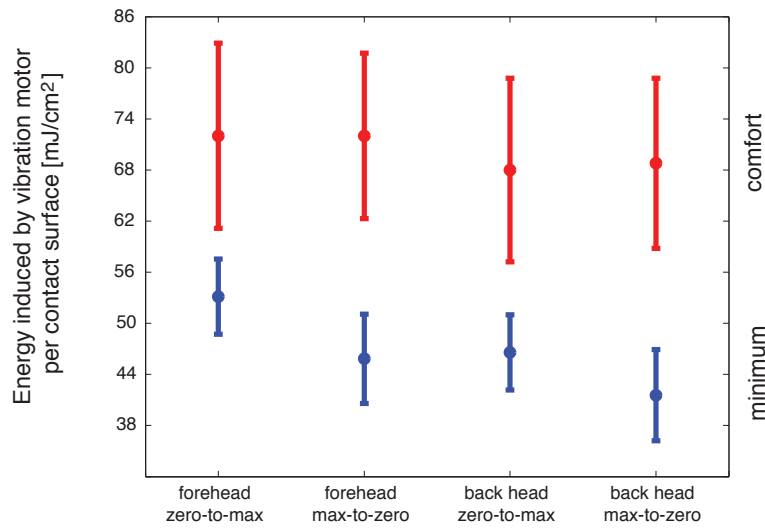


Figure 4.3: Average minimum and comfort vibration strength (\pm SD) identified by 22 subjects for the forehead (motors 1-5) and back head (motors 6-12) with the amplitude increasing from zero-to-max and decreasing from max-to-zero.

Moreover, it should be noticed, that there is a statistically significant difference between the minimum and the comfort regions for all four groups (forehead zero-to-max, forehead max-to-zero, back head zero-to-max, back head max-to-zero) (Wilcoxon rank sum test, $p < 0.001$ for every group). This difference guaranteed that the mean comfort strength (70.84 mJ/cm^2) could always be perceived by all subjects. Therefore, this strength is chosen to be applied in the second experiment.

4.3.2 Experiment 2: Multi-point Discrimination and Vibration Sources Localization

The same group of subjects performing the first experiment was taken for the second experiment, but reduced to 9 female age 21-39 (mean: 26.5, SD: 5.9) and 11 male age 23-35 (mean: 26.8, SD: 4.2) due to an unavailability of 2 female subjects. The second experiment was conducted approximately two weeks after the first one. Thus, subjects had already approximately 45 min of experience with the experimental setup.

The GUI used in the second experiment was different from the GUI presented to the subjects during the first experiment both in graphical design and functionality. In the second experiment the GUI displayed the top view of the human head and the subjects were asked to click on the head location corresponding to the place where

they perceived the vibration (Fig. 4.1 Matlab GUI - bottom). Neither the number of simultaneously active motors nor their location were given to the subjects before the experiment or displayed on the GUI. Subjects had no feedback regarding the correctness of their answers during the experiment. It should be noticed, that subjects were not explicitly asked to identify the number of currently active motors.

Subjects were exposed to 150 randomly generated sequences of motors divided into 3 consecutive runs. In every run the strength of vibrations was changed, starting with the comfort vibration strength (70.84 mJ/cm^2) in the first run, continuing with a lowered vibration strength of 60.21 mJ/cm^2 in the second run (comfort vibration strength -15%) and ending with an elevated vibration strength of 81.47 mJ/cm^2 (comfort vibration strength +15%) in the third run. The $\pm 15\%$ range was a rough estimation of the SD of the comfort region (see Fig. 4.3). There was a one minute break given to the subjects between every run.

In every sequence there were between 1 and 6 motors simultaneously active. Subjects experienced every sequence 6 times (6 pulses of 0.5 s on - 0.5 s off) after which 15 s were given to indicate the vibration sources on the GUI. Both the number of motors and the motors' numbers were randomly generated with uniform distribution for each sequence and are unknown to the subjects and the assistant. The subjects were allowed to request a new sequence anytime within the given 15 s. Thus, the total time of the experiment varied between 30 to 60 minutes.

The first two objectives of the experiment were to determine the maximum number of simultaneously active motors successfully perceived by the subjects and to assess the impact of the vibration strength on motor number identification. Therefore, the actual number of active motors in every sequence was subtracted from the number of motors identified by the subject in that sequence. The obtained results were grouped by the number of simultaneously vibrating motors in a sequence (6 groups). Fig. 4.4 shows the distribution of the average for each subject in each group discriminated by the three tested strengths. No significant difference between the three tested vibration strengths within each group is observed (Fig. 4.4). The precision in perceiving the number of simultaneously active motors (*i.e.*, percentage of sequences in which the number of motors is correctly indicated) for the three different vibration strengths is presented in Table 4.1. Note, that there are no correct results achieved in the group of 6 motors. The obtained results show, that in most of the cases the users are unable to correctly recognize the number of multiple simultaneously presented stimuli, irrespectively to the stimuli strength. Nonetheless, in the cases of 1 active motor, 2 simultaneously active motors and 3 simultaneously active motors the highest success rate is observed for comfort strength of vibrations.

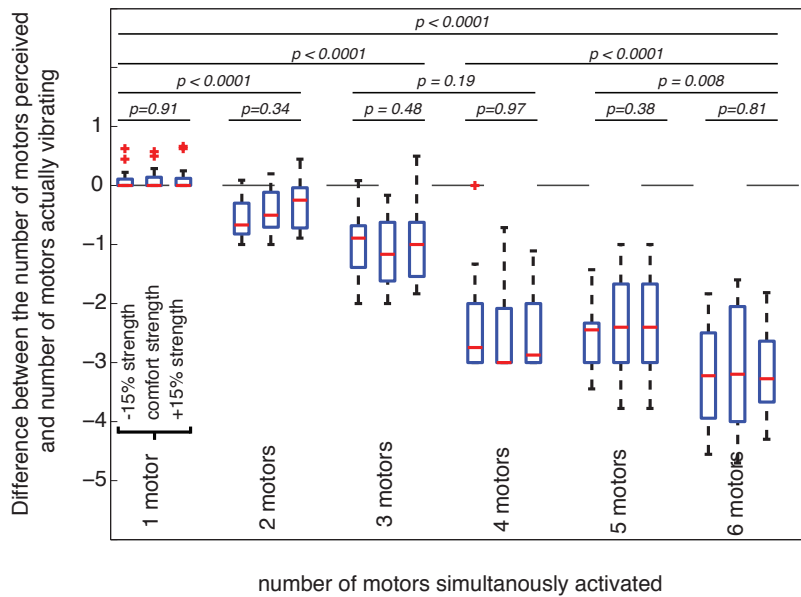


Figure 4.4: Number of actually vibrating motors subtracted from the number of motors perceived by subjects for 1-6 simultaneously active motors. For every number of simultaneously activated motors three vibration strengths were applied (mean comfort strength $\pm 15\%$). Shown is distribution of the average for each subject in each group for each strength. P-values are obtained from ANOVA tests and indicate significance of differences between and within groups.

Table 4.1: Percentage of sequences in which the number of motors is correctly indicated with respect to the number of simultaneously active motors in a sequence, for three tested strengths of vibrations.

	-15% strength	comfort strength	+15% strength
1 motor	86.21%	93.75%	86%
2 motors	19.33%	39.84%	28.21%
3 motors	19.66%	30.88%	27.27%
4 motors	13.51%	14.1%	15%
5 motors	5.13%	5.13%	5.41%
6 motors	0%	0%	0%

The third goal of this experiment was to determine the localization precision. To normalize the data for the various head sizes of the subjects, the positions of the motors and the positions of the identified vibration sources were projected onto a circle with a circumference of 12 units length. Thus, in the new scale, a unit length corresponds to the distance between two consecutive motors. The precision of motor localization is expressed as the distance between the vibration source identification point and the closest active motor of a given sequence. For further analysis, I decided to consider only the sequences where the number of identified motors equaled to the number of actually active motors. Therefore, I will discuss separately only the cases of 1, 2 and 3 simultaneously active motors because they contain a relatively high number of such sequences (Table 4.1). Moreover, due to the lack of a significant difference between the three tested vibration strengths (discussed previously) the data obtained for these strengths are taken together.

In case of only one active motor in a sequence, I calculate for each user and for each sequence the distance between the position of the motor indicated by the user and the active motor. Therefore, for each user a number of measured distances for every motor location is obtained, over which I calculated a mean distance value. I repeat such procedure for all users, storing for every user a mean distance value for every motor location. Fig. 4.5A shows the distribution of the mean distances for each user for each motor location if only a single motor is activated in a sequence. The number of subjects experiencing particular sequences vary with respect to the head locations which is an effect of the random sequence generation during the experiment. This number is explicitly given on every graph (square brackets). Subsequently, on the obtained results I perform a multi-comparison test based on the ANOVA analysis (*i.e.*, pairwise comparisons for a significant difference between the means of two motor locations at a 95% confidence level). This test resulted in three different groups of motor locations: *a*, *b* and *c*. Since the groups indicate significant differences in the means, each motor location can belong either to one or to two groups (*e.g.*, group *a* is significantly different from group *b* and from group *c* but group *ab* is significantly different only from group *c*, *etc.*). The grouping allows to define high (*a*) and low (*c*) levels of precision for the different motor locations and to derive good and bad locations for motor placement. Fig. 4.5B&C follow the same procedure for 2 and 3 simultaneously active motors. In these cases, I measured the distance from the position of a motor indicated by a user to the closest active motor in a sequence.

In all the cases, group *a* contains the locations of the highest precision with the average distance between the point indicated by a user and a vibrating motor of < 0.5 . Such distance suggests, that the motors are correctly localized on the head. The locations 2, 3, 4, 5, 8, 9, 10 and 11 were assigned to group *a*. Groups *b* and *c* represent lower

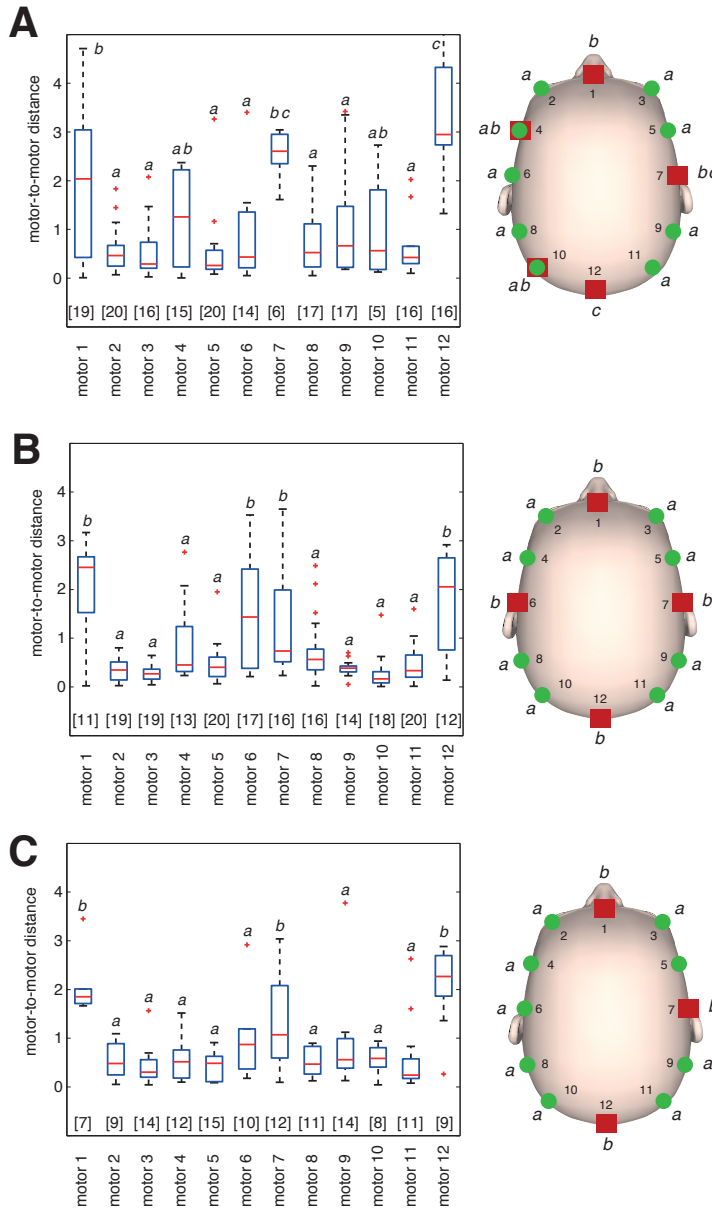


Figure 4.5: Precision in stimuli localization for each of the 12 motor locations. Shown are the results for sequences with 1 (A), 2 (B) and 3 (C) simultaneously vibrating motors. Left column: Distribution of average distances that subjects deviated from the actual active motor for each motor location. Motor locations are divided into groups based multi-comparison tests for significant differences of the mean (see text for details) where *a, b* and *c* indicate high, medium and low precision, respectively. The number of users (given in square brackets below the bars) for each motor location varied due to random sequence selection during the experiment. Right column: Top view of the head indicating the group to which each motor location belongs (*a* - green circle, *b, c* - red square). The motor location numbers used in the left column graphs are given inside the head.

precision for motor localization. The average mean distance value of group *b* is ≈ 1.5 , while for group *c* it is ≈ 3 . Locations 1, 7, and 12 are always assigned to groups *b* or group *c*. The remaining location 6 belonged either to group *a* or to group *b*. The average mean distance value for this location is ≈ 0.9 . The motor locations assigned to the groups are marked on the graphs as well as on the top view of the heads in Fig. 4.5.

4.4 Discussion

My experimental results can be used to extract guidelines for the design and control of a head-attached vibrotactile display. First, an actuator needs to be selected guaranteeing operational properties such as size, weight, power consumption and character of the output vibration (*i.e.*, the frequency, amplitude and motion character of the vibrating tip). I showed the usefulness of the coin-type motor in a wearable scenario, where low power consumption and small size are the priorities, outperforming for this purpose the C-2 tactor (Engineering Acoustics Inc.) used by Myles and Kalb [107] and the TP4x6 solenoid proposed by Gilliland and Schlegel [102]. In particular, small size and low power consumption allow battery supply and control unit miniaturization, essential for portable applications. Unfortunately, due to its operational principle, the coin-type motor does not support independent control over the vibration amplitude and frequency. This limitation can be compensated by arranging the vibrations into temporal patterns (sequences) as shown in my study and suggested by Morley and Rowe [113]. Alternatively, recently a method of decoupling the control over the amplitude and the frequency has been proposed [92]. This method is based on creating *vibels* - stacks of vibrating motors, whose individual control allows modulation of the envelope signal to the desired profile.

Depending on the chosen actuator, information can be transferred using the vibration amplitude, frequency or amplitude-frequency pair (strength). For a given actuator type a test determining minimum vibration strength and comfort vibration strength should be performed. This is important because, as presented in the studies, the differences between the forehead and the back head and the hysteresis, observed for the minimum vibration strength, disappear at the comfort vibration strength. The fact that the comfort vibration strength is insensitive to head location and hysteresis extends the results presented by Myles and Kalb [107] who focused only on minimal vibration strength perception. Operating at comfort strength guarantees that vibrations can be successfully perceived by every subject. Therefore, comfort vibration strength can act as a default strength value of a vibrotactile display. Moreover, I demonstrated that the deviation from the comfort vibration strength of $\pm 15\%$ has no significant impact on motor number recognition, which confirms its robustness. I identified

Chapter 4. Vibrotactile Feedback System - Design and Control

the comfort vibration strength value of the coin-type motor operating based on the unbalanced mass principle to be 70.84 mJ/cm^2 . I believe that this value can be applied to other types of vibration actuators operating based on the same principle.

The next step is to determine the number of actuators in the vibrotactile display. I support the observation of Jones and Sarter [106] that an increase in actuator density does not necessarily correspond to an increase in information transfer. This is due to the fact, that only a limited number of simultaneous stimuli can be successfully perceived. My results revealed low performance for multi-point discrimination showing a drop in success rate of nearly 54% when increasing from one to two simultaneously presented stimuli. Furthermore, a constant undershoot trend in the number of perceived motors with respect to actually vibrating motors is observed if more than one motor is simultaneously active. This suggests that motor vibrations propagate on the head masking other simultaneously presented stimuli [114–116]. Therefore, I strongly suggest to limit the number of actuators in the display to the minimum required by a given application. Moreover, global coordination of the motors must be applied to limit the number of simultaneously active units.

Next, the actuators' positions on the head should be determined. I investigated location precision for single- and multi-point vibration to determine the best out of the 12 tested ones. I observed, that when increasing from one to three simultaneously presented stimuli the general sensitivity pattern remains fairly constant, as presented in Fig. 4.5. This shows that the identified sensitivity pattern holds irrespective of the number of presented stimuli. Therefore I suggest to explore the eight best locations (motors: 2, 3, 4, 5, 8, 9, 10 and 11) while to avoid the three worst ones (motors: 1, 7 and 12) and motor 6, for which precision lies in-between.

Finally, the overall ergonomics of the system should be addressed. This is particularly valid in case of users presenting movement or vision deficiency, whose ability to put on, adjust, clean and operate the device is limited. Therefore, significant effort should be put on the wearability, reliability and intuitive operation of the system. I believe, that head-attached vibrotactile displays can successfully fulfill such requirements, outperforming other body locations such as torso, belt, hands or tongue.

4.5 Conclusions

The presented in this chapter quantification of the information transfer for a head attached vibrotactile display allowed me to identify three major design factors and to suggest design and control principles for them. First, a comfort strength of tactile stimulation should be estimated. This comfort strength should be preferred over the minimally perceivable strength due to its insensitivity to hysteresis effects and variation in strength perception in different regions of the head. Second, the results on multi-point stimulation, ranging from one up to six simultaneously active motors, strongly suggest to avoid using multiple motors at the same time because the precision in perceiving the correct number of active motors is dramatically decreased compared to a single active motor. Last, in contrast to motor number estimation, the precision of localizing the stimulus remains surprisingly constant over the whole range of multi-point stimulation showing, however, great differences between different regions of the head. Such differences need to be considered for placing the motors in a head attached vibrotactile display if high localization precision is required.

I believe that the thorough analysis of the information transfer via a head attached vibrotactile display may prove useful in various applications that aim at extending a user's perceptual space, not only as the development of assistive devices for visually impaired persons but also as a gait rehabilitation tools or a virtual reality devices.

5 *VisionHat* - System Integration and Tests

In this chapter, I present the design of the *VisionHat*: the ETA system supporting users in indoor and outdoor navigation by increasing their awareness of motion present in close proximity. Based on perceived motion, collision-threats are estimated. Subsequently, the system transfers this information to a user through the head-attached vibrotactile system. The *VisionHat* possesses modular structure that allows for scalability and wide surface coverage. All the elements are integrated into a hat to provide them with wearability and comfort during long-time use. Moreover, in this chapter I present experiments proving operation of the system in indoor and outdoor environments. In particular, the system is tested in a natural outdoor scene and in an office-like room, where the present motion is successfully detected and an appropriate feedback signal is triggered.

5.1 Introduction

In the introduction to this thesis I, following Kaczmarek et al. [5], pointed out two equally important challenges that must be addressed in an ETA system design: the wearability and the information transfer. Throughout the thesis, these two challenges were, so far, addressed individually.

In Chapter 2, the Vision Tape was introduced. Due to its flexibility, the VT can be integrated with textiles and used as a wearable OF sensor. Already in Chapter 2 basic tests with textile integration were described, showing the mechanical compliance of the developed prototype devices. In Chapter 3, I described the shape sensors, the necessary elements providing the VT with self-shape estimation for OF normalization. In Chapter 4, the head-attached vibrotactile feedback system, capable of transferring information to a user in an intuitively-understandable manner, was investigated. The described human experiments determined the placement of the vibration motors on the head and the principles for their control.

In this chapter, the two challenges are, for the first time, addressed together in a single wearable ETA system: the *VisionHat*. The main function of the *VisionHat* is to increase the general awareness of the motion present in close proximity to a user. In particular, the *VisionHat* extracts information regarding collision threats present in the surrounding environment during everyday activities. To extract the threats, the OF obtained with the VT and normalized with the information from the shape sensor is used. Subsequently, the hat-integrated vibrotactile display transfers the information. It is important to understand that the *VisionHat* aims at supporting, not replacing, the conventional systems used by visually impaired persons, such as the white cane or the guide dog.

In this chapter, I present the design of the *VisionHat* and the accompanying signal processing for estimation of collision-threats. The proposed modular design facilitates clothing integration and supports expansion towards large surfaces due to the possibility of rearranging the modules on the surface. The function and the design of the three building modules – the *Tape*, the *Nerve* and the *Brain* – are described. Also, the data flow scheme is presented. Finally, I assess the performance of the *VisionHat* when worn in indoor and outdoor environments, mimicking everyday situations. The conducted experiments demonstrate good wearability and quick information transfer.

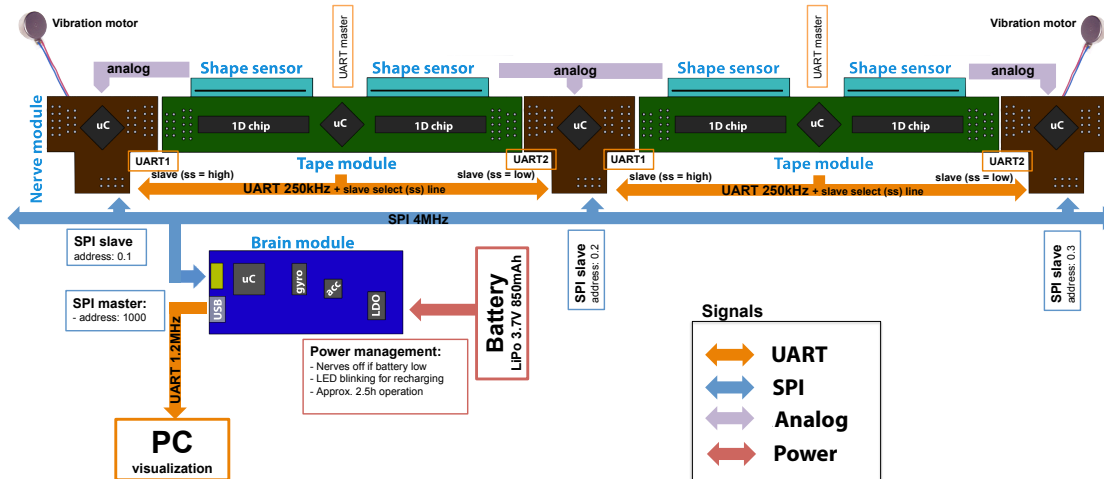


Figure 5.1: Modular design of the *VisionHat* system and the data flow. The system consists of two *Tape* modules equipped with two shape sensors each, three *Nerve* modules and one *Brain* module. Moreover, two vibration motors and a battery are required for correct operation of the system, *i.e.*, power supply and feedback signal transfer. UART and SPI busses are used for information exchange between the modules. Power, provided by the battery is managed and distributed through the *Brain* module to other modules of the system.

5.2 System Design and Data Flow

The modular design of the *VisionHat* ETA system and the signal flow are shown in Fig. 5.1. The system consists of two *Tape* modules, three *Nerve* modules and one *Brain* module. Also, two vibration motors, left and right (corresponding to, respectively, motor positions 2 and 3 in Fig. 4.2, Chapter 4.2), and a battery are required for complete operation of the system.

The configuration pursued here provides a frontal FOV of approximately 90°, equally shared between the left and the right *Tape* module (Fig. 5.2). However, it should be mentioned that due to the flexibility of the substrate, deformations during wearing occur, and hence, the FOV varies and depends on the current geometrical configuration of the system imposed by the underlying textile substrate. Nevertheless, placing the device on the head constrains the possible deformations and simplifies the challenge of shape monitoring.

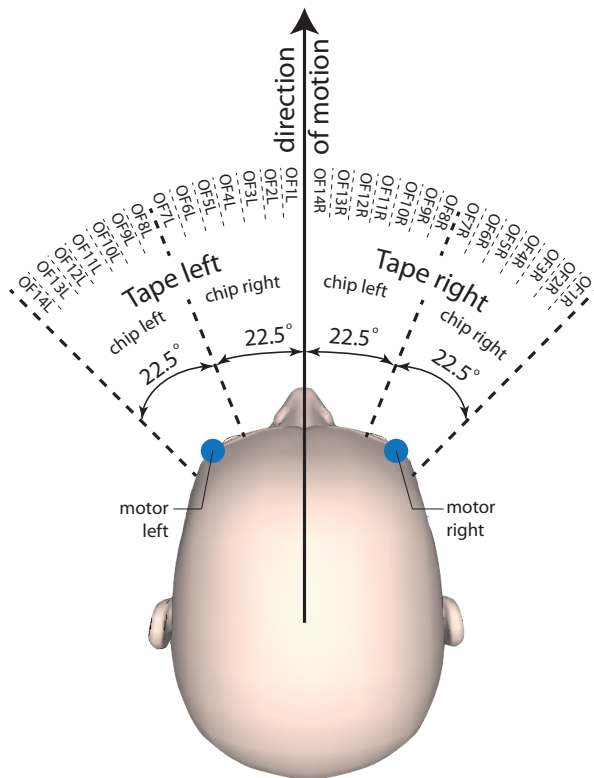


Figure 5.2: Estimated angular perceptive range (the overall field of view) of the *VisionHat* illustrated with respect to human head. In particular, there are indicated angular fields of view of the left and the right *Tape* modules, which include the left and right vision chip for each module, and the distribution of the OF vectors. Also, positions of two vibration motors (left and right) are marked. It should be remembered that the perceptive range of the system varies due to the flexibility and depends on the geometrical configuration of the textile substrate.

5.2.1 Tape, Nerve and Brain Modules

The *Tape* module is responsible for image acquisition and its subsequent processing for motion extraction. The module, presented in Fig. 5.3, consists of the second VT prototype (see Chapter 2.2.3) and the back-side attached hyper-flexible strain gauge (see Chapter 3.2.3). The aim of the module is to extract OF: the pattern of apparent motion of objects in the visual scene caused by the relative motion between an observer and the scene. The OF is calculated onboard the VT microcontroller based on two consecutive images. A simplified version [39] of the I2A [40] algorithm is used (see Chapter 2.2 equation 2.2).

There are 14 OF vectors (OF1-OF14) calculated within the FOV of a single *Tape* module, each one across five consecutive ommatidia (respectively, OF1-OF7: ommatidia chip right 1-5, 6-10, 11-15, 16-20, 21-25, 26-30 and 30-34, OF8-OF14: ommatidia chip left 1-5, 6-10, 11-15, 16-20, 21-25, 26-30 and 30-34), as shown in Fig. 5.2. A second order Finite Impulse Response (FIR) low-pass filter with a cut-off frequency of 100 Hz is applied to every OF vector individually to reduce the high-frequency noise.

The images are acquired with a fixed frame rate of 40 fps. Such a frame rate is chosen as a tradeoff between the quality of the measured OF and the maximum perceivable

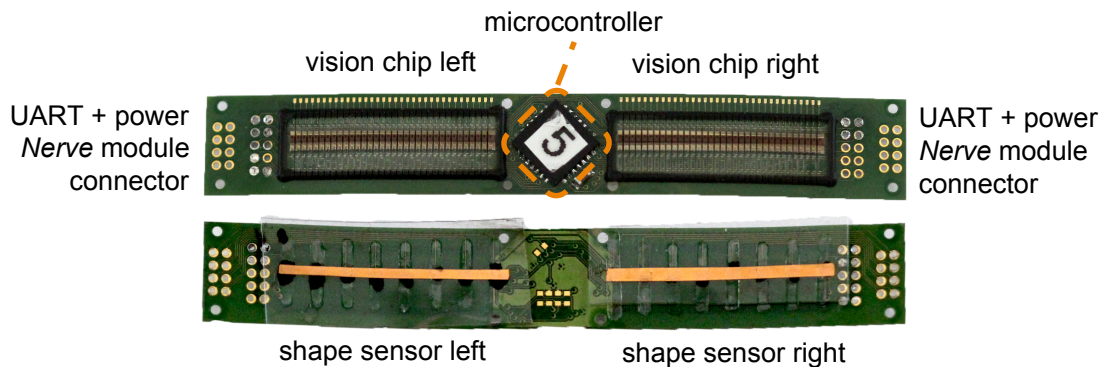


Figure 5.3: *Tape* module consisting of a VT and two shape sensors attached to the back-side of the flexible substrate. Two connectors, placed on both ends of the module, provide UART communication and power supply.

velocity of the relative motion. The lower the frame rate, the higher the corresponding pixel shift between two consecutive frames, and consequently, the amplitude of the OF. Under an unchanged noise level, an increase in the OF amplitude improves the signal-to-noise ratio. However, a low frame rate reduces the maximum perceivable velocity, as OF under pixel shift exceeding one pixel in two consecutive frames cannot be correctly extracted with the simple I2A method. Although alternative OF algorithms could address this challenge, they are typically more computationally demanding and require images of much higher resolution. Moreover, the 40 fps frame rate is selected based on the assumption that the user travels with an average walking speed of 1.5 m/s. It has been measured that pedestrians walk with an average speed of 1.2 m/s for older and 1.5 m/s for younger people [117]. Average walking speed below the mentioned 1.2 m/s was observed in visually impaired people not accompanied by assistance [118]. Also, I assume the presence of moving objects and dynamic sources of collisions (for instance, other people) in the social space [119], *i.e.*, approximately 1.5 m from the user.

The shape of the module is measured with two shape sensors – the hyper-flexible strain gauges – one underneath every vision chip. The connection pads of the strain gauges are designed to match the spatial distribution of the OF vectors. Therefore, the shape perceived by every strain gauge segment can be directly used for normalization of the corresponding OF vector following the procedure described in Chapter 2.3.1.

The *Tape* module performs one-directional communication to two neighboring *Nerve* modules based on the UART protocol under the bandwidth of 250 kHz. In every

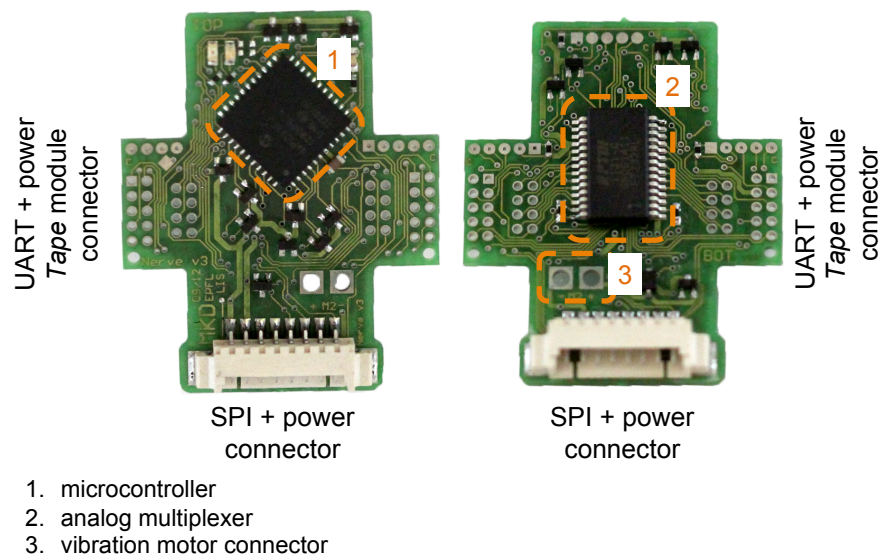


Figure 5.4: *Nerve* module consisting of a top-side-placed microcontroller, back-side-placed analog multiplexer, two connections providing SPI communication and power supply, two connections providing UART communication and power supply to the attached *Tape* modules and a PWM driven vibration motor connector.

communication cycle, 14 values of the OF vectors are sent. Data markers are used for data synchronization.

The module, as well as the whole system, operates under 3.3 V DC. The mean current consumption of the module, measured during 1 min. of continuous operation, is 70 mA. The weight of the module is 0.9 g, out of which 0.7 g is the weight of the VT while the remaining 0.2 g is the weight of the two shape sensors.

The *Nerve* module, presented in Fig. 5.4, interconnects the *Brain* module and the *Tape* modules. It emerged as a solution to the limited processing power and Input/Output (IO) capabilities of the *Tape* module. The main function of the *Nerve* module is the read-out of the neighboring hyper-flexible strain gauges, following the scheme described in Chapter 3.2.3. The read-out is performed periodically (frequency of 50 Hz) and simultaneously for two neighboring shape sensors using a dual-channel analog multiplexer (ADG707BRUZ, ANALOG DEVICES), a reference 150 Ω resistor and a microcontroller-integrated ADC converter (dsPIC33FJ128GP804, Microchip). The OF values received from two adjoined *Tape* modules are subsequently normalized with the measured shape.

Chapter 5. *VisionHat* - System Integration and Tests

Another function of the module is activation of the vibration motors. Motor strength is fixed to 70.84 mJ/cm^2 . The strength is obtained by PWM modulation of the supply voltage. Every active motor is automatically switched off 0.5 s after the last activation signal. As shown in Chapter 4, a 0.5 s long feedback is a minimum sufficient for correct information transfer. Moreover, following the results presented in Chapter 4, the number of simultaneously vibrating motors is limited to one. To prevent simultaneous activation of multiple motors, the activation is commanded by the *Brain* module, which provides a global overview on the system.

A bi-directional SPI bus (bandwidth of 4 MHz) is used to communicate with the *Brain* module, based on an individual, unique addresses assigned to each module. When the address is called by the *Brain* module the corresponding *Nerve* module replies by sending the normalized OF values and awaiting the motor activation command.

The weight of the *Nerve* module is 2.1 g and the attached vibration motor is 0.7 g. The current consumed by the module is approximately 130 mA with, and 80 mA without, the vibration motor active.

The *Brain* module (Fig. 5.5) is a single module responsible for the global coordination of the *VisionHat* system and the feedback activation decision. The on-board microcontroller (dsPIC33FJ128GP802, Microchip) collects the normalized OF values from the active *Nerve* modules (through the SPI bus) and 6 DOF inertial information from the integrated Inertial Measurement Unit (IMU). The IMU consists of an accelerometer (MMA7745 FREESCALE SEMICONDUCTOR) and a gyroscope (ITG3200 INVENSENSE); both read-out through the 1.2 MHz I²C bus.

The inertial information is necessary for correct interpretation of the OF values, *i.e.*, differentiating between the rotational and the translational component of the OF. Since the rotational component of the OF does not contain collision-related information, it should be removed from the signal. It is commonly practiced in OF-based collision avoidance systems to de-rotate OF based on the IMU information [11, 120–122] prior to further data processing. The *Brain* operates based on another, simpler strategy. When the detected rotation exceeds $30^\circ/\text{s}$ (value found empirically), the received OF vectors are ignored. Such a strategy of replacing the typical OF de-rotation is possible, because during walking, the human head is naturally stabilized [123] and the applied rotation is very limited. Continuously looking forward when walking can be intuitively explained by the fact that most of the collisions lie on our direction of walking. In healthy people, pitch and yaw rotations exceeding $30^\circ/\text{s}$ occur only when turning the head intentionally towards objects spotted in the peripheral vision, whereas roll rotations of such magnitude are almost never observed.

5.2. System Design and Data Flow

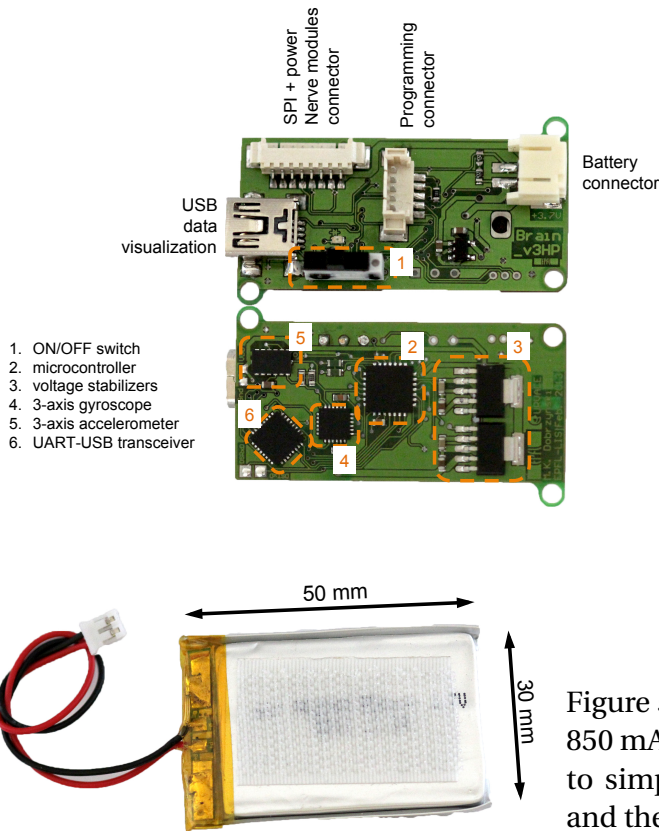


Figure 5.5: *Brain* module consisting of a top-side-placed USB port allowing connection to a PC and data visualization, a connector providing SPI communication and power supply to other modules of the system, a programming connector, a battery connector, an ON/OFF switch to start/stop the system, a back-side-placed microcontroller, two voltage stabilizers that allow decoupling the analog from the digital power supply, a 3-axis gyroscope, a 3-axis accelerometer and a UART-to-USB transceiver.

Figure 5.6: One-cell lithium-ion battery of 850 mAh capacity. The velcro tape is used to simplify attachment to the *VisionHat* and the battery replacement process.

Another function of the *Brain* module is power management. There are two voltage stabilizers providing 3.3 V DC to the analog and digital circuits of the system separately. The stabilizers are controlled by the microcontroller and can be switched on/off in respond to certain system behaviors. In particular, control over the power supply allows for a general reset of the system, performed if the communication between the *Brain* module and *Nerve* modules is lost. Moreover, since the *VisionHat* system is designed to be powered by a single-cell lithium-polymer (li-po) battery (3.7 V, >850 mAh, Fig. 5.6), whose unsupervised depletion can lead to an explosion, the *Brain* module monitors battery level and reduces power consumption in case of a low battery state by switching off the remaining modules. In such cases, the low battery status is indicated visually by blinking a red LED. In case of battery depletion reaching a dangerous level, the system is designed to shutdown automatically.

The *Brain* module supports communication to a PC through a USB port via the integrated UART-to-USB transceiver (FTDI232R, FTDIchip). Such communication, compatible with the USB 1.0 and USB 2.0 standards, may be used for data acquisition and monitoring. The data are sent to a PC on demand, based on a set of pre-defined

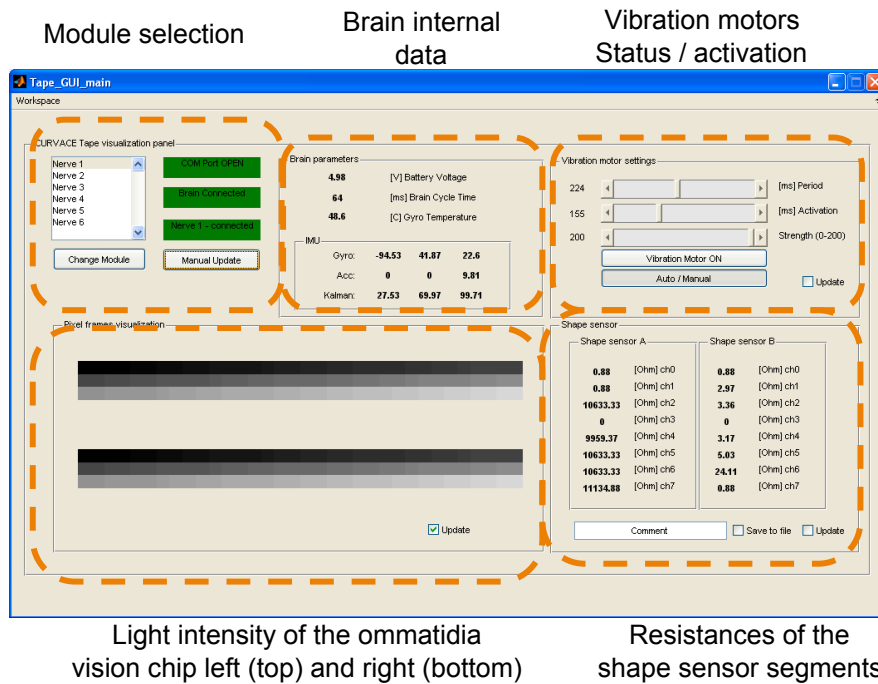


Figure 5.7: Matlab-based GUI that allows monitoring the following system data: battery level, temperature of the *Brain* module, IMU data, resistances of a given shape sensor segment, intensities of the ommatidia and status of vibration motors.

commands. To access data not stored by the *Brain* module, for instance intensity values of the ommatidia, resistances of shape sensor segments or status of the vibration motors, an appropriate command is broadcasted to all *Nerve* and *Tape* modules active in the system, who reply by sending the requested data. Because the command needs to propagate from a PC to the modules of the system and because of the communication overhead for the transfer of additional data (64 bits in case of motor activation command, 960 bits in case of shape-related information, 3264 bits in case of pixel intensity values), a delay beyond 1.5 s is observed, which excludes the possibility of real-time data monitoring. Nevertheless, such a scheme provides a view of the current status of the system, useful during system development and characterization stages. To further facilitate data monitoring, I developed a GUI using Matlab (Fig. 5.7). The GUI allows checking for modules active in the system and collecting, displaying and logging information regarding battery level, temperature of the *Brain* module, IMU data, resistances of a given shape sensor segment and pixel values. Moreover, the GUI provides the status and manual control over the vibration motors, their strength and activation time.

Current consumption by the module is approximately 80 mA, measured during one minute continuous operation. The total weight of the module is 21.3 g, out of which 17.4 g is the weight of the battery.

Supporting components. In addition to the three modules, the motors and the battery, there are three copper cables used to distribute power and provide SPI communication. Every cable consists of eight wires. Due to the relatively large diameter of the wire (0.32 mm), the resistance of the connection is $<0.3 \Omega$, which allows reaching a SPI communication bandwidth of 4 MHz. The weight of one cable is 2.4 g.

Moreover, two OpenLog modules (<https://github.com/sparkfun/OpenLog>) were added during the time of the experiments for real-time data collection. OpenLog is a serial logger that automatically writes the received data (UART protocol under maximum bandwidth of 115200 bps) to a micro SD card. The logger is electrically compatible with the *VisionHat*, operates under 3.3 V and consumes 100 mA of current during data logging. The weight of the logger is 1.2 g while the weight of the micro SD memory card is 0.2 g.

The weight and current consumption of the components as well as the whole *VisionHat* system is summarized in Table 5.1.

5.2.2 Hat Integration

A critical aspect of designing a wearable ETA system, derived by Mau et al. [6] from a series of interviews and ethnographic studies at the Blind and Visual Rehabilitation Service of Pittsburgh, is the visual appearance of the assistive device during its utilization. Mau reports that "there is a psychological barrier and a stigma associated with assistive devices, even canes". Therefore, the desired assistive system should be unnoticeable to an external observer.

To address this challenge, I decided to integrate all the modules of the *VisionHat* system into an ordinary baseball cap, the hat, by sewing them to the inner part of the cap, as shown in Fig. 5.8. Two rectangular openings are cut in the front to provide vision to the vision chips of the two *Tape* modules. The vision chips are the only visible elements of the system hidden in the concavity of the cap. The two vibration motors are sewn and internally protected using a layer of textile to provide separation between the metal case and the skin of the user. The battery is also hidden. Velcro tape is used to support quick battery replacement.

Chapter 5. *VisionHat* - System Integration and Tests

	Weight [g]	Current [mA]	Units in the system []
Tape module		70	2
- Vision Tape:	0.7	-	2
- shape sensor:	0.2	-	4
Nerve module			3
- the module:	2.1	80	3
- vibration motor	0.7	50	2
Brain module			1
- the module:	3.9	80	1
- battery (3.7 V 850 mAh):	17.4	-	1
Supporting components			-
- cable:	2.4	-	3
- OpenLog:	1.2	100	2 (optional)
- SD card:	0.2	(included in OpenLog)	2 (optional)
<hr/>			
<i>VisionHat</i> system:			
- with OpenLog:	40.8	710 (with vibration motor) 660 (without vibration motor)	
- without OpenLog:	38	510 (with vibration motor) 460 (without vibration motor)	

Table 5.1: Summary of the weight, current consumption and number of units of the *VisionHat* system components.

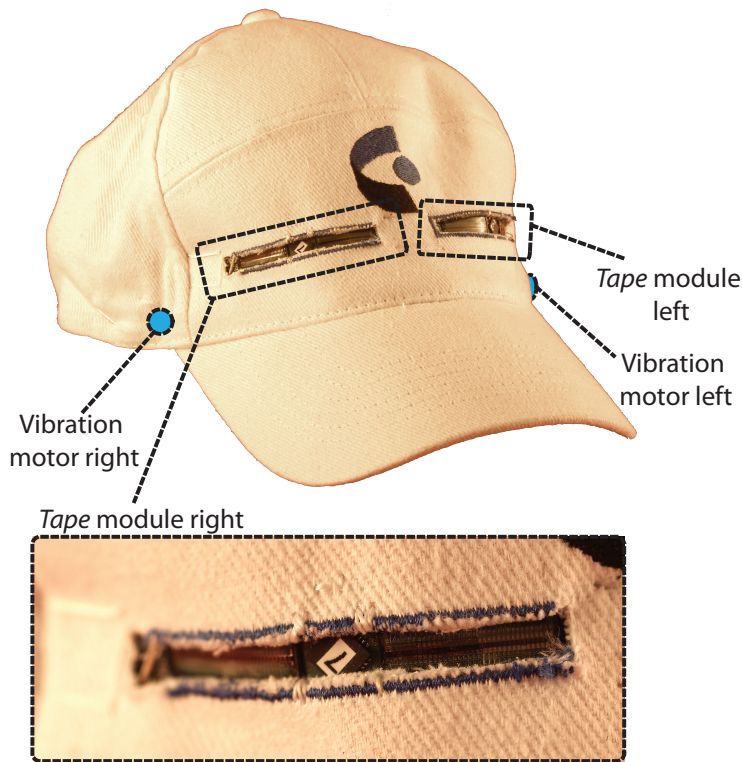


Figure 5.8: Baseball cap with integrated *Tape*, *Nerve* and *Brain* modules and the supporting components. The cap is chosen and designed to minimize the visibility of the integrated devices.

To further assess the visual appearance of the *VisionHat*, caps of four different colors, gray, black, red and white, were manufactured, as shown in Fig. 5.9. Although the prototype of the system is integrated into a white cap, I admit that the components are best hidden with the black version. Moreover, dirt embedded during manipulation of the white prototype could most likely remain unnoticeable if the black cap was used.

5.2.3 Information Processing and Feedback Activation

The amplitude of the translational components of the OF (p) is proportional not only to the ratio of the relative speed (T) between the object and the observer and the distance (d) between them, but also depends on the relative angular orientation (α) of the OF sensor with respect to the moving object (5.1). Therefore, under a translational motion in a static environment, amplitudes of the 28 OF vectors extracted with the two *Tape* modules should follow a sinusoidal distribution, where amplitudes equal to zero indicate the direction of motion. The sensors oriented at an angle of 45° to the direction of motion will show the maximum amplitude. This principle of motion



Figure 5.9: Baseball cap in four colors: gray, black, red and white.

direction detection from a sinusoidal distribution of the OF vectors has already been proposed in robotics [124, 125] for odometry and egomotion estimation:

$$p \cong \frac{|\mathbf{T}|}{D(\alpha)} \cdot \sin(\alpha), \quad (5.1)$$

In the *VisionHat* system, knowledge regarding the distribution of the OF amplitudes along the FOV is used to derive the vibration motor activation thresholds individually for every OF vector. The proposed activation thresholds have a sinusoidal distribution with zero corresponding to the vectors pointing in the direction of motion and maximum values corresponding to those pointing to the side. To activate vibration motors, the absolute value of the OF, and hence, the absolute value of the thresholds are used, as presented in Fig. 5.10 (top). By taking the absolute values, I eliminate any dependence on the direction of motion, which is unwanted for collision avoidance.

The vibration motor is activated if at least one of the OF vectors crosses the threshold. If the threshold is crossed by the OF perceived on both sides of the hat simultaneously, the vector with the highest amplitude activates the corresponding vibration motor.

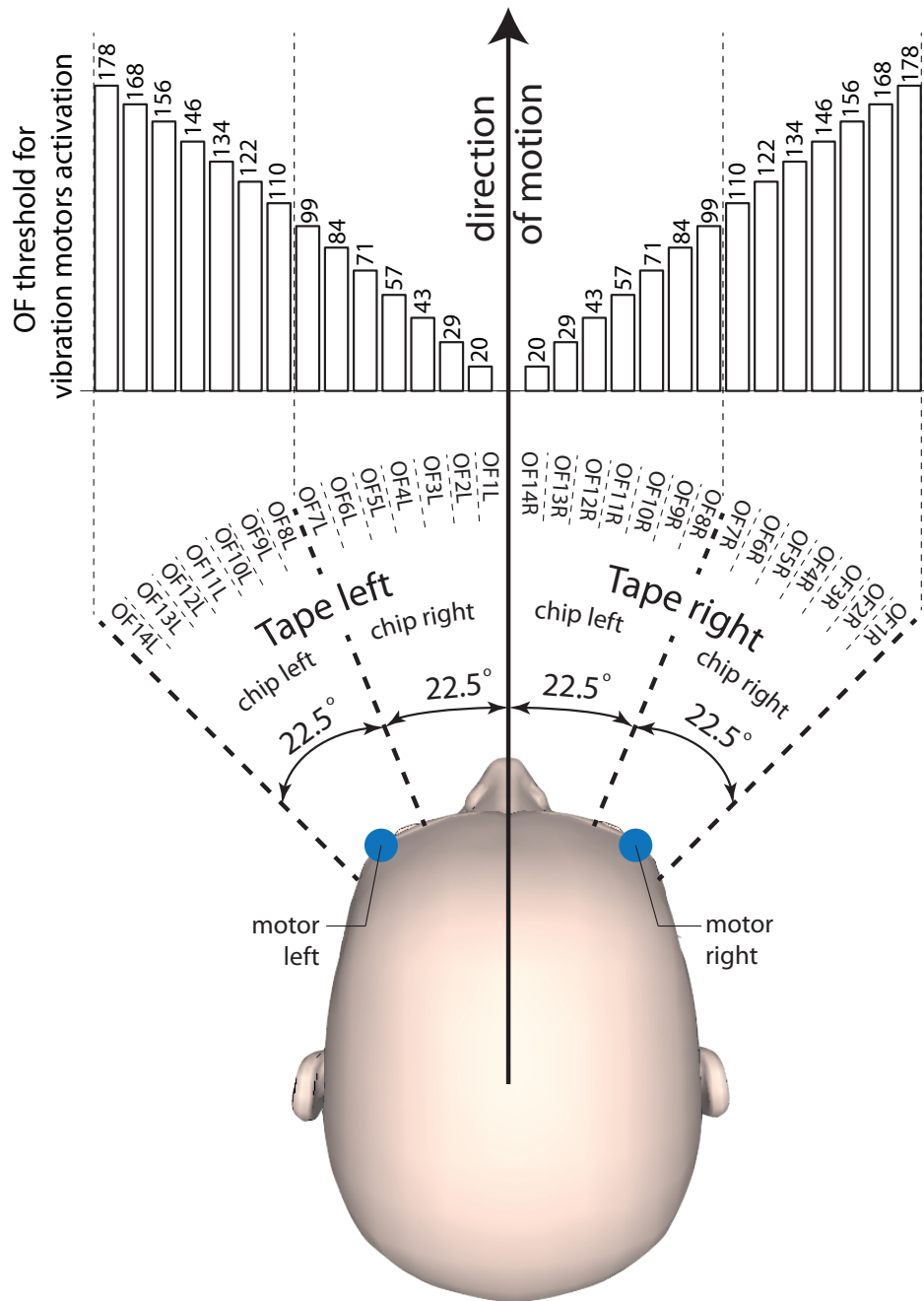


Figure 5.10: Distribution of the vibration motor activation thresholds for the 28 OF vectors of the *VisionHat* system

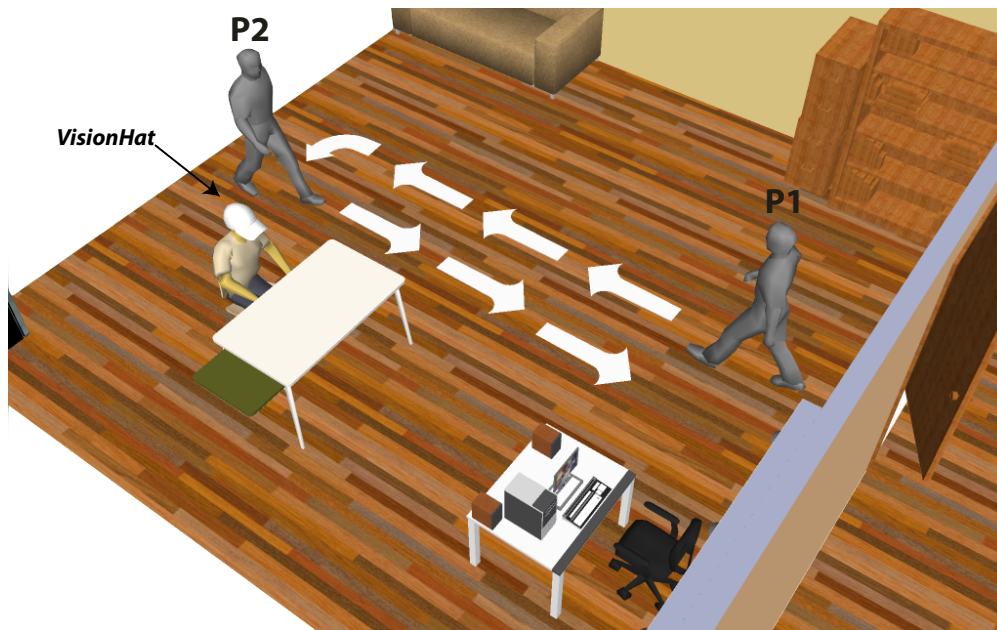


Figure 5.11: Experiment 1: sitting in an office. The person sitting by a desk is equipped with the *VisionHat* prototype. Two phases of the experiment, P1 and P2, correspond to activities of another person walking. P1: entering the room through the door, passing by the sitting man, P2: turning back, passing by the sitting man and going out through the door. Light is provided through ceiling-attached incandescent lamps with an average illuminance of 350 lux.

5.3 Experiments

To demonstrate performance of the device, two experiments are conducted exploring indoor and outdoor operation of the system.

5.3.1 Experiment 1: Sitting in an Office

The aim of the first experiment is to demonstrate that the *VisionHat* prototype can support a user in an office-like environment. In particular, the goal is to demonstrate that in such an environment OF can be successfully perceived and normalized based on the shape information obtained with the hyper-flexible strain gauges. Moreover, that based on the perceived OF, the vibration feedback is activated, signaling approaching and passing objects.

The experimental setup is shown in Fig. 5.11. There is a person wearing the *VisionHat* prototype sitting on a chair in a 7 m long by 4 m wide room. Light is provided through

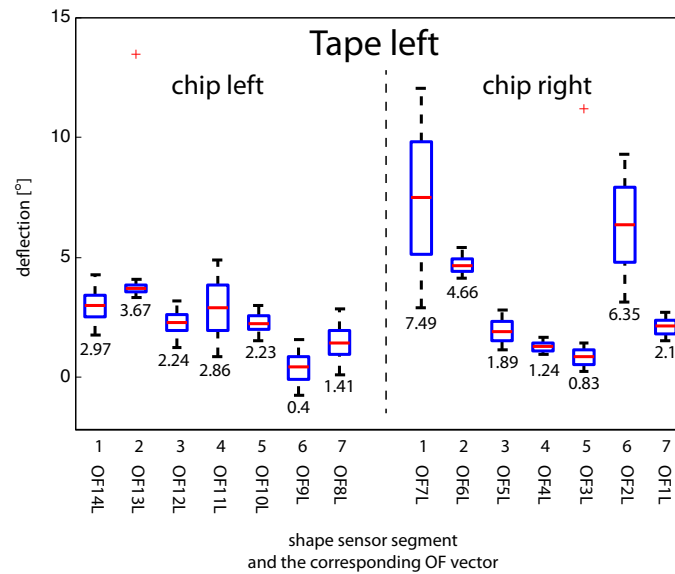


Figure 5.12: Shape of the right and the left vision chip of the left *Tape* module during the experiment. Boxplots show the median (value written below the boxplots) and the lower and upper quartiles of the angular deflections of the seven segments of the two shape sensors placed underneath the right and the left vision chip. The shape values directly correspond to the angular FOV of the 14 segments of the two vision chips over which the OF vectors were calculated.

ceiling-attached incandescent lamps with an average illuminance of 350 lux, as measured on the floor level. There are two chairs, two desks and a PC in the room. The experiment consists of two phases, which correspond to the activities of the walking person. Phase P1: the person is entering the room through the door and is passing by the sitting person. Phase P2: the person is turning back, passing by the sitting person and going out through the door. The speed of walking is approximately 1.5 m/s. The closest distance between the two persons is approximately 0.5 m.

The overall time of the experiment was 11 s. Data regarding OF, shape and motor activities are registered with an OpenLog module at a frequency of approximately 40 fps. There were 450 data frames registered during the experiment, out of which 240 clearly illustrating the two phases of the experiment are selected for the analysis presented here. Also, due to the nature of the experiment, the meaningful data come from the left *Tape* module, and therefore, these data are presented here only.

The boxplots (Fig. 5.12) representing the median and the lower and upper quartiles of the angular deflections of the seven segments of the shape sensor placed underneath the right and the seven segments of the shape sensor placed underneath the left

Chapter 5. *VisionHat* - System Integration and Tests

vision chip of the *Tape* module, registered during the experiment. The OF vectors, OF1L-OF14L, were continuously normalized throughout the experiment according to the shapes of the segments following procedure the described in Chapter 2.3.1.

Normalized amplitudes of the the 14 OF vectors of the right and the left vision chip are shown in Fig. 5.13 (top) as a function of the frame index. It can be observed that the two phases of the experiment are clearly visible in the obtained data. The first peak of the OF amplitude corresponds to the moment of the person passing by during the P1 phase, while the second peak of the OF amplitude, registered approximately 120 frames (3 s) after the first one, corresponds to the moment of the person going back during the P2 phase. There are also the 14 corresponding thresholds marked on the same figure. The moment of threshold crossing by the amplitude of every OF vector is indicated on the 14 bottom graphs with a bar.

Although in this experiment the first motor activation (frame index 5) occurred due to the OF2L vector, it should be classified as a false positive due to the fact that at the time of the activation the moving object could not have been present in the FOV of the sensor. The second motor activation (frame index 68) was also triggered by the vector OF2L and happened due to the beginning of the P1 phase. The subsequent threshold crossings that occurred during the P1 phase followed the sequence: simultaneously OF3L and OF5L, OF4L, OF9L, OF11L and OF12L. Although the amplitudes of the other vectors did not reach the corresponding thresholds, the propagation of the object along the FOV of the sensor is clearly visible.

During the P2 phase, the motor was activated due to the OF14L vector. Threshold crossings occurred in the following sequence: OF14L, OF11L, OF3L and OF2L. Again, the propagation of the object in the FOV of the sensor can be observed in the sequence.

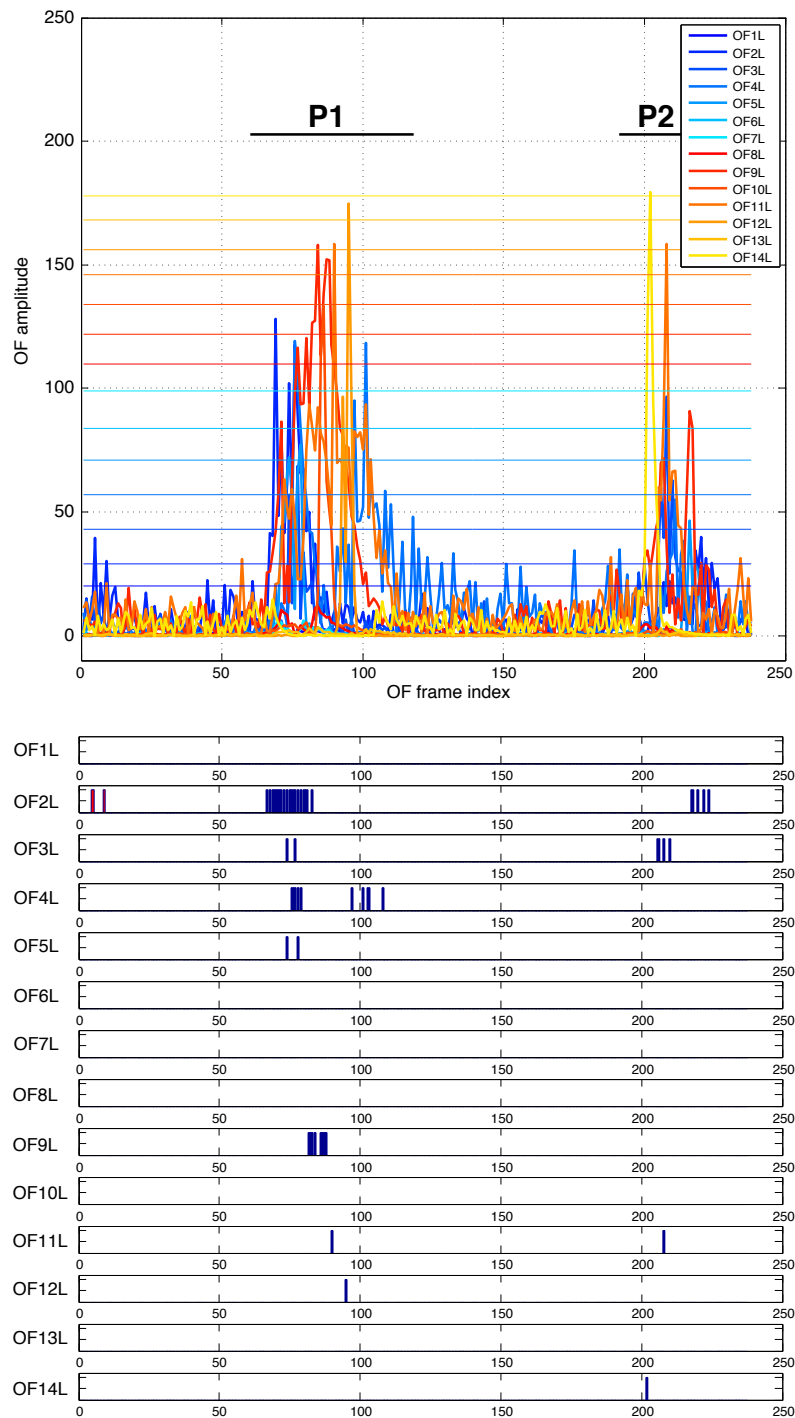


Figure 5.13: OF as a function of frame index collected during the first experiment. Top: normalized amplitudes of the 14 OF values of the right *Tape* module. The threshold levels for every OF are indicated and correspond to those presented in Fig. 5.10. Bottom: the frame indexes of OF threshold crossings are indicated for each vector individually. Two phases of the experiment, P1 and P2, are marked.



Figure 5.14: Experiment 2: outdoor walking during a cloudy day. The aim of the experiment is to show the performance of the *VisionHat* system during outdoor operation. The user, typically equipped with a white cane as well as the *VisionHat*, is walking with an average speed of approximately 1 m/s. An approaching person is passing by with a speed of approximately 1.5 m/s at a distance of approximately 0.5 m. The experiment is conducted under cloudy-day light conditions with an average illuminance of 850 lux, as measured on the ground level.

5.3.2 Experiment 2: Outdoor Walking During a Cloudy Day

The aim of the second experiment is to demonstrate that the *VisionHat* prototype can support a user in such an everyday activity as outdoor walking. In particular, the goal is to demonstrate that the system provides information regarding objects moving in close proximity to the user, which may be sources of collisions.

The experiment is illustrated in Fig. 5.14. During the experiment, a healthy user walking with an average speed of approximately 1 m/s is wearing the *VisionHat* prototype. The user does not use the white cane, as shown in the figure. During the approximately 10 s long experiment, a single event, P1, occurs. An approaching person is passing by with a speed of approximately 1.5 m/s at a distance of approximately 0.5 m.

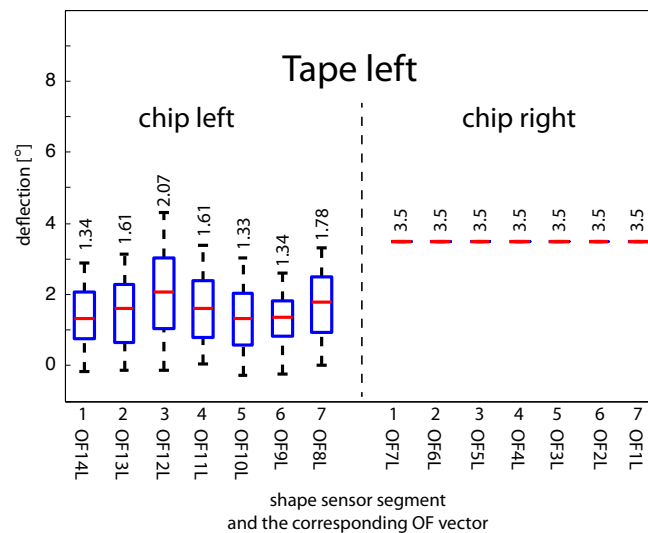


Figure 5.15: Shape of the right and the left vision chip of the right *Tape* module during the experiment. Boxplots show the median (value written above the boxplots) and the lower and upper quartiles of the angular deflections of the seven segments of the two shape sensors placed underneath the right vision chip, registered during the experiment. Values of the shape sensor placed underneath the left vision chip were fixed to 3.5° due to a malfunction of the sensor.

The experiment is conducted during cloudy-day light conditions with an average illuminance of 820 lux, as measured on the ground level. Similarly to the first experiment, amplitudes of the OF vectors and the shape data were registered by an OpenLog module at the frequency of approximately 40 fps. Due to the nature of the experiment, the meaningful data come from the right *Tape* module, and therefore, these data are presented here only. Moreover, although the module is equipped with two shape sensors, the shape-related information was successfully obtained from only one of them. The gold patterned conductor of the second shape sensor, placed underneath the left vision chip, was mechanically damaged during pre-testing of the system, losing its electrical conductivity, and hence, its sensing capabilities. To normalize the OF extracted with the left vision chip, the average value of the shape sensor segments measured during the first experiment, 3.5° , was hardcoded and used throughout the experiment.

The boxplots representing the median and the lower and upper quartiles of the angular deflections of the seven segments of the shape sensor placed underneath the right vision chip of the right *Tape* module, registered during the experiment, are shown in Fig. 5.15. The OF vectors, OF1L-OF14L, were continuously normalized throughout the experiment according to the presented shapes.

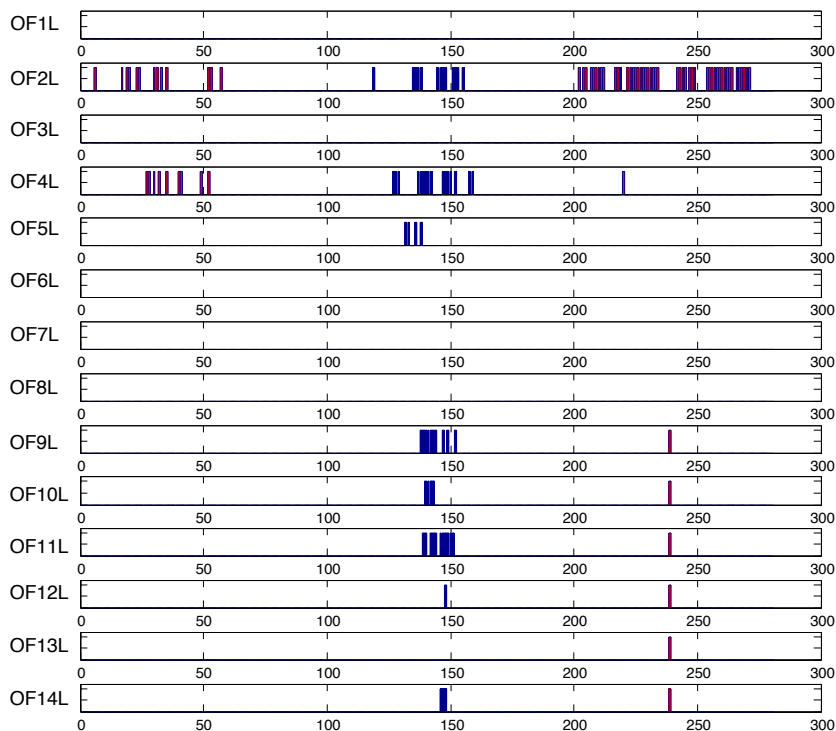
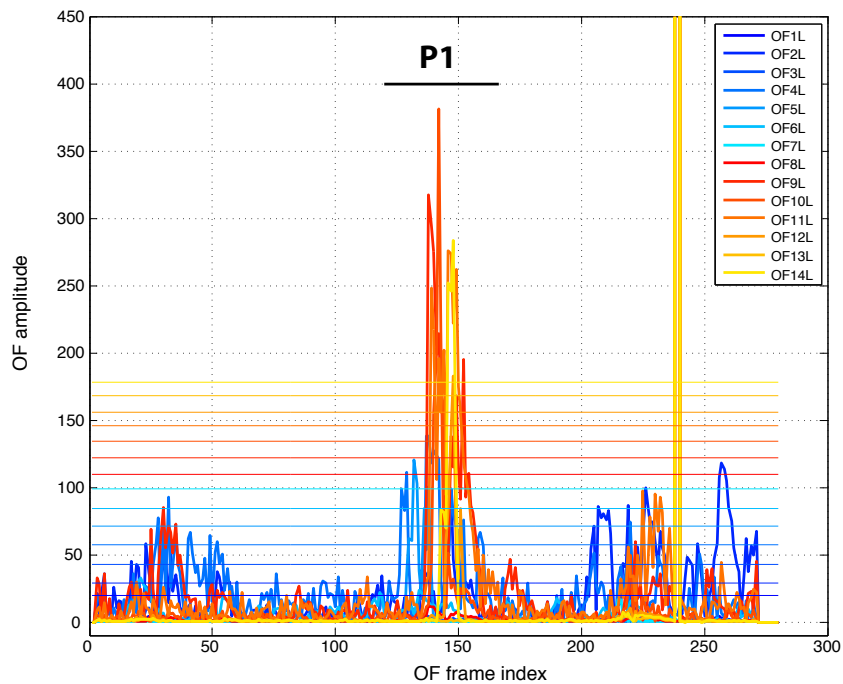


Figure 5.16: OF as a function of frame index collected during the second experiment. Top: 14 OF values of the right *Tape* module and the right and left vision chips. The threshold levels for every OF are indicated and correspond to those presented in Fig. 5.10. Bottom: the frame indexes of OF threshold crossing are indicated for each vector individually. The single event of the experiment, P1, is marked.

There were 405 frames registered, out of which 280 were selected for the analysis of the OF and motor activation. The OF patterns of the 14 normalized OF vectors are presented in Fig. 5.16 (top). It can be observed that the OF amplitudes show generally higher values than the ones observed during the first experiment. This is caused by the additional motion of the *VisionHat* user not present during the first experiment. Also, due to the self-motion of the user, the OF pattern is more erratic, which causes more false feedback activations. The OF amplitudes crossing the corresponding thresholds are marked individually for every OF vector in Fig. 5.16 (bottom). Similar to the first experiment, the first false feedback activation (frame index 5) was triggered by the OF2L vector. It was followed approximately 0.5 s later by the threshold crossing of the OF4L vector. The first feedback activation of the P1 event occurred also due to the OF2L vector. The following threshold crossing sequence during the event was subsequently observed: OF4L, OF5L, OF9L, OF11L, OF10L, OF14L and OR12L. Just as during the first experiment, the propagation of the moving object in the FOV of the sensor can also be observed through the threshold crossing sequence.

Apart from the first false activation before the event, there was a second false activation approximately 40 frames (1 s) after the event. It originated from the OF2RL vector and was most likely a result of noise. However at the same time, a peak of the OF amplitudes across the vectors OF9L-OF14L, calculated within the FOV of the right vision chip, occurred. The simultaneous threshold crossing by the vectors of the same vision chip suggests a temporal malfunction of the chip and points to it as a source of the false feedback activation.

5.3.3 Discussion

The results presented here show that the *VisionHat* system can indeed identify the motion present in proximity to the user and activate the corresponding feedback signal. The proposed thresholding of the OF values provide an easy and comprehensive mechanism for feedback activation. Moreover, by modifying the threshold levels, the sensitivity of the feedback activation can be potentially tuned based on the individual preferences of the users.

Nevertheless, the presence of false activations observed during both experiments diminishes the importance of the provided feedback and should be eliminated. I see two independent sources of false feedback activation. First, the presence of noise. Due to the low feedback activation threshold values of the OF vectors pointing in the direction of motion, spontaneous feedback activation occurs. It was observed during the first and the second experiment that false feedback activation was triggered by the OF2L vector, the one with the second smallest threshold value among all. Moreover

during the second experiment, false feedback activation was also triggered by the OF4L vector, corresponding to the fourth smallest threshold value. To eliminate such false feedback activations, I suggest to increase the feedback activation thresholds for the four central OF vectors, OF1L-OF4L and OF14R-OF11R, and to equalize them to the level of the adjacent vectors OF5L and OF10R, respectively. In practical use, such threshold elevation may eliminate these vectors from the feedback activation process. This would effectively reduce the global perceptive FOV of the system by approximately 26° around the direction of motion.

The second source of false activation is the motion induced by the user of the system. Indeed, the additional motion of the user elevates the OF amplitudes and facilitates OF threshold crossing. It can be observed when comparing the results of the first and the second experiment that the presence of additional motion results in more false feedback activations. To reduce the number of such false feedback activations, I suggest to link the feedback activation thresholds to the motion of the user, in particular the translational velocity. However, in practice such a link may not be trivial to achieve as additional system tracking of ego-motion during long-time operation would have to be introduced. The onboard IMU unit could provide such information. Velocity can be estimated by continuous integration of the acceleration measurements. However, such a procedure is known to diverge from the real velocity value due to a drift of the sensing units. Moreover, the correct relationship between the motion and the threshold would have to be derived through human experiments.

5.4 Discussion

It is important to understand that the *VisionHat* system described here is not limited to the presented configuration and can be further extended by increasing the number of the modules and modifying their spatial arrangement. Extension allows covering larger surfaces and increasing the overall FOV of the system for motion detection from other directions. For instance the system may be integrated with something other than a baseball cap, *e.g.*, clothing such as a T-shirt or belt, to provide similar functionality to that presented.

Although the prototype shows certain limitations, it serves as a proof of concept only and allows assessment of the functionality, wearability and information transfer of the system. In particular, the wearability and ergonomics of the system, not explicitly presented in the previous sections, are addressed. Overall ergonomics may be particularly important in the case of users having movement or vision deficiency, whose ability to put on, adjust, clean and operate the device is limited. The compact and

lightweight design of the *VisionHat*, integration with the baseball cap, the possibility of quick battery replacement and intuitive activation of the feedback signals address this challenge.

5.5 Conclusions

Integration of the perviously developed elements, the Vision Tape, the shape sensor and the feedback system into a baseball cap created the *VisionHat* system described in this chapter.

The system possesses a modular design that supports extensions towards larger surfaces. Such extensions may provide an increase of the overall FOV of the system for motion detection from directions not proposed with the current prototype. Moreover, the proposed data exchange scheme facilitates module rearrangements, as assignment of one address per module is only required. Increasing the number of modules may, however, lead to a slower operation of the system as amount of data exchanged in every communication cycle (between the *Brain* and the *Nerve* modules) is proportional to the number of *Nerve* modules active in the system.

As investigated in other works, unnoticeable appearance of the system to external observers is particularly important for visually impaired people. This challenge is addressed through integration of the system components inside the concavity of the cap. Two rectangular windows, cut in the front part of the cap, show the only visual evidence of the system to an external observer. Moreover for better camouflage of the system, caps of different colors are investigated.

The presented experiments mimic system operation in natural environments. In particular in the office-like room, the system is capable of detecting the surrounding motion in close proximity to the user. Subsequently, the system accurately activates the feedback signal, providing the motion-related information through vibrations. In the outdoor environment, the system supports a walking user in detecting an incoming person by activating the vibration feedback.

Nevertheless, false activation of the feedback was also observed. Sources of such activations are discussed and two solutions are proposed. In particular, threshold elevation for the OF values around the direction of motion and incorporation of ego-motion information in the feedback activation process are suggested.

6 Conclusions and Outlook

In this thesis I introduced *VisionHat*, a wearable ETA system aimed at extending autonomous mobility of visually impaired people by detection and communication of collision dangers present in the surrounding proximity. The *VisionHat* displays significant advantages over the existing ETA systems, such as good wearability, reflected through its compact, lightweight design, seamless integration with clothes and its highly intuitive feedback system. The *VisionHat* consists of two main parts: a flexible OF sensor and a vibrotactile display.

The main function of the flexible OF sensor, the Vision Tape (VT), is the detection of motion. Collision dangers are determined through a specifically designed thresholding process applied to the OF. The VT supports motion extraction under flat and bent configurations as well as during dynamic deformations. In this thesis the impact of the VT deformation on the extracted OF is studied and the optimal configuration for motion extraction is derived. The obtained results show a drop of sensor performance in flat and bent configurations that are far from the optimal one. The performance drop is a result of the optical independence of the ommatidia and the fact of the overlap of their FOV during bending. To overcome this limitation, a normalization method is developed. The method allows maintenance of an optimal level of OF amplitude for an arbitrary configuration of the flexible sensor. Monitoring of the shape, required by the normalization method, is performed with an array of the custom-developed hyperflexible strain gauges. A novel read-out strategy, which is applied to the strain gauge array, allows enhancement of spatial and angular resolution during the measurement process.

The main function of the vibrotactile display is to communicate collision danger events to the user. The design and the control of the display are derived through a series of human studies. The three main findings of these studies, namely the value of the comfort strength of the vibrations, the results of the multi-point stimulation

Chapter 6. Conclusions and Outlook

and the dependence of the position of the stimuli on the precision of its localization, provide collision-alert feedback in a comprehensible manner.

The wearability of the system is demonstrated by its integration with a baseball cap. Due to its inherent flexibility, the VT sensor complies with the natural flexibility of the cap, which improves comfort in wearing the system over extended periods of time. Moreover, the thin package of the VT, the small size of the vibrotactile display and their positioning in the concavity allow unnoticeable integration with the cap.

The *VisionHat* system is tested in two scenarios mimicking everyday-life situations. The performance of the system is assessed when worn in an indoor, office-like room, and during outdoor walking. Extraction of the OF and the subsequent activation of the vibration feedback are demonstrated when approaching a potential obstacle.

Despite the demonstrated capabilities of the developed prototype, certain drawbacks are still present in the *VisionHat* system as well as in its individual elements. On the system level, false activations of the feedback were observed in the undertaken experiments. A possible source of this issue is the limited performance of the thresholding process in the present implementation. To address this issue I propose to reduce the effective FOV around the direction of motion of the user and tie the feedback activation threshold to the ego-velocity of the user. Such an approach may lead to a better balance between the OF amplitudes extracted during the motion and the feedback activation thresholds, reducing the impact of the noise on the process of feedback activation.

Regarding the individual elements of the system, further improvements could address the understanding of the quantitative impact of the physical parameters of the flexible OF sensor (such as acceptance angle, interommatidia angle, ommatidia pitch, light sensitivity profile and other) on the patterns of the OF extracted under bent configurations of the sensor. This thorough understanding would give quantitative insight into the design of a flexible sensor performing OF extraction in an optimal manner. Alternatively, the possibility of extracting motion related information within a single ommatidium could be explored. With such a possibility, the need for OF normalization could be overcome.

Also, the performance of the hyper-flexible strain gauge could be optimized. In particular the observed hysteresis impairs the angular resolution of the sensor. Patterning the sensitive element of the strain gauge into a zig-zag, which is typically found in analogue metal strain gauges, would increase the sensitivity and hence the angular resolution. Alternatively, a newly developed contactless deflection sensor could be utilized. The sensor shows good angular resolution and no hysteresis. However, further

developments, addressing the challenges of miniaturization and integration, would have to be performed first.

Despite the mentioned limitations, the current instantiation of the *VisionHat* may support visually impaired people in certain tasks, including perception of objects moving in the peripheral vision area. Moreover, with further developments the *VisionHat* system could truly extend mobility autonomy of visually impaired people by providing an easy-to-use, multidirectional and highly reliable collision alert system complementary to the traditionally used white cane.

Beside the presented application, the *VisionHat* systems can serve as a good base for addressing other applications, where wearability, wide FOV and mechanical compliance are indispensable. It has been shown that omnidirectional FOV is particularly beneficial for odometry [126]. The functionality of the *VisionHat* could be extended in this direction and provide users with localization information. Moreover, by imposing a desired geometry to the flexible OF sensor by its active deformation, the angular density of the OF information could be adapted to the needs of an encountered application or a situation. For instance, one could imagine the sensor in a bent configuration for omnidirectional collision detection or odometry. With its subsequent morphing to a flat configuration the sensor would enhance collision detection in a particular direction. Additionally, to the best of my knowledge, the possibility of taking advantage of the mechanical properties of the flexible vision sensors and to integrate them into soft robotic platforms has not been explored yet. Indeed, the VT in combination with shape monitoring system could fill this gap, providing functionalities already observed in rigid platforms equipped in OF sensors. Applications such as collision avoidance or ego-motion estimation could be targeted. Finally, flexible OF sensors could be integrated with other objects like furniture or cars without knowing the shape of the subjacent surface a priori.

A Appendix A: Vision Tape

A.1 First Prototype Design, Image Formation and Image Processing

The mechanical layout of the first VT prototype with dimensions is presented in Fig. A.1. The maximum thickness of the device is only 2.5 mm and the total weight is 2.8 g. The chosen photosensitive elements of the pixels are PT100MCOMP phototransistors (Sharp, Japan). It operates in the visible light spectrum from 400 nm to the peak in 900 nm, bearing a linear characteristic in this region. The spatial sensitivity of the phototransistor has a Gaussian distribution with its half-sensitivity in an angle of 15° from the perpendicular to the phototransistor surface ($\Delta\rho=30^\circ$).

The scheme of the VT operation is presented in Fig. A.2. The read-out and image processing is carried out by a dsPIC33FJ12GP202 microcontroller (Microchip). For the read-out, the photodiodes are connected to a common signal line and pixels are switched on and off in sequence, reconstructing the full frame (eight pixels from no. 0 to no. 7, in the order) in the microcontroller memory. At the end of the line, a 10-bit ADC integrated in the microcontroller digitalizes the signal. The imager is supplied with a 5V voltage through a USB port. The total current consumption is 54 mA. The frame is collected in the microcontroller and sent subsequently to a PC application through an UART-to-USB transceiver.

In Fig. A.3 the image formation is compared for VT reaching convex ($\Delta\phi > 0$) (left) and concave ($\Delta\phi < 0$) (right) shape, for object placed in distances **d1** (top) and **d2** (middle) from the imager. The viewing directions of every pixel is marked with dashed line. The order of the pixels "seeing" the object is summarize in the tables on the bottom of the figure. In general, for every given distance **d** the order of the pixels can only be preserved in convex and flat configurations of the VT and therefore, only

Appendix A. Appendix A: Vision Tape

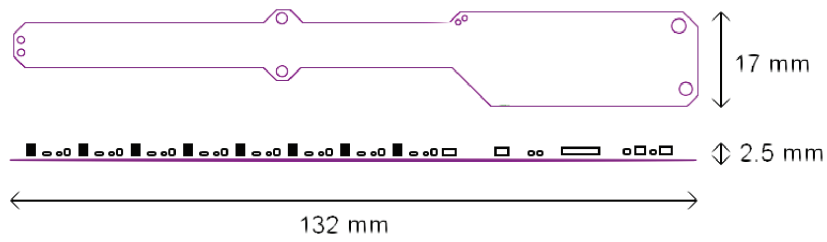


Figure A.1: Mechanical layout of the Vision Tape with dimensions. Top view (top), side view (bottom).

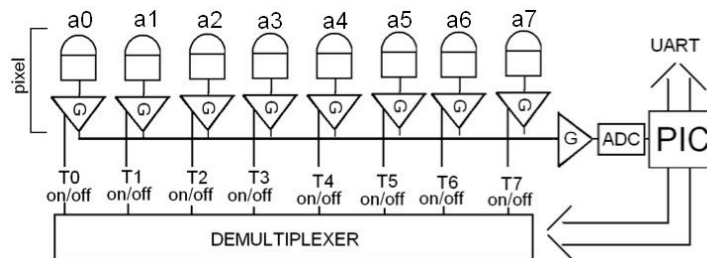


Figure A.2: Vision Tape scheme of operation. Eight photodiodes (a0-a7) are attached to the common signal line through an on/off operational amplifier. At the end of the signal line, analog-to-digital converter digitalizes the signal. By activating the amplifiers in a sequence T0-T7, the microcontroller reads the value of the current state of the photodiode and reconstructs the entire frame every 1 ms.

A.1. First Prototype Design, Image Formation and Image Processing

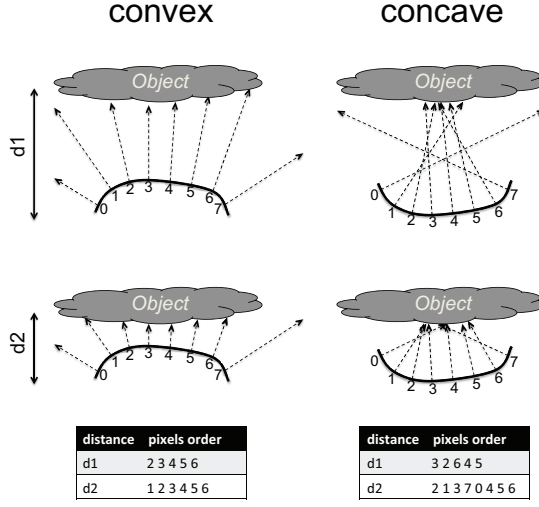


Figure A.3: Arbitrary convex (left) and concave (right) configurations of the VT placed in a distances $\mathbf{d1}$ (top) and $\mathbf{d2}$ (middle) from the observed object. The dashed line is perpendicular to the VT surface and indicates the center of the FOV of every pixel, what corresponds to viewing direction of this pixel. The table (bottom) summarizes the order of the pixels "seeing" the object for both distances.

these configurations allow the correct reconstruction of the image frame. The correct reconstruction of the image frame with the VT reaching the concave configuration is possible, only if the distance to the object is known.

OF is used to calculate the motion vector out of two subsequent frames [36, 37]. To calculate it, a simplified version [39] of the image-interpolation algorithm (I2A) [40] is used here. The I2A algorithm is based on the spatial interpolation of two subsequent frames. The algorithm provides linear estimation of the motion and is independent of contrast. However, a minimum of three pixels are required to calculate a single OF vector.

As OF is proportional to the translational and rotational component of the motion and inversely proportional to the distance to the object, proximity D to the object can be estimated based on the *motion parallax* principle [41]:

$$D(\alpha) \cong \frac{|\mathbf{T}|}{\mathbf{p}(\alpha)} \cdot \sin(\alpha), \quad (\text{A.1})$$

where $|\mathbf{T}|$ is a translational velocity of the camera, \mathbf{p} is a translational component of the OF and α indicates the orientation of the camera wrt. the direction of the movement. To estimate $D(\alpha)$ we assume $|\mathbf{T}|$ to be constant. Therefore, $D(\alpha)$ provides a proximity parameter that is proportional to the distance to the object and the egomotion of the camera.

Table A.1: Main geometrical and optical parameters of the first VT prototype.

Fig. 2.4	A	B	C	D
$\Delta\phi$ [$\Delta\rho$]	0	0.25	0.5	1
$\Delta\phi$ [°]	0	7.5	15	30
global FoV [°]	30	90	150	270
X [1/°]	∞	48	24	12
r [mm]	∞	76.4	38.2	19.1
l [mm]	18.7	25.1	38	∞

A.2 Experimental set-up

I characterize rotational and translational components of the OF vector under three sub-optimal shapes and the optimal shape of the VT imager as presented in Fig. 2.4 A-C and D respectively. The desired pixel-to-pixel angle $\Delta\phi$ is achieved by glueing the VT onto the cylinder of a radius r , calculated as $r = \frac{360^\circ d}{2\pi\Delta\phi}$. In addition, I calculate depth of focus l ($l = \frac{d}{2} \cdot \tan\left(90 + \frac{\Delta\phi}{2} - \Delta\rho\right)$), which defines a distance from the camera at which the FoV of two adjacent pixels start to overlap (Fig. 2.4 I). To extract OF distance, l must be shorter then the distance to the object $l_o < l$ in order to guarantee the continuity of the global FOV of the imager. The main geometrical and optical parameters for every configuration of the sensor are listed in table A.1.

To extract the rotational component of the OF, the VT was attached to the turret of a two-wheeled e-puck robot [47]. OF is calculated over the whole FOV of the imager, *i.e.* 8 pixels (a0-a7). The experimental set-up allowed the imager to spin around the center of the robot with rotational speed controlled by the tachometers placed in the robot wheels. The robot is placed in the center of a circular arena consisting of a wall painted with vertical black-and-white stripes of 5 mm width each. The radius of the arena is 300 mm. The light is provided by a 75 W wolfram bulb placed 850 mm above the arena, providing a luminance of 470 lux on the arena's surface. OF is measured with the robot turning clockwise (counterclockwise) at angular speeds of: 1 (-1) rad/s, 0.8 (-0.8) rad/s, 0.7 (-0.7) rad/s, 0.5 (-0.5) rad/s, 0.25 (-0.25) rad/s, 0.1 (-0.1) rad/s.

To extract translational component of the OF, the two-wheel e-puck robot was used to control the translational speed of the imager. The robot moves straight towards the flat arena wall from a starting distance of 200 mm with a speed of 20 mm/s. Thus, the OF is free of rotational components due to the character of the movement. The size of

A.2. Experimental set-up

the arena is 500 mm x 500 mm. The FOV of the imager is divided into two regions: Left, with pixels a0-a3, and Right, with pixels a4-a7. The OF is calculated independently over each region. OF samples are acquired every 0.5 s, which corresponds to a distance resolution of 10 mm. All experiments are repeated ten times for every speed and imager configuration.

B Appendix B: Shape Sensing

B.1 Contactless Deflection Sensor - Electromechanical Design and Signal Processing

The electronic elements of the system as well as the signal and power flows are presented in Fig. B.1. The main component of the data acquisition, processing and communication block is the digital signal processing microcontroller dsPIC128GP802 (Microchip). The output current from every PD is converted to voltage using 10 k Ω 0.1% resistor. Next, the voltage signal goes through the low-resistance analog demultiplexer, the active low-pass filter with a cut-off frequency of 1.5 kHz and is digitalized by the microcontroller-integrated 12 bits analog-digital converter (ADC). The obtained digital values are sent to a Matlab interface through the UART-to-USB transceiver (FTDI Ltd). The system is designed to obtain the saturation of the ADC for the PD illumination of 2500 lux. This parameter can be changed by using different current-to-voltage conversion ratio. However, with the increase of the saturation level, the decrease of the DS sensitivity should be expected.

The LEDs are driven by the microcontroller in such a way, so when one LED is ON the remaining ones are OFF. This is to enforce the local sensing only, *i.e.*, to prevent from impact of light emitted by LED of one cell to light registered by PDs of another cell. This is also to allow the ambient light cancelation as described in the section 3.2.1.

The total power consumption of the system is 70 mA, which allows it to be powered directly from a USB port of a standard computer. The global state of the system, *i.e.*, the measurement of deflection of all 12 DS, is refreshed every 30 ms (33 Hz).

Appendix B. Appendix B: Shape Sensing

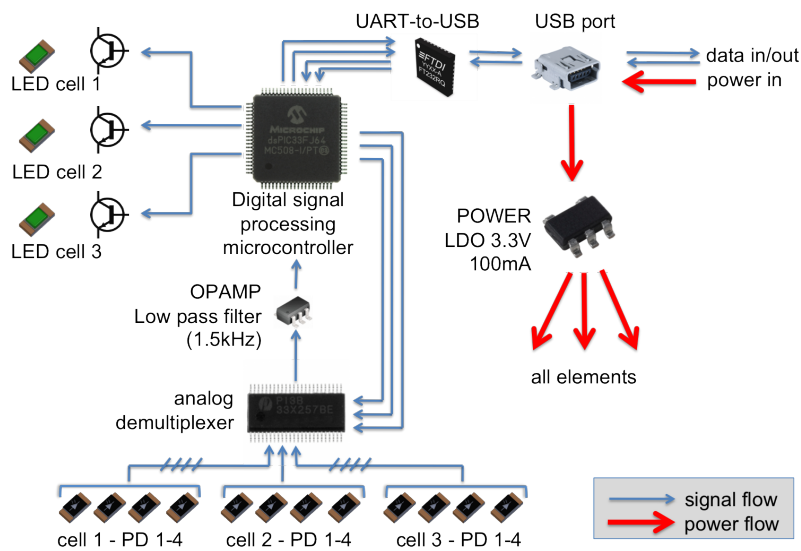


Figure B.1: Composing elements, signal flow and power flow of the deflection monitoring system. Digital signal processing microcontroller controls the data acquisition of 12 photodiodes by addressing the analog demultiplexer. Before the data is digitalized by the microcontroller-integrated 12-bits ADC it is filtered by the first order FIR low-pass filter realized with a low-noise operational amplifier (OPAMP). The microcontroller controls the ON/OFF switching sequence of every cell's LED through the npn transistor. The data collected in the microcontroller's memory is processed and sent to an external application for the visualization purposes through the UART-to-USB transceiver and a mini USB port. Power is provided to every element of the system through the USB port on the computer.

B.2 Hyper-Flexible Strain Gauge Based on Stretchable-Gold-Deposited-on-PDMS Technology

$$\begin{bmatrix}
 1 & 0 & 0 & 0 & 0 & 0 & 0 & 1 & 0 & 0 & 0 & 0 & 0 \\
 1 & 1 & 0 & 0 & 0 & 0 & 0 & 0 & 1 & 0 & 0 & 0 & 0 \\
 1 & 1 & 1 & 0 & 0 & 0 & 0 & 0 & 0 & 1 & 0 & 0 & 0 \\
 1 & 1 & 1 & 1 & 0 & 0 & 0 & 0 & 0 & 0 & 1 & 0 & 0 \\
 1 & 1 & 1 & 1 & 1 & 0 & 0 & 0 & 0 & 0 & 0 & 1 & 0 \\
 1 & 1 & 1 & 1 & 1 & 1 & 0 & 0 & 0 & 0 & 0 & 0 & 1 \\
 1 & 1 & 1 & 1 & 1 & 1 & 1 & 0 & 0 & 0 & 0 & 0 & 0 \\
 0 & 1 & 0 & 0 & 0 & 0 & 0 & 1 & 1 & 0 & 0 & 0 & 0 \\
 0 & 1 & 1 & 0 & 0 & 0 & 0 & 1 & 0 & 1 & 0 & 0 & 0 \\
 0 & 1 & 1 & 1 & 0 & 0 & 0 & 1 & 0 & 0 & 1 & 0 & 0 \\
 0 & 1 & 1 & 1 & 1 & 0 & 0 & 1 & 0 & 0 & 0 & 1 & 0 \\
 0 & 1 & 1 & 1 & 1 & 1 & 0 & 1 & 0 & 0 & 0 & 0 & 1 \\
 0 & 1 & 1 & 1 & 1 & 1 & 1 & 1 & 0 & 0 & 0 & 0 & 0 \\
 0 & 0 & 1 & 0 & 0 & 0 & 0 & 0 & 1 & 1 & 0 & 0 & 0 \\
 0 & 0 & 1 & 1 & 0 & 0 & 0 & 0 & 1 & 0 & 1 & 0 & 0 \\
 0 & 0 & 1 & 1 & 1 & 0 & 0 & 0 & 1 & 0 & 0 & 1 & 0 \\
 0 & 0 & 1 & 1 & 1 & 1 & 0 & 0 & 1 & 0 & 0 & 0 & 1 \\
 0 & 0 & 1 & 1 & 1 & 1 & 1 & 0 & 1 & 0 & 0 & 0 & 0 \\
 0 & 0 & 0 & 1 & 0 & 0 & 0 & 0 & 0 & 1 & 1 & 0 & 0 \\
 0 & 0 & 0 & 1 & 1 & 0 & 0 & 0 & 0 & 1 & 0 & 1 & 0 \\
 0 & 0 & 0 & 0 & 1 & 1 & 1 & 0 & 0 & 0 & 1 & 0 & 0 \\
 0 & 0 & 0 & 0 & 1 & 1 & 1 & 0 & 0 & 0 & 1 & 0 & 0 \\
 0 & 0 & 0 & 0 & 0 & 1 & 0 & 0 & 0 & 0 & 0 & 1 & 1 \\
 0 & 0 & 0 & 0 & 0 & 1 & 1 & 0 & 0 & 0 & 0 & 1 & 0 \\
 0 & 0 & 0 & 0 & 0 & 0 & 1 & 0 & 0 & 0 & 0 & 0 & 1
 \end{bmatrix}
 \times
 \begin{bmatrix}
 Rx_1 + Rc_1 \\
 Rx_2 \\
 Rx_3 \\
 Rx_4 \\
 Rx_5 \\
 Rx_6 \\
 Rx_7 + Rc_8 \\
 Rc_2 \\
 Rc_3 \\
 Rc_4 \\
 Rc_5 \\
 Rc_6 \\
 Rc_7
 \end{bmatrix}
 =
 \begin{bmatrix}
 \frac{Us \cdot Rref}{Ur_1} \\
 \vdots \\
 \frac{Us \cdot Rref}{Ur_{28}}
 \end{bmatrix}
 - Rref(B.1)$$

$$Rx_1 + Rc_1 = \frac{Us \cdot Rref}{2} \left(\frac{1}{Ur_1} + \frac{1}{Ur_7} - \frac{1}{Ur_{13}} \right) - \frac{Rref}{2} \quad (B.2)$$

$$Rx_2 = \frac{Us \cdot Rref}{2} \left(-\frac{1}{Ur_1} + \frac{1}{Ur_2} + \frac{1}{Ur_{13}} - \frac{1}{Ur_{18}} \right) \quad (B.3)$$

$$Rx_3 = \frac{Us \cdot Rref}{2} \left(-\frac{1}{Ur_2} + \frac{1}{Ur_3} + \frac{1}{Ur_{18}} - \frac{1}{Ur_{22}} \right) \quad (B.4)$$

$$Rx_4 = \frac{Us \cdot Rref}{2} \left(-\frac{1}{Ur_3} + \frac{1}{Ur_4} + \frac{1}{Ur_{22}} - \frac{1}{Ur_{25}} \right) \quad (B.5)$$

$$Rx_5 = \frac{Us \cdot Rref}{2} \left(-\frac{1}{Ur_4} + \frac{1}{Ur_5} + \frac{1}{Ur_{25}} - \frac{1}{Ur_{27}} \right) \quad (B.6)$$

$$Rx_6 = \frac{Us \cdot Rref}{2} \left(\frac{1}{Ur_5} - \frac{1}{Ur_7} + \frac{1}{Ur_{27}} \right) - \frac{Rref}{2} \quad (B.7)$$

$$Rx_7 + Rc_8 = \frac{Us \cdot Rref}{2} \left(-\frac{1}{Ur_6} + \frac{1}{Ur_7} + \frac{1}{Ur_{28}} \right) - \frac{Rref}{2} \quad (B.8)$$

$$Rc_2 = \frac{Us \cdot Rref}{2} \left(\frac{1}{Ur_1} - \frac{1}{Ur_7} + \frac{1}{Ur_{13}} \right) - \frac{Rref}{2} \quad (B.9)$$

$$Rc_3 = \frac{Us \cdot Rref}{2} \left(\frac{1}{Ur_2} - \frac{1}{Ur_7} + \frac{1}{Ur_{18}} \right) - \frac{Rref}{2} \quad (B.10)$$

$$Rc_4 = \frac{Us \cdot Rref}{2} \left(\frac{1}{Ur_3} - \frac{1}{Ur_7} + \frac{1}{Ur_{22}} \right) - \frac{Rref}{2} \quad (B.11)$$

$$Rc_5 = \frac{Us \cdot Rref}{2} \left(\frac{1}{Ur_4} - \frac{1}{Ur_7} + \frac{1}{Ur_{25}} \right) - \frac{Rref}{2} \quad (B.12)$$

$$Rc_6 = \frac{Us \cdot Rref}{2} \left(\frac{1}{Ur_5} - \frac{1}{Ur_7} + \frac{1}{Ur_{27}} \right) - \frac{Rref}{2} \quad (B.13)$$

$$Rc_7 = \frac{Us \cdot Rref}{2} \left(\frac{1}{Ur_6} - \frac{1}{Ur_7} + \frac{1}{Ur_{28}} \right) - \frac{Rref}{2} \quad (B.14)$$

Bibliography

- [1] S.S. Lane, B.D. Kuppermann, I.H. Fine, M.B. Hamill, J.F. Gordon, R.S. Chuck, R.S. Hoffman, M. Packer, and D.D. Koch. A prospective multicenter clinical trial to evaluate the safety and effectiveness of the implantable miniature telescope. *American Journal of Ophthalmology*, 137(6):993–1001, JUN 2004.
- [2] K.A. Colby, D.F. Chang, D. Stulting, and S.S. Lane. Surgical placement of an optical prosthetic device for end-stage macular degeneration - The implantable miniature telescope. *Archives of Ophthalmology*, 125(8):1118–1121, AUG 2007.
- [3] D.B. Shire, S.K. Kelly, J. Chen, P. Doyle, M.D. Gingerich, S.F. Cogan, W.A. Drohan, O. Mendoza, L. Theogarajan, J.L. Wyatt, and J.F. Rizzo. Development and implantation of a minimally invasive wireless subretinal neurostimulator. *Biomedical Engineering, IEEE Transactions on*, 56(10):2502–2511, 2009.
- [4] S. Nirenberg and C. Pandarinath. Retinal prosthetic strategy with the capacity to restore normal vision. *Proceedings of the National Academy of Science of the United States of America*, 109(37):15012–15017, SEP 11 2012.
- [5] K.A. Kaczmarek, J.G. Webster, P. Bach-y Rita, and W.J. Tompkins. Electrotactile and vibrotactile displays for sensory substitution systems. *IEEE Transactions on Biological Engineering*, 38(1):1 – 16, 1991.
- [6] S. Mau, N. Melchior, M. Makatchev, and A. Steinfeld. Blindaid: An electronic travel aid for the blind. Technical Report CMU-RI-TR-07-39, Robotics Institute, Pittsburgh, PA, May 2008.
- [7] R.C. Nelson and J. Aloimonos. Obstacle avoidance using flow field divergence. *Pattern Analysis and Machine Intelligence, IEEE Transactions on*, 11(10):1102–1106, 1989.
- [8] M.O. Franz and H.A. Mallot. Biomimetic robot navigation. *Robotics and Autonomous Systems*, 30(1-2):133 – 153, 2000.

Bibliography

- [9] F. Ruffier and N. Franceschini. Optic flow regulation: the key to aircraft automatic guidance. *Robotics and Autonomous Systems*, 50(4):177 – 194, 2005.
- [10] J.-C. Zufferey and D. Floreano. Fly-inspired visual steering of an ultralight indoor aircraft. *IEEE Transactions on Robotics*, 22:137–146, 2006.
- [11] A. Beyeler, J.-Z. Zufferey, and D. Floreano. Vision-based control of near-obstacle flight. *Autonomous Robots*, 27(3):201–219, 2009.
- [12] S. Zingg, D. Scaramuzza, S. Weiss, and R. Siegwart. Mav navigation through indoor corridors using optical flow. In *Robotics and Automation (ICRA), 2010 IEEE International Conference on*, pages 3361–3368, 2010.
- [13] H. Dahmen, A. Millers, and H.A. Mallot. Insect-inspired odometry by optic flow recorded with optical mouse chips. In Dario Floreano, Jean-Christophe Zufferey, Mandyam V. Srinivasan, and Charlie Ellington, editors, *Flying Insects and Robots*, pages 115–126. Springer Berlin Heidelberg, 2010.
- [14] R. Sorabji. Aristotle on demarcating the five senses. *Philosophical Review*, 80(1):55–79, 1971.
- [15] P. Bach-Y-Rita. Vision substitution by tactile image projection. *Nature*, 221:963–964, 1969.
- [16] G. Sainarayanan, R. Nagarajan, and S. Yaacob. Fuzzy image processing scheme for autonomous navigation of human blind? *Applied Soft Computing*, 7(1):257–264, 2007.
- [17] P.B.L. Meijer. An experimental system for auditory image representations. *IEEE Transactions on Biomedical Engineering*, 39:112–121, 1992.
- [18] N. Bourbakis, R. Keefer, D. Dakopoulos, and A. Esposito. A multimodal interaction scheme between a blind user and the tyflos assistive prototype. In *Proceedings of the 2008 20th IEEE International Conference on Tools with Artificial Intelligence - Volume 02, ICTAI '08*, pages 487–494. IEEE Computer Society, 2008.
- [19] A. Rodriguez, J. J. Yebes, P. F. Alcantarilla, L. M. Bergasa, Javier Almazan, and A. Cela. Assisting the visually impaired: Obstacle detection and warning system by acoustic feedback. *Sensors*, 12(12):17476–17496, 2012.
- [20] D.A. Atchison and G. Smith. *Optics of the Human Eye*. Butterworth-Heinemann, Oxford, UK, 2000.

- [21] M. Bouzit, A. Chaibi, K.J. De Laurentis, and C. Mavroidis. Tactile feedback navigation handle for the visually impaired. In *ASME International Mechanical Engineering Congress and RD&D Expo, Anaheim*, pages 1–8, 2004.
- [22] K. Ito, M. Okamoto, J. Akita, T. Ono, I. Gyobu, T. Takagi, T. Hoshi, and Y. Mishima. Cyarm: an alternative aid device for blind persons. In *CHI '05: CHI '05 extended abstracts on Human factors in computing systems*, pages 1483–1488, New York, NY, USA, 2005. ACM.
- [23] S. Cardin, F. Vexo, and D. Thalmann. Wearable System for Mobility Improvement of Visually Impaired People. *Visual computer journal*, 23:109 – 118, 2006.
- [24] J.S. La Grow. The use of the sonic pathfinder as a secondary mobility aid for travel in business environments: a single-subject. *Journal of Rehabilitation Research and Development*, 36(4), 1999.
- [25] <http://www.sonicpathfinder.org/>. Sonicpathfinder website, 2010.
- [26] T. Ifukube, T. Sasaki, and P. Peng. A blind mobility aid modeled after echolocation of bats. *IEEE Transactions on Biological Engineering*, 38(5):461–465, 1991.
- [27] M.K. Dobrzynski, R. Pericet-Camara, and D. Floreano. Vision tape - a flexible compound vision sensor for motion detection and proximity estimation. *Sensors Journal, IEEE*, 12(5):1131 –1139, may 2012.
- [28] H. Saito, K. Hoshino, K. Matsumoto, and I. Shimoyama. Compound eye shaped flexible organic image sensor with a tunable visual field. In *18th IEEE International Conference on Micro Electro Mechanical Systems, MEMS 2005.*, pages 96–99, Feb. 2005.
- [29] Y. Nomura, L. Zhang, and S.K. Nayar. Scene Collages and Flexible Camera Arrays. In *Proc. of Eurographics Symposium on Rendering*, Jun 2007.
- [30] F. Sorin, O. Shapira, A. F. Abouraddy, M. Spencer, N.D. Orf, J.D. Joannopoulos, and Y. Fink. Exploiting collective effects of multiple optoelectronic devices integrated in a single fiber. *Nano Letters*, 9(7):2630–2635, 2009.
- [31] J.J. Boland. Flexible electronics: Within touch of artificial skin. *Nature Materials*, online:1476–4660, 09 2010.
- [32] N. Franceschini, J.M. Pichon, and C. Blanes. From insect vision to robot vision. *Philosophical Transactions of the Royal Society B*, 337:283–294, 1992.

Bibliography

- [33] D. Coombs, M. Herman, T.H. Hong, and M. Nashman. Real-time obstacle avoidance using central flow divergence and peripheral flow. In *Proc. of International Conference on Computer Vision*, pages 276–283, 1995.
- [34] M.A. Lewis. Visual navigation in a robot using zig-zag behavior. In *Neural Information Processing Systems 10*. MIT Press, 1998.
- [35] D. Trivedi, C.D. Rahn, W.M. Kier, and I.D. Walker. Soft robotics: Biological inspiration, state of the art, and future research. *Applied Bionics and Biomechanics*, 5:99–117, 2008.
- [36] J.J. Gibson. *The Perception of the Visual World*, volume 60. Houghton Mifflin, 1950.
- [37] B.K. Horn and P. Schunck. Determining optical flow. *Artificial Intelligence*, 17:185–203, 1981.
- [38] J.J. Koenderink and A.J. Doorn. Facts on optic flow. *Biological Cybernetics*, 56:247–254, 1987.
- [39] J.-C. Zufferey and D. Floreano. Fly-inspired visual steering of an ultralight indoor aircraft. *IEEE Transactions on Robotics*, 22(1):137 – 146, Feb. 2006.
- [40] M.V. Srinivasan. An image-interpolation technique for the computation of optic flow and egomotion. *Biological Cybernetics*, 71:401–416, 1994.
- [41] T.C. Whiteside and G.D. Samuel. Blur zone. *Nature*, 225:94–95, 1970.
- [42] M.F. Land. Compound eyes: old and new optical mechanisms. *Nature*, 287:681 – 686, 1980.
- [43] M.F. Land and D.-E. Nilsson. *Animal Eyes*. Oxford University Press, New York, United States, 2002.
- [44] J. Duparré, P. Dannberg, P. Schreiber, A. Bräuer, and A. Tünnermann. Thin compound-eye camera. *Applied Optics*, 44(15):2949–2956, 2005.
- [45] K. Jeong, J. Kim, and L.P. Lee. Biologically Inspired Artificial Compound Eyes. *Science*, 312(5773):557–561, 2006.
- [46] A. Brückner, J. Duparré, P. Dannberg, A. Bräuer, and A. Tünnermann. Artificial neural superposition eye. *Optical Express*, 15(19):11922–11933, 2007.

-
- [47] F. Mondada, M. Bonani, X. Raemy, J. Pugh, C. Cianci, A. Klapotocz, S. Magnenat, J.-C. Zufferey, D. Floreano, and A. Martinoli. The e-puck, a Robot Designed for Education in Engineering. In *Proc. of the 9th Conference on Autonomous Robot Systems and Competitions*, volume 1, pages 59–65, 2009.
- [48] J. Duparré, P. Schreiber, P. Damberg, T. Scharf, P. Pelli, R. Volkel, H.P. Herzig, and A. Brauer. Artificial compound eyes - different concepts and their application for ultra flat image acquisition sensors. In *Proc. SPIE-The International Society for Optical Engineering, Bellingham, USA*, volume 5346 of *Proc. SPIE*, 2004.
- [49] M.F. Land. Visual acuity in insects. *Annual Review of Entomology*, 42(1):147–177, 1997.
- [50] R. Etienne-Cummings. Biologically inspired visual motion detection in VLSI. *International Journal of Computer Vision*, 44:175–198, 2001.
- [51] R. Brinkworth and P. Shoemaker. Characterization of a neuromorphic motion detection chip based on insect visual system. *Intelligent Sensors Sensor Networks and Information Processing ISSNIP*, pages 289–294, 2009.
- [52] S. Viollet, F. Ruffier, T. Ray, M. Menouni, F. Aubepart, L. Kerhuel, and N. Franceschini. Characteristics of three miniature bio-inspired optic flow sensors in natural environments. *Proc. of Fourth International Conference on Sensor Technologies and Applications*, pages 51–55, 2010.
- [53] F. Expert, S. Viollet, and F. Ruffier. Outdoor field performances of insect-based visual motion sensors. *Journal of Field Robotics*, 28(4):529–541, 2011.
- [54] J.-C. Zufferey. *Bio-inspired Flying Robots: Experimental Synthesis of Autonomous Indoor Flyers*. EPFL/CRC Press, Lausanne, 2008.
- [55] D. Floreano, R. Pericet-Camara, S. Viollet, F. Ruffier, A. Bruckner, R. Leitel, W. Buss, M. Menouni, F. Expert, R. Juston, M.K. Dobrzynski, G. L'Eplattenier, F. Recktenwalde, H.A. Mallot, and N. Franceschini. A miniature curved artificial compound eye. *Proceedings of the National Academy of Sciences*, 10(13):9267–9272, 2013.
- [56] T. Delbruck and C.A. Mead. Adaptive photoreceptor with wide dynamic range. In *Circuits and Systems, 1994. ISCAS '94., 1994 IEEE International Symposium on*, volume 4, pages 339–342 vol.4, 1994.
- [57] Z. Zhang. Flexible camera calibration by viewing a plane from unknown orientations. In *ICCV*, pages 666–673, 1999.

Bibliography

- [58] J.-S. Hu, Y.-J. Chang, and Y.-L. Hsu. Calibration and data integration of multiple optical flow sensors for mobile robot localization. In *Sensor Networks, Ubiquitous and Trustworthy Computing, 2008. SUTC '08. IEEE International Conference on*, pages 464–469, June 2008.
- [59] M.K. Dobrzynski, R. Pericet-Camara, and D. Floreano. Contactless deflection sensor for soft robots. In *Intelligent Robots and Systems (IROS), 2011 IEEE/RSJ International Conference on*, pages 1913–1918. IEEE, 2011.
- [60] M.K. Dobrzynski, I. Halasz, R. Pericet-Camara, and D. Floreano. Contactless deflection sensing of concave and convex shapes assisted by soft mirrors. In *Intelligent Robots and Systems (IROS), 2012 IEEE/RSJ International Conference on*, pages 4810–4815, October 2012.
- [61] M.K. Dobrzynski, H. Vanderparre, R. Pericet-Camara, G. L'Eplattenier, S. Lacour, and D. Floreano. Hyper-flexible 1-d shape sensor. In *17th International Conference on Solid-State Sensors, Actuators and Microsystems*, June 2013.
- [62] T. Adrega and S.P. Lacour. Stretchable gold conductors embedded in pdms and patterned by photolithography: fabrication and electromechanical characterization. *Journal of Micromechanics and Microengineering*, 20(5):055025–055025, 2010.
- [63] S. Vurpillot, D. Inaudi, and J.M. Ducret. Bridge monitoring by fiber optic deformation sensors : design, emplacement and results. In *Smart Structures and Materials 1996 : Smart Systems for Bridges, Structures, and Highways*, pages 141–149. SPIE The Society of Photo-Optical Instrumentation Engineers, Washington, 1996.
- [64] X. Meng, G.W. Roberts, A.H. Dodson, S. Ince, and S. Waugh. GNSS for structural deformation and deflection monitoring: implementation and data analysis. *Spectrum*, 2006.
- [65] D.M. Brown, G.A. DeBacher, and J.V. Basmajian. Feedback goniometers for hand rehabilitation., 1979.
- [66] L. Simone and D. Kamper. Design considerations for a wearable monitor to measure finger posture. *Journal of NeuroEngineering and Rehabilitation*, 2:1–10, 2005.
- [67] D. Trivedi, C.D. Rahn, W.M. Kier, and I.D. Walker. Soft robotics: Biological inspiration, state of the art, and future research. *Applied Bionics and Biomechanics*, 5(3):99–117, 2008.

- [68] M. Otake, Y. Kagami, M. Inaba, and H. Inoue. Motion design of a starfish-shaped gel robot made of electro-active polymer gel. *Robotics and Autonomous Systems*, 40(2-3):185 – 191, 2002.
- [69] M.D Grissom, V. Chitrakaran, D. Diunno, M. Csencits, M. Pritts, B. Jones, W. McMahan, D. Dawson, C. Rahn, and J. Walker. Design and experimental testing of the octarm soft robot manipulator. In *Unmanned Systems Technology VIII, PTS 1 and 2*, volume 6230 of *Proceedings of the Society of Photo-Optical Instrumentation Engineers (SPIE)*, page F2301, 2006.
- [70] K. Je-Sung and C. Kyu-Jin. Omegabot : Biomimetic inchworm robot using sma coil actuator and smart composite microstructures (scm). In *Robotics and Biomimetics (ROBIO), 2009 IEEE International Conference on*, pages 1154 –1159, dec. 2009.
- [71] Y.-L. Park, C. Majidi, R. Kramer, P. Berard, and R. J. Wood. Hyperelastic pressure sensing with a liquid-embedded elastomer. *Journal of Micromechanics and Microengineering*, 20(12), 2010.
- [72] G.H. Spencer and M.V.R.K. Murty. General ray-tracing procedure. *Journal of the Optical Society of America*, 52(6):672–676, Jun 1962.
- [73] R. L. Cook, T. Porter, and L. Carpenter. Distributed ray tracing. *ACM SIGGRAPH Computer Graphics*, 18(3):137–145, 1984.
- [74] E.-H. Park, M.-J. Kim, and Y.-S. Kwon. New fabrication technology of convex and concave microlens using uv curing method. In *LEOS '99. IEEE Lasers and Electro-Optics Society 1999 12th Annual Meeting*, volume 2, pages 639 –640 vol.2, 1999.
- [75] S.-Y. Hsiao, C.-C. Lee, and W. Fang. The implementation of concave micro optical devices using a polymer dispensing technique. *Journal of Micromechanics and Microengineering*, 18(8), 2008.
- [76] A.F. Stalder, G. Kulik, D. Sage, L. Barbieri, and P. Hoffmann. A snake-based approach to accurate determination of both contact points and contact angles. *Colloids And Surfaces A: Physicochemical And Engineering Aspects*, 286(1-3):92–103, 2006.
- [77] A.F. Stalder, T. Melchior, M. Müller, D. Sage, T. Blu, and M. Unser. Low-bond axisymmetric drop shape analysis for surface tension and contact angle measurements of sessile drops. *Colloids and Surfaces A: Physicochemical and Engineering Aspects*, 364(1-3):72–81, 2010.

Bibliography

- [78] I.M. Graz, D.P.J. Cotton, and S.P. Lacour. Extended cyclic uniaxial loading of stretchable gold thin-films on elastomeric substrates. *Applied Physics Letters*, 94(7):071902–071902–3, 2009.
- [79] M.K. Dobrzynski, S. Mejri, S. Wischmann, and D. Floreano. Quantifying information transfer through a head-attached vibrotactile display: Principles for design and control. *Biomedical Engineering, IEEE Transactions on*, 59(7):2011–2018, July.
- [80] A.D. Heyes. Human navigation by sound. *Physics in Technology*, 14(-):68–75, 1983.
- [81] D. R. Griffin. Echolocation by blind men, bats and radar. *Science*, 100(2609):589–590, 1944.
- [82] B. Masterton, H. Heffner, and R. Ravizza. The evolution of human hearing. *The Journal of the Acoustical Society of America*, 45(4):966–985, 1969.
- [83] N. Lessard, M. Pare, F. Lepore, and M. Lassonde. Early-blind human subjects localize sound sources better than sighted subjects. *Nature*, 395(6699):278–280, September 1998.
- [84] J. Zelek, R. Audette, J. Balthazaar, and C. Dunk. A stereo-vision system for the visually impaired. Technical Report 2000-41x-1, School of Engineering, University of Guelph, Guelph, ON, Canada, 2000.
- [85] A.H. Rupert. An instrumentation solution for reducing spatial disorientation mishaps - A more “natural” approach to maintaining spatial orientation. *IEEE Engineering In Medicine And Biology Magazine*, 19(2):71–80, 2000.
- [86] J.B.F. van Erp. Presenting directions with a vibrotactile torso display. *ERGONOMICS*, 48(3):302–313, 2005.
- [87] C. Wall, L.E. Oddsson, F.B. Horak, D.W. Wrisley, and M. Dozza. Applications of vibrotactile display of body tilt for rehabilitation. In *Proceedings of the 26th Annual International Conference of the IEEE-Engineering-in-Medicine-and-Biology-Society*, volume 26 of *Proceedings of the Annual International Conference of the IEEE-Engineering-in-Medicine-and-Biology-Society*, pages 4763–4765, 2004.
- [88] F. Asseman, A. M. Bronstein, and M. A. Gresty. Using vibrotactile feedback of instability to trigger a forward compensatory stepping response. *Journal Of Neurology*, 254(11):1555–1561, 2007.

- [89] M. Dozza, I.C. Wall, R.J. Peterka, L. Chiari, and F.B. Horak. Effects of practicing tandem gait with and without vibrotactile biofeedback in subjects with unilateral vestibular loss. *Journal Of Vestibular Research-Equilibrium & Orientation*, 17(4):195–204, 2007.
- [90] D. Basta and A. Ernst. Modern rehabilitation for vestibular disorders using neurofeedback training procedures. *HNO*, 56(10):990+, 2008.
- [91] J.A. Goebel, B.C. Sinks, B.E. Parker, Jr., N.T. Richardson, A.B. Olowin, and R.W. Cholewiak. Effectiveness of Head-Mounted Vibrotactile Stimulation in Subjects With Bilateral Vestibular Loss: A Phase 1 Clinical Trial. *Otology & Neurology*, 30(2):210–216, 2009.
- [92] C. Cipriani, M. D’Alonzo, and M.C. Carrozza. A miniature vibrotactile sensory substitution device for multifingered hand prosthetics. *Biomedical Engineering, IEEE Transactions on*, 59(2):400–408, 2012.
- [93] L. Cheng, R. Kazman, and J. Robinson. *Vibrotactile feedback in delicate virtual reality operations*, pages 243–251. ACM Press, 1996.
- [94] H. Regenbrecht, J. Hauber, R. Schoenfelder, and A. Maegerlein. Virtual reality aided assembly with directional vibro-tactile feedback. *Proceedings of the 3rd international conference on Computer graphics and interactive techniques in Australasia and South East Asia GRAPHITE 05*, 1(212):381, 2005.
- [95] L.A. Jones, J. Kunkel, and E. Piatetski. Vibrotactile pattern recognition on the arm and back. *Perception*, 38(1):52–68, 2009.
- [96] D. Fucci, L. Petrosino, D. Harris, and E. McMathe. Stimulus-Duration Effects On Vibrotactile Magnitude Estimation For The Tongue And Hand. *Bulletin Of The Psychonomic Society*, 24(3):193–196, 1986.
- [97] B.G. Green. The Effect Of Cooling On The Vibrotactile Sensitivity Of The Tongue. *Perception & Psychophysics*, 42(5):423–430, 1987.
- [98] D. Fucci, D. Harris, L. Petrosino, and E. Randolph Tyler. Exposure Effects On The Psychophysical Scaling Methods Of Magnitude Estimation And Cross-Modal Matching For Vibrotactile Stimulation Of The Tongue And Hand. *Perceptual And Motor Skills*, 66(2):479–485, 1988.
- [99] S. Weinstein. *Intensive and extensive aspects of tactile sensitivity as a function of body part, sex, and laterality*, pages 195–218. Charles C Thomas, 1968.

Bibliography

- [100] J.B.F. van Erp. Absolute localization of vibrotactile stimuli on the torso. *Perception & Psychophysics*, 70(6):1016–1023, 2008.
- [101] F. Thullier, B. Bolmont, and F.G. Lestienne. Vibrotactile pattern recognition: A portable compact tactile matrix. *Biomedical Engineering, IEEE Transactions on*, 59(2):525–530, 2012.
- [102] K. Gilliland and R.E. Schlegel. Tactile Stimulation of the Human Head for Information Display. *Human Factors*, 36(4):700–717, 1994.
- [103] E.A. Geldard. The Tongue Of The Skin. *Bulletin Of The British Psychological Society*, 31:49, 1957.
- [104] C.E. Sherrick. The art of tactile communication. *American Psychologist*, 30(3):353–360, 1975.
- [105] M.A. Heller and J.M. Kennedy. *The Psychology of Touch*, pages 219–233. Lawrence Erlbaum Associates, 1991.
- [106] L.A. Jones and N.B. Saftir. Tactile displays: Guidance for their design and application. *Human Factors*, 50(1):90–111, 2008.
- [107] K. Myles and J.T. Kalb. *Vibrotactile sensitivity of the head*. ARL/TR. U.S. Army Research Laboratory, 2009.
- [108] E.H. Weber. *The sense of touch*. Academic Press, 1978. original works published in 1834.
- [109] T.G. van Kooten, J.F. Whitesides, and A.F. von Recum. Influence of silicone (PDMS) surface texture on human skin fibroblast proliferation as determined by cell cycle analysis. *Journal Of Biomedical Materials Research*, 43(1):1–14, 1998.
- [110] S.H. Hsu and H.J. Tseng. In vitro biocompatibility of PTMO-based polyurethanes and those containing PDMS blocks. *Journal of Biomaterials Applications*, 19(2):135–146, 2004.
- [111] M.M. Merzenich and T. Harrington. The sense of flutter-vibration evoked by stimulation of the hairy skin of primates: Comparison of human sensory capacity with the responses of mechanoreceptive afferents innervating the hairy skin of monkeys. *Experimental Brain Research*, 9:236–260, 1969.
- [112] R.W. Cholewiak and A.A. Collins. Vibrotactile Pattern-Discrimination and Communality at Several Body Sites. *Perception & Psychophysics*, 57(5):724–737, 1995.

- [113] J.W. Morley and M.J. Rowe. Perceived pitch of vibrotactile stimuli: effects of vibration amplitude, and implications for vibration frequency coding. *The Journal of Physiology*, 431:403–416, 1990.
- [114] G. Vonbckesy. Vibration of the head in a sound field and its role in hearing by bone conduction. *Journal of the Acoustical Society of America*, 20(6):749–760, 1948.
- [115] S.A. Dunlap, M.L. Lenhardt, and A.M. Clarke. Human skull vibratory patterns in audiometric and supersonic ranges. *Otolaryngologyhead and neck surgery official journal of American Academy of OtolaryngologyHead and Neck Surgery*, 99(4):389–391, 1988.
- [116] M.L. Lenhardt, A. Shulman, and B.A. Goldstein. Bone-conduction propagation in the human body: Implications for high-frequency therapy. *The International Tinnitus Journal*, 2(13):81–86, 2007.
- [117] R.L. Knoblauch, M.T. Pietrucha, and M. Nitzburg. Field Studies of Pedestrian Walking Speed and Start-Up Time. *Transportation Research Record: Journal of the Transportation Research Board*, 1638(1):27–38, 1996.
- [118] G.P. Soong, J.E. Lovie-Kitchin, and B. Brown. Measurement of preferred walking speed in subjects with central and peripheral vision loss. *Ophthalmic and Physiological Optics*, 24(4):291–295, July 2004.
- [119] E.T. Hall. *The Hidden Dimension*. Anchor, October 1966.
- [120] J.-C. Zufferey, A. Klaptocz, A. Beyeler, J.-D. Nicoud, and D. Floreano. A 10-gram Microflyer for Vision-based Indoor Navigation. In *IEEE/RSJ International Conference on Intelligent Robots and Systems*, volume 1, pages 3267–3272, October 2006.
- [121] B. Barber, S. Griffiths, T. McLain, and R. Beard. Autonomous landing of miniature aerial vehicles. *Journal of Aerospace Computing, Information, and Communication*, 4(5):770–784, 2007.
- [122] J. Kim and G. Brambley. Dual Optic-flow Integrated Navigation for Small-scale Flying Robots. In *Proc. of Australasian Conference on Robotics and Automation, Brisbane, Australia*, 2007.
- [123] E. Hirasaki, S.T. Moore, T. Raphan, and B. Cohen. Effects of walking velocity on vertical head and body movements during locomotion. *Experimental Brain Research*, 127(2):117–130, 1999.

Bibliography

- [124] J. Conroy, G. Gremillion, B. Ranganathan, and S. Humbert. Implementation of wide-field integration of optic ow for autonomous quadrotor navigation. *Autonomous Robots*, 27(3):189–198, 2009.
- [125] S. Humbert, J.K. Conroy, C.W. Neely, and G.L. Barrows. Wide-Field Integration Methods for Visuomotor Control. In Dario Floreano, Jean-Christophe Zufferey, Mandyam V. Srinivasan, and Charlie Ellington, editors, *Flying Insects and Robots*, chapter 5. Springer Berlin Heidelberg, 2009.
- [126] H. Dahmen, A. Millers, and H.A. Mallot. Insect-inspired odometry by optic flow recorded with optical mouse chips. In Dario Floreano, Jean-Christophe Zufferey, Mandyam V. Srinivasan, and Charlie Ellington, editors, *Flying Insects and Robots*, pages 115–126. Springer Berlin Heidelberg, 2010.

C Publications

Journal articles

Vision Tape - A Flexible Compound Vision Sensor for Motion Detection and Proximity Estimation (2012), **M.K. Dobrzynski**, R. Pericet-Camara and D. Floreano, *Sensors Journal*, IEEE **12**(5), pp: 1131-1139, DOI: 10.1109/JSEN.2011.2166760

Figure 2 of this article has been selected for the front page of the volume

Quantifying Information Transfer Through a Head-Attached Vibrotactile Display: Principles for Design and Control (2012), **M.K. Dobrzynski**, S. Mejr, S. Wischmann and D. Floreano, *Biomedical Engineering*, IEEE Transactions on **59**(7), pp: 2011-2018, DOI: 10.1109/TBME.2012.2196433

This article has been awarded the 2012 NCCR Robotics Best PhD Paper Award

A Miniature Curved Artificial Compound Eye (2013), D. Floreano, R. Pericet-Camara, S. Viollet, F. Ruffier, A. Bruckner, R. Leitel, W. Buss, M. Menouni, F. Expert, R. Juston, **M.K. Dobrzynski**, G. L'Eplattenier, F. Recktenwalde, H.A. Mallot and N. Franceschini, *Proceedings of the National Academy of Sciences*, **110** (23), pp: 9267-9272, DOI: 10.1073/pnas.1219068110

Conference proceedings

Contactless Deflection Sensor for Soft Robots (2011), **M.K. Dobrzynski**, R. Pericet-Camara and D. Floreano, *Intelligent Robots and Systems (IROS) IEEE/RSJ International*

Appendix C. Publications

Conference on, pp: 1913-1918, DOI: 10.1109/IROS.2011.6094845

Contactless deflection sensing of concave and convex shapes assisted by soft mirrors (2012), **M.K. Dobrzynski**, I. Halasz, R. Pericet-Camara and D. Floreano, Intelligent Robots and Systems (IROS) IEEE/RSJ International Conference on, pp: 4810-4815, DOI: 10.1109/IROS.2012.6385505

Hyper-Flexible 1-D Shape Sensor (2013), **M.K. Dobrzynski**, H. Vanderparre, R. Pericet-Camara, G. L'Eplattenier, S. Lacour and D. Floreano, 17th International Conference on Solid-State Sensors, Actuators and Microsystems, *Accepted*

Conference and workshop contributions

Vision Tape - a novel class of flexible vision sensor for robots and humans (2011), **M.K. Dobrzynski**, G. L'Eplattenier, R. Pericet-Camara and D. Floreano, IEEE Swiss Image and Vision Sensors Workshop 2011 (SIVS11), Zurich, Switzerland, September 2011.

Towards wearable vision: promises, challenges and recent developments (2013), **M.K. Dobrzynski**, Compound Eyes: from Biology to Technology, workshop, Tuebingen, Germany, March 2013.

Shape Sensors for Soft Robots (2013), **M.K. Dobrzynski**, R. Pericet-Camara and D. Floreano, International Workshop on Soft Robotics and Morphological Computation (SoftRobot2013), Monte Verita, Ascona, Switzerland, July 2013.



Michal Karol DOBRZYNSKI

nationality: Polish
born: 29.09.1982
married, 1 child

Av. du Tir Federal 36,
1024 Ecublens, CH
+41 76 735 61 35
email: m.k.dobrzynski@gmail.com
michal.dobrzynski@epfl.ch

Education

PhD Manufacturing Systems and Robotics, *Ecole Polytechnique Fédérale de Lausanne*, Switzerland 2009-2013

MSc Eng Automatic Control and Robotics, Electrical Dpt., *Warsaw University of Technology*, Poland, 2001–2006

Work experience

2009 – 2013 Doctoral assistant, Laboratory of Intelligent Systems, EPFL, Switzerland

- Microcontroller implementation of signal processing algorithms for motion recognition and obstacle avoidance, based on images acquired with wearable flexible vision sensors. Technical aspects of wearable system development.
- Participation in tasks within the European Project CURVACE, conducted in cooperation with industrial research institutes and universities.
- Supervision of 8 master level student projects. Teaching assignments in student courses related to: *microcontroller-based vision processing for motion detection and sensors for mobile robots*.

2007 – 2009 Researcher, Numerical Methods Laboratory, Politehnica University of Bucharest, Romania
(Marie Curie fellowship, European Commission)

- Matlab-based software development for simulation of electromagnetic field phenomena in micro-VLSIs.
- Development of customized method for direct inversion of huge sparse matrices and its subsequent Matlab implementation.

2006 – 2007 Application and Commissioning Engineer, SGAR S.L., Barcelona, Spain

- Development of automatic control system and a subsequent commissioning of parts of production lines in automotive and food processing factories (Ford, Heineken, Sandevid).
- Elaboration of technical offers, stuff supervision, contracts negotiations, and technical documentation.

2005 – 2006 Control Systems Engineer, Danone, Warsaw, Poland

- Development of a remote monitoring and data acquisition systems.

Language skills

Polish (Mother tongue), English (C2), Spanish (B1), French (A2), German (A1), Russian (A1)

Honors and Awards

- Scientific scholarships 2004/2005 and 2005/2006,
- Best poster award at ESCO'08 Czech Republic,
- Front cover in Int. IEEE Sensors journal, vol.12, 2012,
- NCCR Robotics Best PhD Paper Award 2012,
- Invited talk at CURVACE workshop, Tuebingen, March'12.